Soliton Interpretation of Arterial Blood Pressure Waveform: Derivation, Verification of Korteweg-de Vries type Dynamics and Application of Nonlinear Fourier Analysis

G. Gezer

Master of Science Thesis

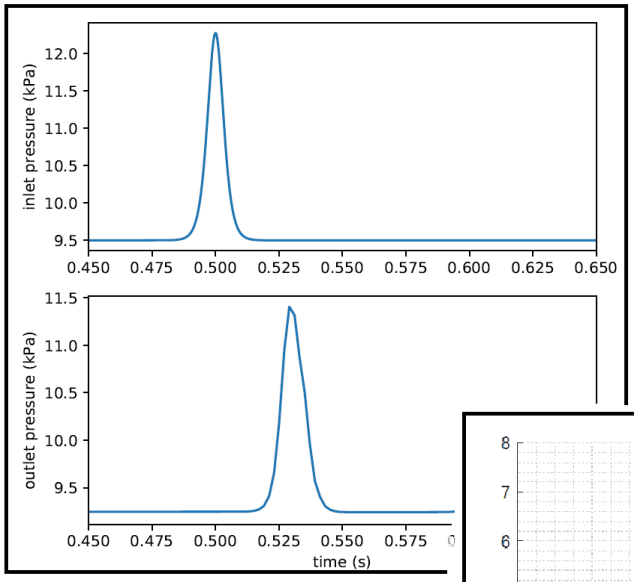

$$\dot{A} + \frac{\partial (A v_z)}{\partial z} = 0$$

$$\dot{Q}_z + \frac{\partial}{\partial z}\left(\frac{Q_z^2}{A}\right) + \frac{A}{\rho}\frac{\partial P}{\partial z} = \frac{f_z}{\rho}$$

$$\dot{u} + 6u\frac{\partial u}{\partial x} + \frac{\partial^3 u}{\partial x^3} = 0$$

$$h\frac{\partial^2 \psi}{\partial x^2} + u(x,t)\psi = \lambda\psi$$

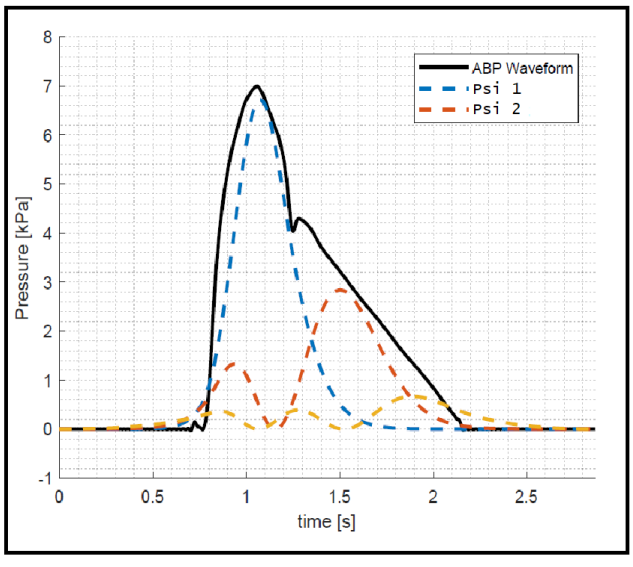

TU Delft Delft University of Technology

Biomechanical Engineering (BMechE)
Delft Center for Systems and Control (DCSC)

Soliton Interpretation of Arterial Blood Pressure Waveform: Derivation, Verification of Korteweg-de Vries type Dynamics and Application of Nonlinear Fourier Analysis

Master of Science Thesis

For the degrees of Master of Science in Systems & Control and Mechanical Engineering at Delft University of Technology

G. Gezer

January 21, 2019

Faculty of Mechanical, Maritime and Materials Engineering (3mE) · Delft University of Technology

Delft University of Technology
Department of
Biomechanical Engineering and Delft Center for Systems and
Control

The undersigned hereby certify that they have read and recommend to the Faculty of Mechanical, Maritime and Materials Engineering (3mE) for acceptance a thesis entitled

Soliton Interpretation of Arterial Blood Pressure Waveform: Derivation, Verification of Korteweg-de Vries type Dynamics and Application of Nonlinear Fourier Analysis

by

G. Gezer

in partial fulfillment of the requirements for the degrees of

Master of Science Systems & Control and Mechanical Engineering

Dated: January 21, 2019

Supervisor(s):

prof.dr.ir. J. Dankelman

dr.ir. S. Wahls

ir. P.J. Prins

Reader(s):

prof.dr.ir. M. Verhaegen

Abstract

As a nonlinear alternative to the linear interpretation of arterial blood pressure waveform, soliton theory has been proposed to model arterial blood pressure by interpreting the pulsatile nature of pressure pulses in the viewpoint of soliton transmission. The existing solitary wave literature supports this interpretation by deriving Korteweg-de Vries (KdV) type dynamics from 1-D Navier-Stokes equations. In this paper, we explain and discuss the derivation of KdV type dynamics for arterial blood pressure from basics of fluid motion. As original work, we provide two verification tests for two of the existing KdV models in three case studies which are considered to be interconnected sections of a simplified arterial network. Finally, using both KdV models and considering realistic inlet boundary conditions, we study arterial blood pressure waveforms using nonlinear Fourier analysis to extract physical information.

Table of Contents

Preface

As much as I would like to see this graduation project as the product of my initiative and endeavor, the project has taught me that scientific research is a cumulative effort beyond anything else. I want to use the opportunity to thank my supervisors involved in my graduation project. I started as a beginner to both fields of partial differential nonlinear systems and cardiovascular modeling. Also considering the fact that my bachelor studies were in electrical and computer engineering fields, I would not be able to conduct this research without the supervision of Dr.ir. S. Wahls and Prof.dr. J. Dankelman. Ir. P. J. Prins has also dedicated his time often to help me with minor issues as my daily supervisor, which helped me to resolve problems arising in a smaller scale.

I also want to thank Prof.dr.ir. M. Verhaegen for taking the role of DCSC defense committee leader. Under his vision, DCSC has employed dedicated researchers and research groups to *Numerics for Control and Identification* scientific section, which my project also depended on. I truly feel blessed to have him in my defense committee.

Over the course of my studies, I have taken several responsibilities to act on the student life in *Delft Center for Systems and Control* (DCSC) department and Mechanical, Maritime and Materials Engineering (3mE) faculty. As a personal highlight, in DCSC's old student dispute *Out of Control* (OoC), for three generations I had an opportunity to work among countless faculty members and student colleagues on academic, professional and social matters that led to the formation of the new student dispute *Delft Student Association for Systems and Control* (D.S.A. Kalman). I want to thank especially Dr.ir. T. van den Boom, M. Versloot-Bus and Prof.dr.ir. H. Hellendoorn for providing me countless responsibilities and helping in various matters to improve student life. I also want to thank my OoC colleagues for the unique comradery feeling that I will cherish for the rest of my life and the new generation of D.S.A. Kalman for taking the mantle of OoC and furthering its vision.

Last but not least, I want to thank Dr. ir. S. Wahls again for reasons beyond my graduation project context. In two of his lectures, for four years, I was employed as a teaching assistant. During my teaching assistant experience, I was granted the opportunity to help thousands of students in practical sessions, in online sessions and in additional tutorials. He always allowed me to take over more responsibilities, which I can never thank him enough for. Under his supervision, I became a better student and I had the opportunity to make other students better. I genuinely felt happy to show up for work 'every' time and I would not have had the same experience if he was not involved.

Chapter 1

Introduction

Flow and pressure propagate in the cardiovascular system as waves, generated by periodic ejection of blood from the heart to the arterial tree at each cardiac cycle. Based on blood dynamics, interaction with vessel walls and with mechanical discontinuities, the incident waveform changes as it travels, resulting in waveform shapes characteristic to their locations in the arterial tree. This is referred to as *pulsatile* pressure and flow. Exemplary arterial volumetric flow, Q, and pressure, P, waveforms are provided in Figure 1-1.

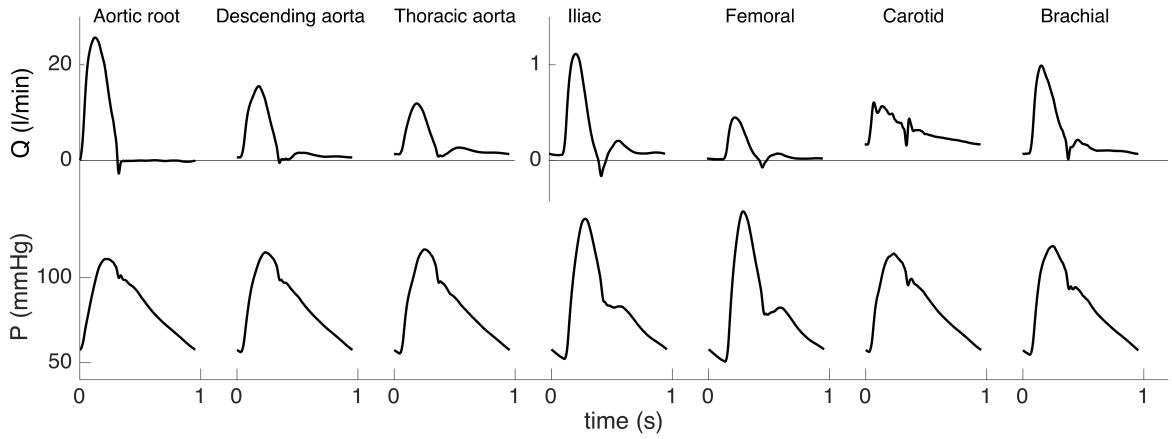

Figure 1-1: Exemplary arterial waveforms at different locations in the arterial network [1].

The cardiac cycle comprises of two phases called *systole* and *diastole* during which the heart muscle contracts and relaxes respectively. The part of the arterial waveforms corresponding to the first one third of the cardiac cycle is referred to as the *systolic part*, whereas the rest of the waveform is referred to as the *diastolic part*. In the systolic part, pressure increases to the maximum value from the minimum value fast, which is immediately followed by a fast decrease. In the diastolic part, the variation of pressure is relatively smaller and the pressure is considered to gradually decrease with time reaching its minimum value at the end.

Modeling and understanding of the dynamics of arterial blood flow and pressure can be beneficial beyond a mathematical context. Cardiac output, which is a measure of volumetric flow, is used in clinical applications to assess cardiovascular state. Accurate measurements of the cardiac output are needed for high risk patients and are often done with invasive methods. As arterial blood pressure is measured continuously by minimally invasive monitoring devices, modeling of arterial blood pressure can potentially provide us better means to estimate the cardiac output globally and at the same time improve patient health by removing dependency on invasive methods.

The Windkessel models, originally proposed by Frank [2], have been intensively studied in scientific literature and used in clinical applications to model the flow-pressure relationship. This led to the popular linear interpretation of arterial blood pressure waveform referred to as the *wave-reflection model* proposed by Westerhof et al. [3]. Based on this model, the waveform is interpreted as the superposition of a forward and a backward wave. However the nonlinear dynamics of fluid motion can not be properly modeled by Windkessels. As a nonlinear alternative, soliton theory has been proposed to model arterial blood flow and pressure dynamics in large arteries, dating back to works of Hashizume [4, 5] and Yomosa [6].

Based on the soliton interpretation, arterial blood waveform is modeled after solitons moving in one direction, whereas the rest of the waveform characteristics are associated to the reflections in transmission. To the extent of our knowledge, the existing soliton theory on the modeling of arterial blood pressure is supported by the derivation of Korteweg-De Vries (KdV) dynamics from 1-D Navier-Stokes equations for blood flow in large arteries [6, 7, 8]. Once again to to the extent of our knowledge, in the scientific literature there has not been publications dedicated to the verification of the KdV type dynamics, beyond the benchmark tests provided by the original model creators or their coworkers. In this paper, we will provide verification tests for KdV type dynamics derived by Yomosa [6] and Crépeau and Sorine [9] and the corresponding 1-soliton solutions. These dynamics will be benchmarked against 1-D Navier-Stokes equations using openBF blood software by Melis [10]. Both considered KdV models [6, 9], do not take the effects of friction and the connection to other vessels into account for the derivation of KdV type dynamics. We will also test the modeling capabilities of KdV models with in the presence of these effects beyond their derivation assumptions. This would provide us insight on modeling clinical measurements with KdV type equations, as the clinical data is subject to frictional effects and interconnection effects.

Additionally, KdV type dynamics for the arterial blood flow implies a potential application of scattering transform to analyze arterial blood pressure waveform. To the extent of our knowledge, Nonlinear Fourier Analysis of the arterial blood waveform has been done by only Laleg-Kirati and her co-workers in multiple works [11, 12, 13, 14, 15]. In all Laleg-Kirati's publications, although the application of nonlinear Fourier analysis is attributed to the underlying KdV type dynamics, the parameter used for the scattering transform is not calculated based on the coefficients of the derived KdV equation, but chosen small enough to provide the desired estimate error by considering only the discrete spectrum for the reconstruction of the initial data. Such an approach can be seen as a model fitting task instead of calculation of a physically representative spectrum. In our paper, both Yomosa's model [6] and Crépeau and Sorine's model [9] will be used to calculate the corresponding scattering problem which might provide us physically relevant insight on the soliton interpretation of arterial blood pressure waveforms.

Chapter 2

Biomechanical Design Part

2-1 Cardiac Output and its Clinical Measurement

Section 2-1 is adapted from the literature survey.

Cardiac output is the volume of blood ejected by the left ventricle per minute and it is a cardinal parameter used to assess cardiovascular state, global oxygen delivery and tissue perfusion. The cardiac output can be calculated by multiplying the heart rate with the stroke volume, which is the amount of blood pumped by the left ventricle at each heart beat:

$$\text{Cardiac output} = \text{Heart rate} \times \text{Stroke volume}. \tag{2-1}$$

Cardiac output monitoring is an important tool in high risk critically ill surgical patients in whom large fluid shifts are expected along with bleeding and hemodynamic instability [16]. Routine clinical measurements of the cardiac output is often done with invasive indicator-dilution methods such as thermodilution [17]. The pulmonary artery catheter method is till date considered as the golden standard method to measure the cardiac output [18]. There are various complications associated with the pulmonary artery catheter method as described in Domino et al. [19]. Based on the study of Boyd et al. on pulmonary artery catheter method, in 24% of the cases complications are reported. Based on Katsikis et al. [20], pulmonary artery catheter accounts for 64-67% of knotted devices among all intravascular catheters. An image of knotted pulmonary artery catheter after removal is provided in Figure 2-1.

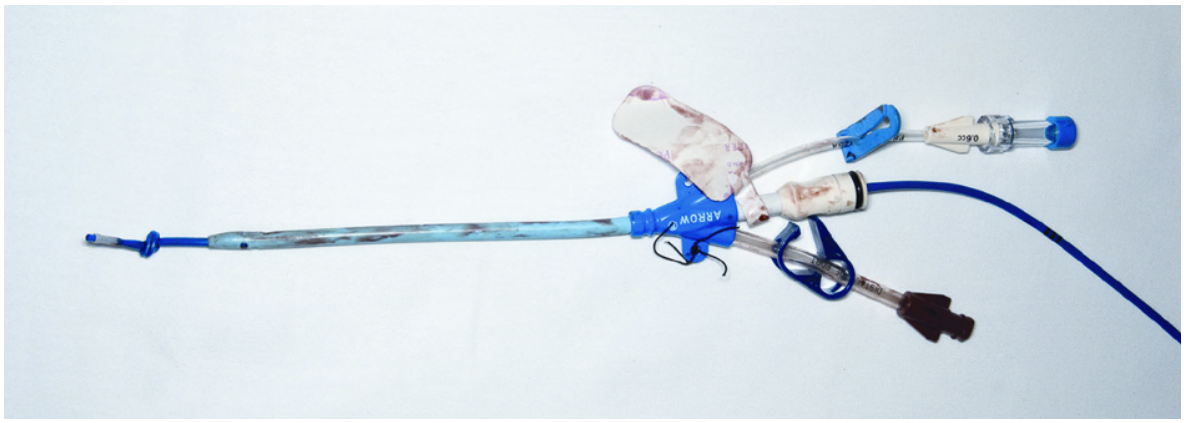

Figure 2-1: Knotted pulmonary artery catheter after removal [21].

Due to the invasive nature of the pulmonary artery catheter method, less invasive and non-invasive methods to measure the cardiac output have gained increased appeal. Among the minimally invasive methods, analysis of arterial blood pressure waveforms has been of scientific interest to provide important information as arterial blood pressure is measured continuously in many operating rooms and intensive care units [22]. Commercially available monitoring devices estimate the cardiac output from arterial blood pressure waveforms with *pulse contour methods* which assume that the area under the systolic part of an arterial blood pressure waveform is proportional to the cardiac output. Often imprecise metrics, like maximum, minimum and mean value of the arterial blood pressure waveform, are used to estimate the cardiac output. For the interested reader, a comparison of some of these global estimation algorithms can be found in Sun et al. [17]. As the variability of arterial blood pressure waveforms beyond the imprecise metrics is not taken into account by the pulse contour methods, modelling the dynamics of arterial blood flow and pressure can potentially lead to the development of better estimators for cardiac output.

2-2 Arterial Blood Pressure Interpretation

2-2-1 Windkessel Interpretation of Arterial Blood Pressure

As a pioneer in linear modeling of arterial blood flow, in 1899 Frank [2] has applied the *Windkessel* concept to describe the mechanics of a compliant aorta. Based on this model, the blood flow-pressure relationship is described by a *linear ordinary differential* equation. An electrical analogy of the Frank's 2-element Windkessel is provided in Figure 2-2.

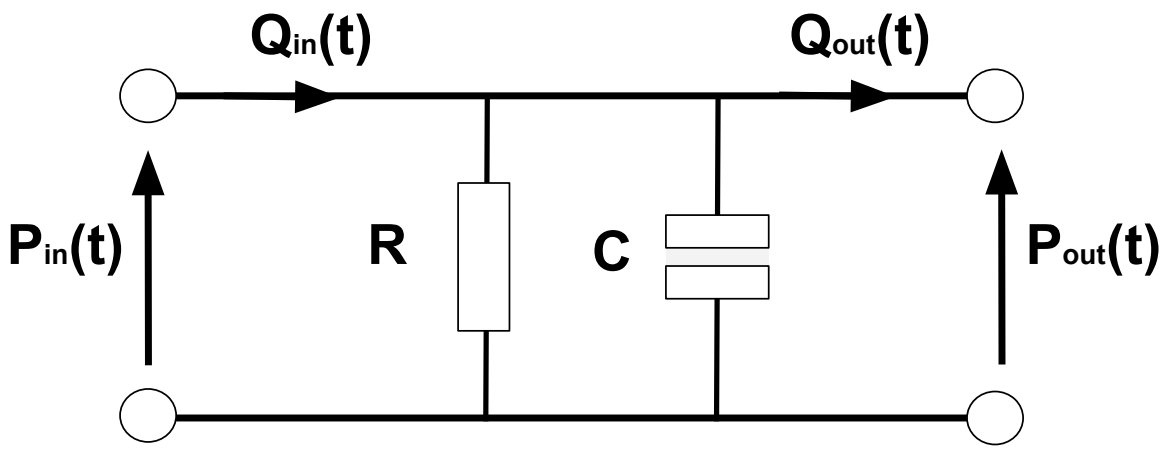

Figure 2-2: Representation of the 2-element Windkessel using an electrical circuit analogy.

Frank's model was able to describe the dynamics of the diastolic portion of arterial blood pressure and flow waveforms accurately with an exponential decay profile in time. However, variability of data in the systolic part of waveforms were not explained by the 2-element Windkessel. Westerhof et al. [23] have proposed a third element between the flow source and the Frank's Windkessel to account for the resistance to blood flow due to the aortic valve to tackle this specific problem. An electrical analogy of the Westerhof's 3-element Windkessel is provided in Figure 2-3.

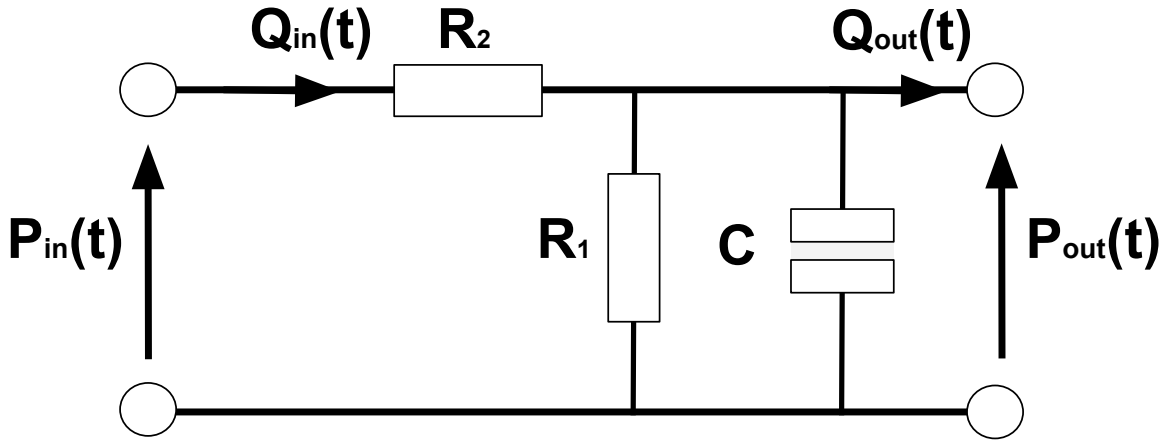

Figure 2-3: Representation of the 3-element Windkessel using an electrical circuit analogy.

Additionally in Westerhof's model, Fourier analysis has been used to identify the Windkessel elements as a natural consequence of assuming linear ordinary differential dynamics. The 3-element Windkessel modeling choice lead to its own interpretation of arterial blood waveforms, referred to as the *wave reflection model*. In particular, Westerhof et al. [3] have interpreted the pressure and flow pulses as composite waves consisting of a forward traveling and a

backward traveling component. The forward wave is associated to the ejection of blood from the heart and the backward wave is associated to physical reflections caused by the mechanical discontinuities in the arterial tree. In the diastolic phase, both waves are considered to have destructive superposition, whereas in the systolic phase, both waves are considered to have constructive superposition. The constructive superposition can also explain the increase of peak pressure of the waveform during its propagation in some arteries which is referred to as *steepening*. An illustration of the wave reflection model and the steepening phenomena is provided in Figure 2-4.

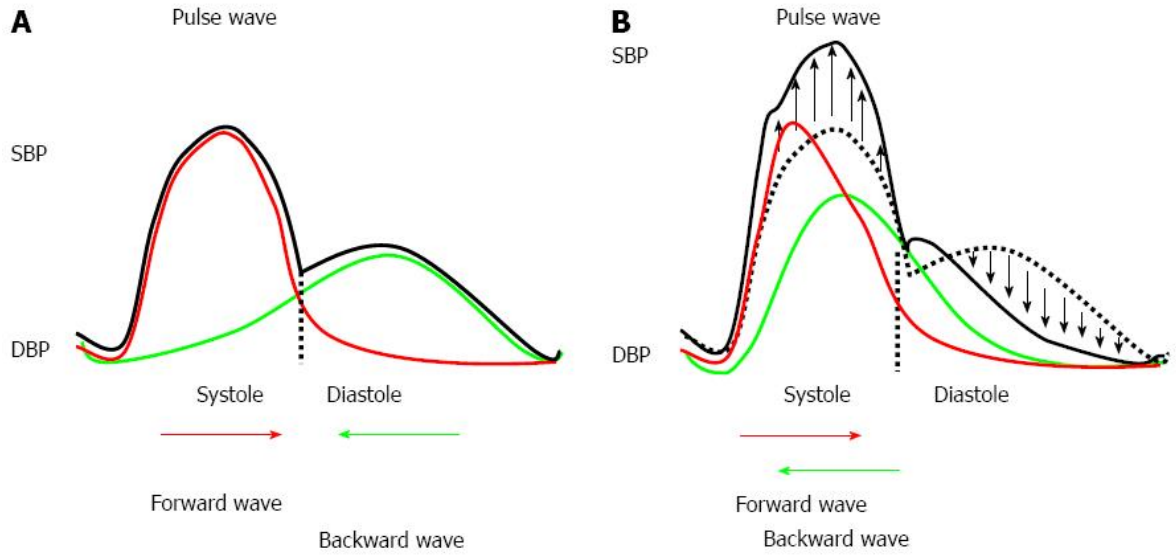

Figure 2-4: An illustration of the forward and the backward wave superposition [24]. SBP: systolic blood pressure, DBP: diastolic blood pressure.

3-element Windkessel models are till date widely used to model the pressure and flow relationship. Windkessels with 4-element proposed by Burattini and Gnudi [25] are also used in abundance in the existing literature. The Windkessel models made arterial compliance and impedance frequently used parameters to model arterial dynamics in *lumped models*. In the lumped models, each artery is modeled after a Windkessel and arterial networks are modeled after the interconnection of these individual Windkessels. However based on the derivations of Navier-Stokes equations for large arteries, the evolution of blood flow and pressure are described by *nonlinear partial differential* equations instead [26]. Furthermore in compliant artery models, the dynamics of the vessel wall movement is also an important determinant of arterial flow and pressure dynamics. Frank's and Westerhof's Windkessels relies on the simplification of fluid dynamics and vessel wall movement dynamics, using 2 and 3 linear elements respectively. In the lumped models, this simplification leads to more error with increasing network size. This is why the modern compliant artery modeling literature combines the concept of Windkessel, Navier-Stokes equations and the vessel wall dynamics in hybrid models. In the hybrid models, intermediate Windkessel flow and pressure variables, Q_W and P_W respectively, are calculated based on fluid and vessel wall dynamics using the system input. The input flow and/or pressure is referred to as *inlet boundary conditions*. *System equations* comprise of Navier-Stokes equations describing fluid dynamics and the material law describing vessel wall movement. Q_W and P_W are treated as inputs to the Windkessel

whose output is also considered as the system output. An an important remark, this type of Windkessel models the hydraulic impedance that results from connection to other vessels instead of *all* dynamics describing a compliant artery. In mathematical terminology, the Windkessel describes the *outlet boundary conditions*. The structure of common hybrid models with 3-element Windkessel is provided in Figure 2-5.

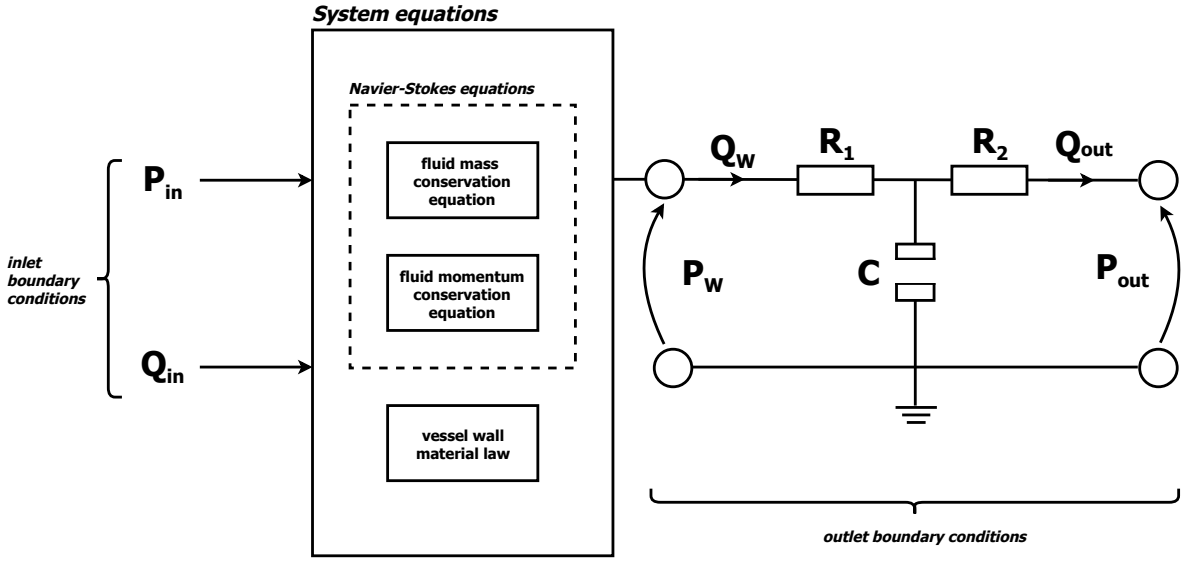

Figure 2-5: Hybrid arterial blood flow and pressure model structure.

In the rest of our paper, we will treat Windkessels as outlet boundary conditions that model the connection to the other vessels based on hybrid modeling approach.

2-2-2 Soliton Interpretation of Arterial Blood Pressure

Based on the soliton theory interpretation of arterial blood pressure, an analogy is made between pressure pulses and soliton transmission. Unfamiliar readers can read about basic properties of solitons in Appendix B. There have been handful of publications on modeling arterial blood pressure using soliton theory; the earliest publications date back to Hashizume [4, 5] and Yomosa [6].

To the extent of our knowledge, the existence of soliton solutions are supported by the derivation of KdV type dynamics from 1-D Navier-Stokes equations and a dynamic material law [6, 27, 8, 7, 9, 11, 28]. As a side remark, the terms included in 1-D Navier-Stokes equations and the material law assumptions differ between some of these works. The following steps are followed for the derivation of KdV type dynamics.

1. Physical model parameters, such as the vessel length or radius, are used to scale the system variables to dimensionless system variables. The system variables consist of a flow variable, either the axial velocity v_z or the volumetric flow Q_z, the pressure variable P and either the vessel radius R or the vessel cross-sectional area A. The space variable, z and the time variable t are also scaled to dimensionless variables. The dimensionless variables are used to convert the system equations to the non-dimensional form. The

system equations consist of three equations: two of them are the 1-D Navier-Stokes equations and the other one is the material law. The system equations and variables will be explained more in detail in Sections 2-3 and 2-4.

2. Traveling wave solutions in only one direction are used over the space variable z or the time variable t. If z is replaced, a spacelike KdV equation is obtained for P like in Yomosa [6]. If t is replaced instead, a timelike KdV equation is instead for P, like in Crépeau and Sorine [9]. If traveling wave solutions in both directions are considered, Boussinesq type equation is obtained for P, like in Paquerot and Remoissenet [29], which has a wave solution between a solitary and a shock wave.

3. Using long wave estimation and the reductive perturbation expansion method, the three non-dimensional equations are converted into three KdV type equations for the dimensionless system variables.

In the literature review submission, the solitary wave literature on modeling arterial blood pressure was discussed in detail. In this paper, we will focus on two works, specifically Yomosa [6] and Crépeau and Sorine [9].

Yomosa [6] has described the pulse waves of pressure and flow propagating through arteries as solitons by considering the 1-D Navier-Stokes equations of ideal fluid motion in an infinitely long, straight, circular, thin walled elastic tube. In Yomosa's work the effects of viscosity and friction are both neglected and only the traveling wave solutions in one direction are considered. Using various asymptotic methods, spacelike KdV type dynamics are derived for the longitudinal velocity, the pressure and the vessel radius.

Créapau and Sorin [9] and Laleg et al. [11] have proposed a model for the arterial blood flow based on the decomposition of pressure into two components; the wave component is modeled after 2 or 3-solitons whereas the slow phenomena is modeled after 2 or 3-element Windkessel which is used to correct the behavior of solitons, just like an outlet boundary condition. In Crépeau and Sorine timelike KdV type dynamics are derived for the volumetric flow, the pressure and the vessel cross-sectional area. Friction is included in the considered 1-D Navier Stokes equations but the frictional effects are excluded for the derivation of KdV type dynamics based on the fast times assumption. This is why the soliton solutions are defined only in boundary layers by Crépeau and Sorine and the frictional effects are absorbed by the Windkessel included in the model.

Solitons associated to the underlying KdV type dynamics are considered to move only in one direction, contrary to the interpretation of the wave reflection model. The superposition of finite number of solitons are considered to model a forward wave, comprising a *discrete spectrum*. The non-soliton contribution in the waveforms is considered to comprise a *continuous spectrum* associated to the reflections in transmission, which differ from physical reflections of the backward wave component of the wave reflection model. To the extent of our knowledge, there is not a work addressing the continuous spectrum of arterial blood pressure in the solitary wave literature.

If KdV type dynamics describes the pressure evolution in a compliant artery, we can extract physical information from the discrete spectrum of a given initial pressure data. The coefficients of the KdV equation derived for the pressure, will determine the relationship between the amplitudes, group velocities and width scalings of the solitons included in the solution.

Furthermore based on the perturbation expansion method, the soliton solutions for different variables are also related. For example, in Yomosa [6], a soliton solution for P corresponds to a soliton for v_z and for R. In Crépeau and Sorine [9], a soliton solution for P corresponds to a soliton for Q_z and for A. Therefore the discrete spectrum of the pressure solution can be used to estimate the discrete spectrum of the other system variables. This potentially means that estimation of the cardiac output can be done based on the correlation between the forward flow and the discrete spectrum of the pressure.

2-3 Derivation of Navier-Stokes Equations for Arterial Blood Flow

2-3-1 3-D Navier-Stokes Equations for Large Arteries

The 3-D Navier-Stokes equations describing the dynamics of fluid flow are

$$\dot{\rho} + \bigtriangledown \cdot (\rho \underline{v}) = 0, \tag{2-2}$$

$$\rho \frac{\partial \underline{v}}{\partial t} + \rho(\underline{v} \cdot \bigtriangledown)\underline{v} = \bigtriangledown \cdot \left(-P\underline{\underline{I}} + \underline{\underline{d}}\right) + \rho \underline{f}, \tag{2-3}$$

where $\bigtriangledown\cdot$ denotes the divergence operator, $\bigtriangledown$ denotes the gradient operator, x is the 3-D Cartesian position, t is the time, $\rho = \rho(x,t)$ is the fluid density, $\underline{v}= \underline{v}(x,t)$ is the velocity vector, P is the fluid hydrostatic pressure, $\underline{\underline{d}}$ is the deviatoric stress caused by fluid motion, $\underline{\underline{I}}$ is the unit tensor and f is the fluid body force per unit mass.

Three assumptions can be made based on arterial blood flow in *large arteries* [30]:

1. Blood is a Newtonian fluid:
$$\underline{\underline{d}} = 2\mu \underline{\underline{e}} - \frac{2\mu}{3}(\bigtriangledown \cdot \underline{u})\underline{\underline{I}}, \tag{2-4}$$
where μ is the fluid viscosity with
$$e_{ij} = \frac{1}{2}(\frac{\partial v_i}{\partial x_j} + \frac{\partial v_j}{\partial x_i}).$$

2. Blood is an isothermal fluid:
$$\mu \text{ is constant.} \tag{2-5}$$

3. Blood is incompressible:
$$\rho \text{ is constant.} \tag{2-6}$$

Using these assumptions Equations 2-2 and 2-3 can be reduced to:

$$\bigtriangledown \cdot \underline{v} = 0 \tag{2-7}$$

$$\rho \frac{\partial \underline{v}}{\partial t} + \rho(\underline{v} \cdot \bigtriangledown)\underline{v} = \rho \underline{f} - \bigtriangledown P + \mu \bigtriangledown^2 \underline{v}. \tag{2-8}$$

ρ and μ are commonly taken as 1050 kgm^{-3} and 3-4 mN sm^{-2} respectively [31].

2-3-2 Non-dimensional Form of the Navier-Stokes Equations

The variables in Equations 2-7 and 2-8 are scaled to non-dimensional form using the following variable transformations [30]:

$$\underline{x}^* = \frac{1}{R_d}\underline{x}, \quad t^* = t\omega, \quad \underline{v}^* = \frac{1}{v_{\text{mean}}}\underline{v}, \quad P^* = \frac{1}{\rho v_{\text{mean}}^2}P, \quad \underline{f}^* = \frac{R_d}{v_{\text{mean}}^2}\underline{f}, \tag{2-9}$$

where R_d is the vessel radius at diastolic phase, ω is the angular frequency of flow variation and v_{mean} is the mean velocity at the inlet of the artery. Dimensionless Reynolds and Strouhal numbers describing fluid dynamics, denoted by Re and St respectively, are defined as

$$Re = \frac{\rho R_d v_{\text{mean}}}{\mu}, \quad St = \frac{\omega R_d}{v_{\text{mean}}}. \tag{2-10}$$

Using Equations 2-9 and 2-10 Navier-Stokes equations can be described in non-dimensional form:

$$\bigtriangledown \cdot \underline{v}^* = 0, \tag{2-11}$$

$$St\ \frac{\partial \underline{v}^*}{\partial t} + \underline{v}^* \cdot \bigtriangledown \underline{v}^* - \frac{1}{Re}\bigtriangledown^2 \underline{v}^* + \bigtriangledown P^* = \underline{f}^*. \tag{2-12}$$

Based on Equations 2-11 and 2-12, for large Reynolds numbers the nonlinear convective term, $\underline{v}^* \cdot \bigtriangledown \underline{v}^*$, dominates the viscous term, $\frac{1}{Re}\bigtriangledown^2 \underline{v}^*$. Based on the measurements of flow pulses in canine arteries [32], this is assumed to be the case so the viscosity term is neglected, leading to further reduced 3-D Navier-Stokes equations:

$$\frac{\partial \underline{v}}{\partial t} + (\underline{v} \cdot \bigtriangledown)\underline{v} + \frac{1}{\rho}\bigtriangledown P = \underline{f}, \tag{2-13}$$

$$\bigtriangledown \cdot \underline{v} = 0. \tag{2-14}$$

2-4 1-D Modeling of Arterial Blood Flow

Section 2-4 and its subsections are adapted from the literature survey.

2-4-1 Reduction of 3-D Navier-Stokes Equations to 1-D

The solitary wave literature on modeling arterial blood flow is based on 1-D Navier-Stokes equations [6, 29, 27, 8, 9, 11, 14]. This makes the assumptions followed for dimension reduction relevant for these works. In order to reduce 3-D Navier-Stokes equations (Equations 2-13 and 2-14) to 1-D form, the following ideal vessel geometry assumptions are made:

1. The artery is modeled after a cylinder resting in horizontal position. Due to this choice cylindrical coordinates, (z, r, θ), are chosen for representation over Euclidean coordinates, (x_1, x_2, x_3). z is the longitudinal coordinate and increases in the direction away from the heart whereas (r, θ) pair refer to the polar coordinates of the cross-section at z. A diagram of the cylindrical coordinate representation of the artery is provided in Figure 2-6.

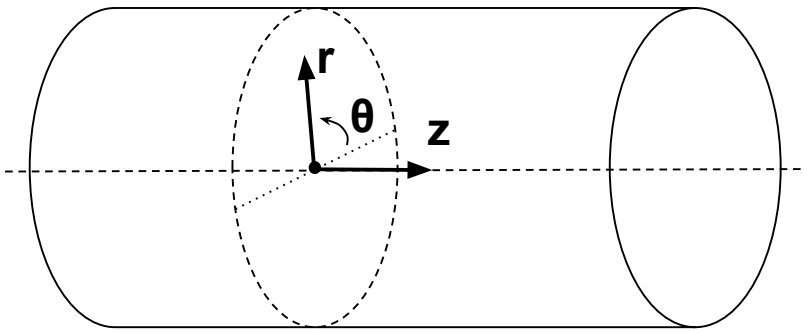

Figure 2-6: Cylindrical coordinates chosen for blood vessel representation.

2. The artery is assumed to be symmetrical around longitudinal axis (axisymmetry), therefore dependencies on and the dynamics of θ are excluded.

3. The radial flow dynamics are excluded.

4. The derivatives with respect to r are excluded in the dynamics based on the thin cylinder assumption. Based on this assumption:

$$L \gg R_d, \tag{2-15}$$

where L is the vessel length.

5. The terms multiplied with the radial velocity, v_r instead of the longitudinal velocity, v_z, are neglected based on the assumption

$$v_z \gg v_r. \tag{2-16}$$

Using these assumptions, the 3-D model described by Equations 2-13 and 2-14 can be reduced to 1-D form:

$$\frac{\partial v_z}{\partial t} + v_z \frac{\partial v_z}{\partial z} + \frac{1}{\rho}\frac{\partial P}{\partial z} = \frac{f_z}{\rho A}, \tag{2-17}$$

$$\frac{\partial A}{\partial t} + \frac{\partial (A v_z)}{\partial z} = 0, \tag{2-18}$$

where $f_z = f_z(v_z) = \frac{f}{A}$ is the axial friction force per length. The volumetric flow in the longitudinal direction, Q_z, is the product of the cross-sectional area and the longitudinal velocity:

$$Q_z = A v_z, \tag{2-19}$$

where $A = A(z,t) = \pi R^2$ is the vessel cross-sectional area and $R = R(z,t)$ is the vessel radius. Equations 2-17 and 2-18 can alternatively be written in terms of Q_z:

$$\frac{\partial Q_z}{\partial t} + \frac{\partial}{\partial z}\left(\frac{Q_z^2}{A}\right) + \frac{A}{\rho}\frac{\partial P}{\partial z} = \frac{f_z}{\rho}, \tag{2-20}$$

$$\frac{\partial A}{\partial t} + \frac{\partial Q_z}{\partial z} = 0. \tag{2-21}$$

2-4-2 Peripheral Friction Model

The frictional force in the longitudinal direction for an incompressible Newtonian fluid for the axisymmetric vessels is given as follows [33]:

$$f_z = 2\pi\mu R \frac{\partial \left(F v_z\right)}{\partial r}|_{r=R} \ , \tag{2-22}$$

where $F = F(r)$ is the radial velocity profile. Based on Equation 2-22, the friction depends on the flow value at $r = R$, which is the reason this type of friction is also referred to as *peripheral friction*, associated to the interaction of blood with the vessel wall. In the literature, the term *viscous friction* is also commonly used as f_z scales linearly with μ. In fact, in modeling literature friction is referred to as viscous effect. In our paper, friction is considered as a separate effect whereas viscous effects are considered to correspond to viscosity dependent second order spatial dynamics in Navier-Stokes equations.

Based on Equation 2-22, F is needed to derive f_z. Polynomial radial velocity profile of order Γ is assumed [34] such that

$$F = \frac{\Gamma + 2}{\Gamma}\left[1 - \left(\frac{r}{R}\right)^{\Gamma}\right]. \tag{2-23}$$

Based on the experimental studies by Hagen [35] and Poiseuille [36] on steady laminar flow of water in the cylindrical pipes, F is found to have a parabolic shape ($\Gamma = 2$). This assumption is used throughout in the existing solitary wave literature on arterial blood pressure modeling [6, 29, 27, 8]. However based on Smith et al.'s analysis of blood flow through a geometric model of the coronary network in different points of the cardiac cycle [33], F is found to have a higher polynomial order instead ($\Gamma = 9$). In this paper, $\Gamma = 9$, is assumed based on Smith et al's findings. By substituting Equation 2-23 into Equation 2-22, the following frictional force is obtained:

$$f_z = -2\pi\mu(\Gamma + 2)\upsilon_z = -2\pi\mu(\Gamma + 2)\frac{Q_z}{A}. \tag{2-24}$$

2-4-3 Linear Elastic Arterial Wall Model

The arterial wall is modeled after a thin, incompressible, homogenous, isotropic membrane [37]. Furthermore the arterial wall is assumed to deform axisymmetrically and the longitudinal deformations are ignored. The membrane is assumed to participate in only linear elastic deformation. Under these assumptions the material law is defined as [37]

$$P = P_0 + \frac{4Eh_0}{3R_0^2}(R - R_0), \tag{2-25}$$

where P_0 is the reference pressure, E is the Young's elastic modulus, R_0 is the vessel radius at the reference pressure and h_0 is the reference vessel wall thickness at the reference pressure. The reference pressure in our paper will be taken as $P_0 = 0$, when the internal pressure of the vessel equals to the external pressure [37].

2-5 Derivation of KdV Equations from 1-D Navier-Stokes Equations

In this section, derivation of the KdV type dynamics from 1-D Navier-Stokes equations in Yomosa [6] and Créapau and Sorine [9] are discussed. Interested readers can find more information on the scaling of KdV Equation in Appendix A.

2-5-1 Yomosa's Model

In 1986, Yomosa [6] proposed a soliton theory for a simplified and idealized model-system the blood motion in large arteries. Yomosa's model can derive a relationship between the width, the amplitude and the group velocity of the flow and pressure pulses. Instead of interpreting the wave as a linear superposition of a backward and a forward component, the wave is interpreted as a nonlinear superposition of only forward components consisting of of 2 to 3 solitons. As the peripheral friction is neglected in Yomosa's work, his model does not account for the energy losses which means Yomosa's model can not describe the pressure as a decreasing function away from the heart. The steepening of the arterial blood pressure is explained in Yomosa's work in the context of nonlinear superposition principle of solitons. In this subsection, the model and the derivations of [6] will be discussed and referred to by the author name, Yomosa.

In Yomosa, the following model assumptions are made:

1. Blood is modeled as an isothermal, incompressible, Newtonian fluid (Section 2-3-1).
2. Viscous term in the blood dynamics is excluded (Section 2-3-2).
3. Friction term in the blood dynamics is excluded (Section 2-4-2).
4. The blood vessel is modeled as an infinitely long, straight cylinder.
5. 1-D dynamics are used over 3-D dynamics (Section 2-4-1).
6. The vessel wall is modeled as a thin, homogenous, elastic membrane. This corresponds to an extension of the static material law described in Equation 2-4-3 to a dynamic law with an additional parameter, a, which when set as non zero, makes the static component of P a nonlinear function of R.

Based on these assumptions in Yomosa, the provided system equations are

$$\frac{\partial Q_z}{\partial t} + \frac{\partial}{\partial z}\left(\frac{Q_z^2}{A}\right) + \frac{1}{\rho}A\frac{\partial P}{\partial z} = 0, \tag{2-26}$$

$$\frac{\partial A}{\partial t} + \frac{\partial Q_z}{\partial z} = 0, \tag{2-27}$$

$$P = \frac{Eh_0}{R_0^3}(R - R_0)\left(aR + (1-a)R_0\right) + \rho_w H\frac{\partial^2 R}{\partial t^2}, \tag{2-28}$$

where $Q_z = Q_z(z,t)$ is the volumetric flow rate, $P = P(z,t)$ is the pressure, $R = R(z,t)$ is the vessel radius, $A = A(z,t) = \pi R^2$ is the vessel cross-sectional area, ρ is the blood density, E is the elastic Young's modulus, h_0 is the reference vessel wall thickness, R_0 is the reference vessel radius, a is the nonlinear coefficient of elasticity, ρ_w is the vessel wall density and $H = H(z,t) = h + h'$ is the effective inertial thickness where $h = h(z,t)$ is the vessel thickness that participates in elastic deformation and h' is the vessel thickness that does not. The reference length measurements are taken at $P = 0$, specifically when the external pressure of the vessel equals to the internal pressure. It should be noted that in Yomosa's work, the longitudinal velocity, $v_z = v_z(z,t)$, is used as a model variable, instead of $Q_z = Av_z$.

Using various asymptotic methods, Yomosa reduces the system equations to three KdV type equations for each model variable, specifically for v_z, P and R. Yomosa's derivations can be summarized in the following steps.

1. t, z, v_z, P and R are scaled to dimensionless variables t^*, z^*, v_z^*, P^* and γ^* respectively using physical model parameters. The dimensionless variables are used to convert Equations 2-26, 2-27 and 2-28 to non-dimensional form.

2. A linear dispersion relation is acquired for the non-dimensional nonlinear problem. To do so, first nonlinear terms in the dynamics are neglected to obtain linearized set of equations. Then harmonic solutions are assumed for the dimensionless variables so that

$$v_z^*,\ P^*,\ \gamma^* \propto e^{i(kz^* - \omega t^*)}, \tag{2-29}$$

   and the non-vanishing solutions of the form $w(k) = gf(k)$ are obtained when the determinant of the system equals to zero. g is the group velocity and $f(k)$ denotes a function of k, which is the wavenumber.

3. D'Alembert's solution for a right traveling wave is considered such that

$$z^* - gt^*,$$

   is used over the space variable z^*.

4. Using long wave estimation (Appendix D), the scaling variable ϵ is introduced to scale the time variable and the new space variable:

$$\xi = \epsilon^{\frac{1}{2}}(z^* - gt^*), \quad \tau = \epsilon^{\frac{3}{2}} t^*. \tag{2-30}$$

5. The dimensionless variables are expressed as power series of ϵ:

$$v_z^* = \sum_{n=1}^{\infty} \epsilon^n v_n(\xi, \tau), \tag{2-31}$$

$$P^* = \sum_{n=1}^{\infty} \epsilon^n p_n(\xi, \tau), \tag{2-32}$$

$$\gamma^* = \sum_{n=1}^{\infty} \epsilon^n \gamma_n(\xi, \tau), \tag{2-33}$$

   and this power expansion is substituted into the non-dimensional equation. The terms scaled with ϵ^3 and higher powers are neglected under small ϵ assumption.

6. Perturbation expansion is done by grouping and solving the terms scaled with same powers of ϵ. In particular, this leads to three set of equations that scale with ϵ^0, ϵ^1 and ϵ^2 respectively.

7. Using realistic boundary conditions and solving for the terms scaled with ϵ^1, the expansion variables υ_1, p_1 and γ_1 are related to each other.

8. Using these relationships, the terms proportional to ϵ^2 are solved to relate υ_2, p_2 and γ_2 to υ_1, p_1 and γ_1. Then, the terms proportional to ϵ^2 are expressed in terms of υ_1, p_1 and γ_1 which leads to KdV type equations.

9. Solutions are provided for the original variables by estimating the dimensionless variables as a linear function of ϵ under small ϵ assumption:

$$\upsilon_z^* \simeq \epsilon \upsilon_1(\xi, \tau), \tag{2-34}$$
$$P^* \simeq \epsilon p_1(\xi, \tau), \tag{2-35}$$
$$\gamma^* \simeq \epsilon \gamma_1(\xi, \tau), \tag{2-36}$$

   and using the transformations back to the original variables, the 1-soliton solutions are derived for the original variables for P, υ_z and R in z and t.

Yomosa's 1-soliton solution for P is provided as

$$P(z,t) = P_d + \frac{6}{L} p_0 \kappa^2 \text{sech}^2 \left(\frac{\kappa}{L_0}(z - Vt) + \delta \right), \tag{2-37}$$

where P_d is the diastolic pressure, κ is the imaginary wavenumber, L, L_0 and p_0 are scaling parameters derived by Yomosa, V is the group velocity of the soliton and δ is the phase. Based on Yomosa's definitions the scaling parameters and V can be described in terms of model physical parameters:

$$p_0 = \frac{E h_0}{2R_0}, \tag{2-38}$$
$$L_0 = \sqrt{\frac{R_0 H_0 \rho_w}{2\rho}}, \tag{2-39}$$
$$L = \frac{K}{g}, \tag{2-40}$$
$$V = g c_0 (1 + 2\kappa^2), \tag{2-41}$$

with

$$K = \frac{(1+\gamma_0)\,(1+2a+3(2a-1)\gamma_0)}{4\,(1+(2a-1)\gamma_0)^{\frac{3}{2}}},$$
$$g = \frac{\sqrt{1+(2a-1)\gamma_0}}{1+\gamma_0},$$
$$c_0 = \sqrt{\frac{Eh_0}{2\rho R_0}},$$
$$\frac{P_d}{p_0} = \frac{2\gamma_0(1+a\gamma_0)}{(1+\gamma_0)^2}.$$

KdV equations for the original variables, P, υ_z and R are not provided explicitly in Yomosa's work. We will derive the KdV equation for P expressed in z and t following Yomosa's normalization steps. In Yomosa, the following KdV equation is provided for p_1:

$$\frac{\partial p_1}{\partial \tau} + Lp_1\frac{\partial p_1}{\partial \xi} + \frac{1}{2}\,\frac{\partial^3 p_1}{\partial \xi^3} = 0. \tag{2-42}$$

Following the normalization steps for time and space variables in Yomosa's work, ξ and τ can be described as a function of z and t:

$$\xi = \frac{\epsilon^{\frac{1}{2}}}{L_0}\,(z - gc_0t)\,, \quad \tau = \frac{\epsilon^{\frac{3}{2}}gc_0}{L_0}t \tag{2-43}$$

which is used to express Equation 2-42 in terms of z and t:

$$\frac{\partial p_1}{\partial t} + gc_0(1+\epsilon Lp_1)\frac{\partial p_1}{\partial z} + \frac{gc_0L_0^2}{2}\,\frac{\partial^3 p_1}{\partial z^3} = 0. \tag{2-44}$$

Following Yomosa's normalization steps, p_1 can be described as an affine function of P:

$$p_1 \simeq \frac{1}{\epsilon}P^* = \frac{1}{\epsilon p_0}(P - P_d), \tag{2-45}$$

which can be used to derive KdV-type dynamics for P:

$$\frac{\partial P}{\partial t} + \frac{gc_0L}{p_0}\,\left(\frac{p_0}{L} - P_d + P\right)\frac{\partial P}{\partial z} + \frac{gc_0L_0^2}{2}\,\frac{\partial^3 P}{\partial z^3} = 0. \tag{2-46}$$

The solution to this equation can be determined uniquely if the initial data decays sufficiently rapidly. The initial data is considered to be fixed in time:

$$P_{\text{ini}} = P(z, t_0). \tag{2-47}$$

In practical applications we are interested in solving for initial data fixed in z instead. This is due to the fact that clinical measurements of arterial blood pressure is done at fixed positions

making space evolution of interest over time evolution. Equation 2-46 can be converted timelike KdV equation referring to the work of Osborne and Petti [38]. First P is normalized such that the vertical offset is removed.

$$\hat{P} = P - P_d \tag{2-48}$$

which leads to the spacelike KdV Equation

$$\frac{\partial \hat{P}}{\partial t} + gc_0 \frac{\partial \hat{P}}{\partial z} + \frac{gc_0 L}{p_0} \hat{P} \frac{\partial \hat{P}}{\partial z} + \frac{gc_0 L_0^2}{2} \frac{\partial^3 \hat{P}}{\partial z^3} = 0. \tag{2-49}$$

Then, based on [38], the spacelike KdV Equation is converted to an estimated timelike form:

$$\frac{\partial \hat{P}}{\partial z} + \frac{1}{gc_0} \frac{\partial \hat{P}}{\partial t} - \frac{L}{gc_0 p_0} \hat{P} \frac{\partial \hat{P}}{\partial t} - \frac{L_0^2}{2} \frac{\partial^3 \hat{P}}{\partial t^3} = 0, \tag{2-50}$$

such that the associated initial data is fixed in position instead

$$\hat{P}_{\text{ini}} = P(z_0, t) - P_d. \tag{2-51}$$

2-5-2 Crépeau and Sorine's Model

In 2005, Crépeau and Sorine[7] proposed a reducel model describing the input-output behavior of an arterial compartment. Based on this model, the arterial blood pressure waveform is interpreted as finite number of solitons moving in forward direction and the contribution of the frictional effects is estimated by a Windkessel. In 2007, Créapau and Sorine revised their model for a different conference submission [9] and Laleg contributed to Crépeau and Sorine's work by proposing identification method for the soliton components [11]. In particular, in this subsection, the model and the derivations of [9] will be discussed and referred to by author name, Crépeau and Sorine.

In Crépeau and Sorine following model assumptions are made:

1. Blood is modeled as an isothermal, incompressible, Newtonian fluid (Section 2-3-1).
2. Viscous term in the blood dynamics is excluded (Section 2-3-2).
3. Frictional term in the blood dynamics is included but the coefficient of the term is not derived based on model physical parameters but rather taken as an arbitrary constant.
4. The blood vessel is modeled as an infinitely long, straight cylinder.
5. 1-D dynamics are used over 3-D dynamics (Section 2-4-1).
6. The vessel wall is modeled as a thin, homogenous, elastic membrane. Pressure is considered to be a linear dynamical function of the vessel cross-sectional area, which makes it a nonlinear function of vessel radius.

Based on the aforementioned assumptions Crépeau and Sorine's system equations are given as

$$\frac{\partial Q_z}{\partial t} + \frac{\partial}{\partial z}\left(\frac{Q_z^2}{A}\right) + \frac{1}{\rho}A\frac{\partial P}{\partial z} + b\frac{Q_z}{A} = 0, \tag{2-52}$$

$$\frac{\partial A}{\partial t} + \frac{\partial Q_z}{\partial z} = 0, \tag{2-53}$$

$$P = \frac{Eh_0}{2R_0^3}(R - R_0)(R + R_0) + \frac{2\rho_w h_0}{R_0}\left[R\frac{\partial^2 R}{\partial t^2} + \left(\frac{\partial R}{\partial t}\right)^2\right], \tag{2-54}$$

where $Q_z = Q_z(z,t)$ is the volumetric flow rate, $P = P(z,t)$ is the pressure, $R = R(z,t)$ is the vessel radius, $A = A(z,t) = \pi R^2$ is the vessel cross-sectional area, ρ is the blood density, b is the coefficient of the frictional term, E is the elastic Young's modulus, h_0 is the reference vessel wall thickness, R_0 is the reference vessel radius and ρ_w is the vessel wall density. The reference length measurements are taken at $P = 0$.

Using various derivations, Crépeau and Sorine reduces this set of equations to three KdV equations for Q_z, P and A in a boundary layer. Crépeau and Sorine's derivations can be summarized as follows:

1. z, t, Q_z, P and A are scaled to dimensionless variables z^*, t^*, Q_z^*, P^* and A^* using physical model parameters. The dimensionless variables are used to convert Equations 2-52, 2-53 and 2-54 to non-dimensional form.

2. D'Alembert's solution for a right traveling wave is considered such that

   $$t^* - z^*,$$

   is used over the time variable t^*.

3. Using long wave estimation (Appendix D), the scaling variable ϵ is introduced to scale the space variable and the new time variable:

   $$\tau = \frac{t^* - z}{\epsilon^2}, \quad \xi = \frac{z^*}{\epsilon}. \tag{2-55}$$

   An explicit definition for ϵ is also provided:

   $$\epsilon = \left(\frac{R_0}{L_0}\right)^{\frac{2}{5}}, \tag{2-56}$$

   where L_0 is the typical wave length of the waves propagating in the tube.

4. The dimensionless variables are expressed as power series of ϵ:

   $$Q_z^* = \sum_{n=1}^{\infty} \epsilon^n Q_n(\xi,\tau), \tag{2-57}$$

   $$P^* = \sum_{n=1}^{\infty} \epsilon^n p_n(\xi,\tau), \tag{2-58}$$

   $$A^* = \sum_{n=1}^{\infty} \epsilon^n A_n(\xi,\tau), \tag{2-59}$$

and this power expansion is substituted into the non-dimensional equation. The terms scaled with ϵ^3 and higher powers are neglected under small ϵ assumption.

5. Perturbation expansion is done by grouping and solving the terms scaled with same powers of ϵ. In particular, this leads to three set of equations that scale with ϵ^0, ϵ^1 and ϵ^2 respectively.

6. Using the relationships of the variables and assuming fast times in a boundary layer, the equations obtained from the perturbation expansion are solved for Q_1, p_1 and A_1, leading to KdV type equations in timelike form.

7. The dimensionless variables are estimated as an linear function of ϵ under small ϵ assumption:

$$Q_z^* \simeq \epsilon Q_1(\xi, \tau), \tag{2-60}$$
$$P^* \simeq \epsilon p_1(\xi, \tau), \tag{2-61}$$
$$A^* \simeq \epsilon A_1(\xi, \tau). \tag{2-62}$$

and using the transformations back to the original variables from dimensionless variables, the KdV equation for Q_z is obtained.

8. The frictional effects are neglected based on fast times in a boundary layer assumption, but assuming large time or space a parabolic equation for Q_z is obtained instead:

$$\frac{\partial Q_z}{\partial t} - \frac{A_0 h_0 E}{2\rho b R_0} \frac{\partial^2 Q_z}{\partial z^2} = 0, \tag{2-63}$$

whose low frequency approximation is used to estimate a 2 or 3 element Windkessel.

In Crépeau and Sorine's work, the KdV equation representing the fast blood flow is provided in initial variables:

$$\frac{\partial Q_z}{\partial z} + d_0 \frac{\partial Q_z}{\partial t} + d_1 \frac{\partial Q_z}{\partial t} Q_z + d_2 \frac{\partial^3 Q_z}{\partial t^3} = 0, \tag{2-64}$$

with

$$d_0 = \frac{1}{c_0}, \quad d_1 = -\frac{3}{2A_0 c_0^2}, \quad d_2 = -\frac{\rho_w h_0 R_0}{2\rho c_0^3}, \tag{2-65}$$

where c_0 is Moens-Korteweg velocity of a wave propagating in an elastic tube and defined as

$$c_0 = \sqrt{\frac{E h_0}{2\rho R_0}}. \tag{2-66}$$

The 1-soliton solutions for Q_z and P are not explicitly provided in Crépeau and Sorine. First we will derive the denormalized 1-soliton solution for Q_z following the normalization steps in Crépeau and Sorine. Consider a standard KdV equation of the form

$$\frac{\partial U}{\partial Z} + 6\frac{\partial U}{\partial T}U + \frac{\partial^3 T}{\partial Z^3} = 0, \tag{2-67}$$

whose 1-soliton solution is given as

$$U(Z,T) = \frac{1}{2}\kappa^2 \text{sech}^2\left(\frac{\kappa}{2}(T - \kappa^2 Z) + \delta\right). \tag{2-68}$$

Using the following transformations [11]

$$T = t - d_0 z, \quad Z = d_2 z, \quad U = \frac{d_1}{6d_2} Q_z \tag{2-69}$$

the denormalized 1-soliton solution for Equation 2-64 can be derived as

$$Q_z(z,t) = \frac{3d_2}{d_1}\kappa^2 \text{sech}^2\left(\frac{\kappa}{2}(t - d_0 z - d_2\kappa^2 z) + \delta\right), \tag{2-70}$$

where κ is the imaginary wavenumber and δ is the phase. The 1-soliton solution for P can be calculated using the following equations provided in Crépeau and Sorine:

$$Q_z = A_0 c_0 Q_1, \quad P = \rho c_0^2 P_1 + P_d, \quad P_1 = Q_1, \tag{2-71}$$

leading to the 1-soliton solution for P:

$$P(z,t) = P_d + \frac{3\rho c_0 d_2}{A_0 d_1}\kappa^2 \text{sech}^2\left(\frac{\kappa}{2}(t - d_0 z - d_2\kappa^2 z) + \delta\right). \tag{2-72}$$

The linear transformations in Equation 2-71 can used along with Equation 2-64 to derive KdV-type dynamics for P:

$$\frac{\partial P}{\partial z} + \left(d_0 - \frac{A_0}{\rho c_0}P_d\right)\frac{\partial P}{\partial t} + d_1\left(\frac{A_0}{\rho c_0}\right)P\frac{\partial P}{\partial t} + d_2\frac{\partial^3 P}{\partial t^3} = 0. \tag{2-73}$$

P is normalized to remove the vertical offset so that

$$\hat{P} = P - P_d, \tag{2-74}$$

which leads to the KdV Equation

$$\frac{\partial \hat{P}}{\partial z} + d_0\frac{\partial \hat{P}}{\partial t} + d_1\left(\frac{A_0}{\rho c_0}\right)\hat{P}\frac{\partial \hat{P}}{\partial t} + d_2\frac{\partial^3 \hat{P}}{\partial t^3} = 0. \tag{2-75}$$

The associated initial data for the problem then becomes

$$\hat{P}_{\text{ini}} = P(z_0,t) - P_d. \tag{2-76}$$

2-6 Model Matching

The simulation model and the KdV models have different model assumptions, so these differences have to be addressed for the verification of KdV type dynamics and soliton solutions. We propose imposing consistency between models by adjusting the physical model parameters of KdV models.

2-6-1 Fundamental Challenges of Testing Korteweg-de Vries Dynamics

Yomosa [6] and Crépeau and Sorine [9] both use 1-D Navier-Stokes equations as their initial model. In both works, using additional and differing assumptions, KdV type dynamics are derived. In fact, 1-D Navier-Stokes equations for large arteries themselves depend on underlying assumptions. In Figure 2-7, the flowchart that shows the hierarchy of the assumptions is provided.

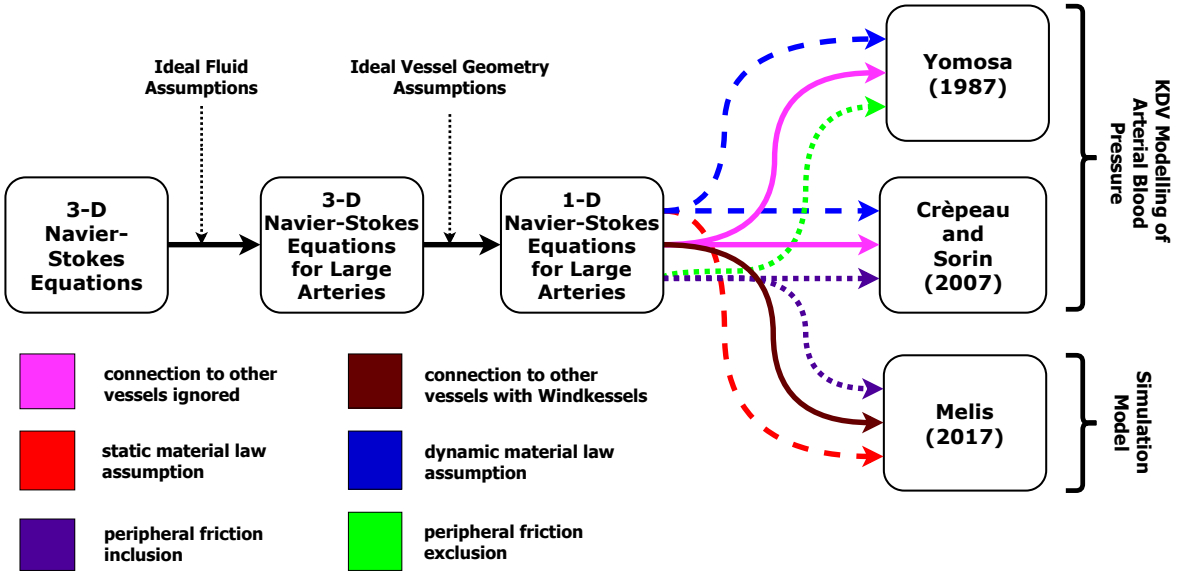

Figure 2-7: The blood flow assumptions of Yomosa [6], Crépeau and Sorine [9] and Melis [10]

Based on Figure 2-7 the differences between Yomosa [6], Crépeau and Sorine [9] and Melis's [10] model are explained by differing material law assumptions, inclusion of peripheral friction in the flow dynamics and connection to other vessels. Melis's model will be referred to as the simulation model in our paper.

The simulation model's material law is static and the pressure is considered to be a linear function of vessel radius at the reference pressure. Same material law is in fact commonly used throughout the 1-D compliant artery modelling and verification literature [39, 23, 40, 37, 41]. On the other hand, Yomosa's and Crépeau and Sorine's models' material laws are dynamic in nature due to the inclusion of time derivatives. In particular, Yomosa derives KdV type dynamics for the radius, whereas Crépeau and Sorine derives KdV type dynamics for the cross-section which rely on the inclusion of the dynamic components in the material law. The dynamic terms in the material law also depend on additional physical model parameters which are not used by the simulation. As these parameters are physical in nature, such as the vessel

wall density, it is possible to refer to literature to come up with valid values. Unfortunately this is not the case for all additional parameters assumed by Yomosa - although Yomosa derives a soliton solution based on physical parameters, in his benchmark tests two of the additional parameters, specifically nonlinear coefficient of elasticity, a, and thickness of the arterial wall that does not participate in elastic deformation, h', are treated as fit variables based on additional assumptions on the solution. To the extent of our knowledge, these particular parameters do not have reference values or even ranges in the existing literature. Testing Yomosa's solution for a range of these values is also problematic in nature as the simulation model's material law lacks a dynamic component, making *over-fitting* a relevant problem for testing Yomosa's model.

Another difference between the models arises from the inclusion or exclusion of terms in the 1-D Navier-Stokes momentum equation. The simulation model and Crépeau and Sorine's model both include frictional term in the dynamics, whereas Yomosa's model does not. As the inclusion of friction correspond to energy losses over wave propagation, this violates the energy conservation principles of the soliton solutions over large space or time propagation. This in fact explains why Yomosa's model can not explain the decrease of pressure as function of increasing longitudinal distance. Crépeau and Sorine tackles this issue, by restricting the definition of proposed soliton solutions to boundary layers which removes the effects of the friction due to fast times assumption. For large space or time propagation, the effects of friction is estimated with a 2 or 3-element Windkessel (described in Figures 2-2 and 2-3 respectively). In the simulation model, peripheral friction is included in the dynamics and is derived based on Equation 2-24. Setting the viscosity parameter, μ, to zero in the simulation initialization file can eliminate the effects of peripheral friction. The existing literature on 1-D modelling of compliant arteries accounts for the effects of friction in the flow dynamics [39, 40, 37, 41, 10] so in our tests we will include the effects of friction in the dynamics as well.

Last but not least, assumption on connection to other vessels plays an important part in the arterial blood pressure dynamics. In Yomosa's model, the artery is assumed to be infinitely long, which means physical reflections caused by the interconnections of arteries are neglected. In Crépeau and Sorine, the assumptions on reflections are not explicitly addressed; specifically Crépeau and Sorine restrict their derivations to describe the dynamics of the arterial compartment of a single artery. In the simulation, connections to other vessels can be accounted for by imposing outlet boundary conditions using 2 or 3-element Windkessels. Alternatively, the *reflection type outlet* can be chosen in the simulation model and by setting the reflection parameter, R_t, to zero, the connections to other vessels can be neglected to match the assumptions of Yomosa's and Crépeau and Sorine's model. In our tests, the effects of connections to the other vessels will be considered as clinical pressure measurements are subject to the interconnection effects. Windkessels can represent the effects of interconnection in a simple manner by assigning a hydraulic impedance at the outlet which can be effective to explain the steepening phenomena (described in Section 2-2-1). In contrast, Crépeau and Sorine describe the Windkessel dynamics based derivations of 1-D Navier-Stokes equations and the assumed material law. The values of the Windkessel elements are not explicitly given in Crépeau and Sorine but treated as fit variables in the benchmark tests with real patient pressure measurements. As the experimental data is subject to network effects, the fitted Windkessel elements might be representing effects beyond friction in the dynamics. In our paper, the 3-element Windkessels will be used to model reflections caused by network effects,

consistent with its definition in the simulation model.

The ideal fluid and vessel geometry assumptions used for the derivation of 1-D Navier-Stokes equations (Figure 2-7) also impose fundamental limitations on physiological implications of our testing. Xiao et al. [37] address the ideal vessel geometry assumptions by comparing 1-D and 3-D compliant artery models using consistent physical parameters and boundary conditions. Based on the results of Xiao et al., both formulations are in good agreement. The ideal fluid assumptions will not be fully addressed in the scope of our work. The incompressible fluid behavior is an estimation of a conceptually unphysical phenomenon; as a truly incompressible fluid would require the sound waves to travel at an instant throughout the fluid, violating the concept of causality. In the smaller vessels non-Newtonian effects may also play a role [30] and these effects may be potentially relevant for larger vessels. In a nutshell, 1-D Navier-Stokes representation may not be able to represent the real physiological phenomena accurately. Addressing such a problem would require benchmarking 1-D Navier-Stokes equations against accurate *in vivo* measurements, which might be challenging in its own way as pressure and flow relationship of human subjects differ in an individual level and between different groups. This the main reason, we want to test KdV type dynamics and associated soliton solutions against 1-D Navier-Stokes equations, as this approach removes dependencies on ideal fluid and vessel geometry assumptions in the reference and tested behavior. To verify KdV type equations for arterial blood pressure, the ideal fluid and ideal vessel geometry assumptions have to be properly addressed to verify results at the physiological level.

2-6-2 Blood Flow Simulation Software and Model

openBF is an open-source 1D blood flow solver based on MUSCL finite-volume numerical scheme, written in Julia and released under Apache 2.0 free software license. The documentation of openBF, the benchmark tests that compares the results with existing modeling literature is provided in the PhD dissertation of Melis [10].

The blood flow model of openBF is based on the following model assumptions:

1. Blood is modeled after an incompressible and isothermal Newtonian fluid. This assumption is used for the derivation of 3-D Navier Stokes equations (Section 2-3-1).

2. Viscosity term in the blood dynamics is excluded (Section 2-3-2).

3. The vessel is modeled after a thin axisymmetric cylinder which is used to reduce the 3-D dynamics to 1-D (Section 2-4-1).

4. The friction model is derived under polynomial radial velocity profile assumption (Section 2-4-2).

5. The vessels are straight and have linearly elastic compliant walls (Section 2-4-3).

The simulation model is given as follows:

$$\frac{\partial Q_z}{\partial t} + \frac{\partial}{\partial z}\left(\frac{Q_z^2}{A}\right) + \frac{A}{\rho}\frac{\partial P}{\partial z} + 2\frac{\mu}{\rho}(\Gamma + 2)\frac{Q}{A} = 0, \tag{2-77}$$

$$\frac{\partial A}{\partial t} + \frac{\partial Q_z}{\partial z} = 0, \tag{2-78}$$

$$P = \frac{4Eh_0}{3R_0^2}(R - R_0), \tag{2-79}$$

where t is time, z is the longitudinal position, $R = R(z,t)$ is the vessel radius, $A = A(z,t) = \pi R^2$ is the vessel cross-sectional area, Q_z is the longitudinal volumetric flow rate, P is the blood pressure, ρ is the blood density, μ is the blood viscosity, Γ is the polynomial fit order assumed for the radial velocity profile, E is the vessel wall elastic Young's modulus, h_0 is the reference vessel wall thickness and R_0 is the reference vessel radius. In this paper, Equations 2-77, 2-78 and 2-79 will be referred to as the simulation's equation of motion, mass conservation principle and material law respectively. As an important remark, the solver has the hybrid model structure described in Figure 2-5. The system boundary conditions are applied to the inlet and the outlet of the vessel. The inlet boundary conditions describe the time evolution fixed at the initial location and can be in terms of P or Q based on user choice:

$$P_{\text{in}}(t) = P(z_0, t), \tag{2-80}$$

$$Q_{\text{in}}(t) = Q(z_0, t), \tag{2-81}$$

where P_{in} and Q_{in} are the considered pressure and volumetric flow rate boundary conditions at the inlet respectively. The solver assumes the time data to be normalized on the cardiac cycle period, T_c. Therefore the boundary conditions are expected to represent the values within a cardiac cycle, with time data scaled to the domain $[0, 1]$. The inlet boundary conditions are treated as periodic.

The user is expected to enter model physical parameters in a *yml* file. In this file also solver parameters have to be specified. The solver runs for multiple cardiac cycles until the difference between the output signals in the current and previous cycle are found be within the user defined error tolerance. The maximum number of cardiac cycles and the number of timesteps included in the outputs can be specified as well.

Outlet boundary conditions should be chosen based on the assumptions to other vessels. If the vessel is not connected to another vessel the reflection type outlet should be chosen and the reflection coefficient, R_t, has to be provided. If the vessel is connected to another vessel, 2 or 3-element Windkessel type outlets should be chosen and then the values of Windkessel elements have to be provided.

If a network of arteries are simulated, the junctions of the components have to be specified. The inlet boundary conditions have to be assigned only to the input components of the network. Outlet types and parameters, have to be assigned only to the output components.

2-6-3 Yomosa's and Simulation Model Matching

Yomosa's material law (Equation 2-28) is different compared to the simulation's material law (Equation 2-79). In particular, in Yomosa's model [6]:

1. The acceleration of the vessel radius is included in the material law resulting with a dynamic material law instead of a static one.

2. P is a quadratic function of R, if the nonlinear coefficient of elasticity a is non-zero and the acceleration term is ignored.

3. P is scaled with 1 instead of $\frac{4}{3}$, if the acceleration term is ignored.

These steps are proposed for imposing consistency between Yomosa's model and the simulation model.

1. The acceleration term in Yomosa's material law can not be taken into consideration by the simulation model which assumes a static material law. However neglecting this mismatch between the models is a reasonable option as the scaling of the acceleration term is very small; in standard units ρ_w scales with 10^3, H scales with 10^{-3} and within a cardiac cycle P variation scales with 10^4.

2. The acceleration term in Yomosa's material law is scaled by ρ_w and H which are not considered parameters in the simulation model but are included in Yomosa's soliton solution. Furthermore as the inclusion of dynamics in the material law is fundamental to the derivation of Yomosa's solution, the acceleration term can not be cancelled by setting ρ_w or H to zero. ρ_w will be considered to match ρ used in the simulation model as the vessel wall density and the blood density are almost equal in the physiological systems leading to the relation:

$$\rho_w = \rho. \tag{2-82}$$

   Yomosa defines H as the sum of h, which is the vessel thickness that participates in the elastic deformation and h', the vessel thickness that does not [6]. Although the value of H at the reference pressure, H_0, is included as a parameter in Yomosa's solution, the parameter is treated as a fit parameter in Yomosa's benchmark tests. In Yomosa, H_0 is estimated based on additional assumptions on the solution which makes Yomosa's estimates of H_0 questionable for generic applications. Due to this, the thickness of the wall that does not participate in elastic deformation will be ignored in the solution, leading to the equation:

$$H_0 = h_0. \tag{2-83}$$

   This also imposes consistency between Yomosa's and simulation model as in the simulation model entire vessel thickness is considered to participate in linear deformation.

3. If the acceleration term is ignored, Yomosa's material law can be reduced to a linear static function as the simulation model when a is set to zero. Since the simulation model has a linear static law, a will be set as zero to match model behavior:

$$a = 0. \tag{2-84}$$

4. E is scaled by a factor of $\frac{4}{3}$ to compensate for the coefficient difference between the models:

$$E_Y = \frac{4}{3}E. \tag{2-85}$$

Yomosa introduces E only for the material law and does not use it in intermediate steps beyond this context so the coefficient can be absorbed without changing the nature of the solution.

The matched Yomosa's 1-soliton solution for P is given as

$$P(z,t) = P_d + \frac{6}{L}p_0\kappa^2 \text{sech}^2\left(\frac{\kappa}{L_0}(z - Vt) - \delta\right), \tag{2-86}$$

where κ is the imaginary wavenumber, L, L_0 and p_0 are scaling parameters derived by Yomosa, V is the group velocity of the pressure soliton and δ is the phase. To address material law inconsistencies, it is assumed that $a = 0$, $\rho_w = \rho$, $H_0 = h_0$ and $E_Y = \frac{4}{3}E$. The matched scaling parameters and the matched V can be described in terms of model physical parameters:

$$p_0 = \frac{E_Y h_0}{2R_0}, \tag{2-87}$$

$$L = \frac{K}{g}, \tag{2-88}$$

$$L_0 = \sqrt{\frac{R_0 h_0}{2}}, \tag{2-89}$$

$$V = gc_0\left(1 + 2\kappa^2\right), \tag{2-90}$$

with

$$K = \frac{(1+\gamma_0)(1-3\gamma_0)}{4(1-\gamma_0)^{\frac{3}{2}}},$$
$$g = \frac{\sqrt{1-\gamma_0}}{1+\gamma_0},$$
$$c_0 = \sqrt{\frac{E_Y h_0}{2\rho R_0}},$$
$$\frac{P_d}{p_0} = \frac{2\gamma_0}{(1+\gamma_0)^2}.$$

The matched parameters can be plugged into the timelike KdV equation (Equation 2-50), leading to the matched KdV equation

$$\frac{\partial \hat{P}}{\partial z} + \frac{1}{gc_0}\frac{\partial \hat{P}}{\partial t} - \frac{L}{gc_0 p_0}\hat{P}\frac{\partial \hat{P}}{\partial t} - \frac{L_0^2}{2}\frac{\partial^3 \hat{P}}{\partial t^3} = 0. \tag{2-91}$$

with

$$\hat{P} = P - P_d. \tag{2-92}$$

The associated initial data for the match KdV equation is

$$\hat{P}_{\text{ini}} = P(z_0, t) - P_d. \tag{2-93}$$

2-6-4 Crépeau and Sorine's and Simulation Model Matching

Crépeau and Sorine's material law (Equation 2-54) is different compared to the simulation's material law (Equation 2-79). In particular, in Crépeau and Sorine's model:

1. The acceleration of the vessel cross-section is included in the material law resulting with a dynamic material law instead of a static one.
2. P is a linear function of A which makes it a quadratic function of R, if the acceleration term is ignored.
3. P is scaled with 1 instead of $\frac{4}{3}$, if the acceleration term is ignored.

These steps are proposed for imposing consistency between Crépeau and Sorine's model and the simulation model.

1. The acceleration term in Crépeau and Sorine's material law can not be taken into consideration by the simulation model which assumes a static material law. However neglecting this mismatch between the models is a reasonable option as the scaling of the acceleration term is very small; in standard units ρ_w scales with 10^3, h_0 scales with 10^{-3} and within a cardiac cycle P variation scales with 10^4.
2. The acceleration term in Crépeau and Sorine's material law is scaled by ρ_w which is not a considered parameter in the simulation model but is included in Crépeau and Sorine's model and solution. Furthermore as the inclusion of dynamics in the material law is fundamental to derivation of the Crépeau and Sorine's solution, the acceleration term can not be cancelled by setting ρ_w to zero. ρ_w will be considered to match ρ used in the simulation model as the vessel wall density and the blood density are almost equal in the physiological systems leading to the relation:

$$\rho_w = \rho. \tag{2-94}$$

3. If the acceleration term is ignored, Crépeau and Sorine's material is a linear function of A which makes it a quadratic function of R as $a = \pi R^2$. To address this issue, we are defining the following optimization problem

$$\min_{E_C} \int_{R_d}^{1.04R_d} \left(\frac{4E(R - R_0)}{3} - \frac{E_C(R^2 - R_0^2)}{2R_0} \right)^2 dR, \tag{2-95}$$

which returns Young modulus E_C that will be used in the matched model instead of E. The optimization problem minimizes the 2-norm of the difference between the static contribution of the material laws between the range $[R_d,\ 1.04R_d]$. R_d is the radius at the diastolic pressure and can be calculated using Equation 2-79:

$$R_d = \frac{3R_0^2}{4Eh_0}P_d + R_0. \tag{2-96}$$

The upper range in the integral, $1.04R_d$ is determined based on Chen et al. [42] which states that the radius stretch rate is less than 4% in the real arteries. As E_C depends on physical model parameters in this formulation, the value of it will be provided in the tests. It should be noted that the optimization problem has an analytical result but due to its complex form the exact solution is not provided. Crépeau and Sorineintroduce E only for the material law and does not use it in intermediate steps beyond this context so the coefficient can be absorbed without changing the nature of the solution.

The matched Crépeau and Sorine's 1-soliton solution for P is given as

$$P(z,t) = P_d + \frac{3\rho c_0 d_2}{A_0 d_1}\kappa^2 \mathrm{sech}^2\left(\frac{\kappa}{2}(t - d_0 z - d_2\kappa^2 z) + \delta\right). \tag{2-97}$$

where κ is the imaginary wavenumber and δ is the phase with

$$A_0 = \pi R_0^2, \quad c_0 = \sqrt{\frac{E_C h_0}{2\rho R_0}}, \quad d_0 = \frac{1}{c_0}, \quad d_1 = -\frac{3}{2A_0 c_0^2}, \quad d_2 = -\frac{h_0 R_0}{2c_0^3}. \tag{2-98}$$

The matched parameters can be plugged into the timelike KdV equation (Equation 2-75), leading to the matched KdV equation

$$\frac{\partial \hat{P}}{\partial z} + d_0\frac{\partial \hat{P}}{\partial t} + d_1\left(\frac{A_0}{\rho c_0}\right)\hat{P}\frac{\partial \hat{P}}{\partial t} + d_2\frac{\partial^3 \hat{P}}{\partial t^3} = 0 \tag{2-99}$$

with

$$\hat{P} = P - P_d. \tag{2-100}$$

The associated initial data for the matched KdV equation is

$$\hat{P}_{\mathrm{ini}} = P(z_0,t) - P_d. \tag{2-101}$$

Chapter 3

Systems and Control Part

3-1 Case Studies and Physical Model Parameters

We are considering the simplified arterial network and case studies described in Figure 3-1.

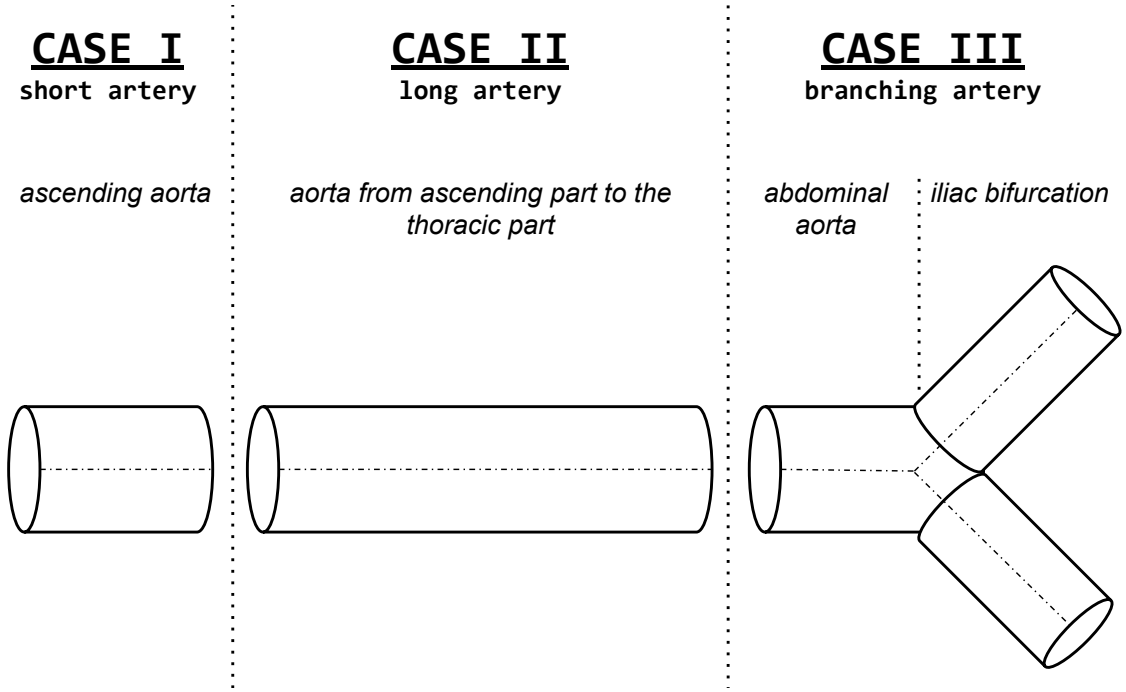

Figure 3-1: The simple artery network and case studies used for simulations.

In all cases, curvature and tapering of the vessels are neglected. The branching of aorta except Case III is also neglected. The simplified artery network output is considered to represent the arterial network from aortic root to the end of iliac bifurcation. The output of the previous

case is considered to be the input of the next case, however in some tests the cases will be treated independently.

For all simulations, the number of time steps is set to 600 and the error tolerance is set to 0.1%. The rest of the solver parameters are taken as default.

In the simulations, the connections to other arteries will be addressed using a 3-element Windkessel and the frictional effects will be also included. As a reminder, the matched KdV models are derived based on the exclusion of both connection to other vessels and peripheral friction. If the tested and the reference behavior is found to be significantly different, first only the connection to other vessels, then both the connection to other vessels and the peripheral friction will be excluded to test whether the mismatch is explained by any of these factors. This way we can test the modeling capabilities of the matched KdV models beyond their derivation assumptions and also understand whether the derivation of KdV type dynamics from 1-D Navier-Stokes equations under derivation assumptions changes the original behavior.

3-1-1 Case I: Short Artery

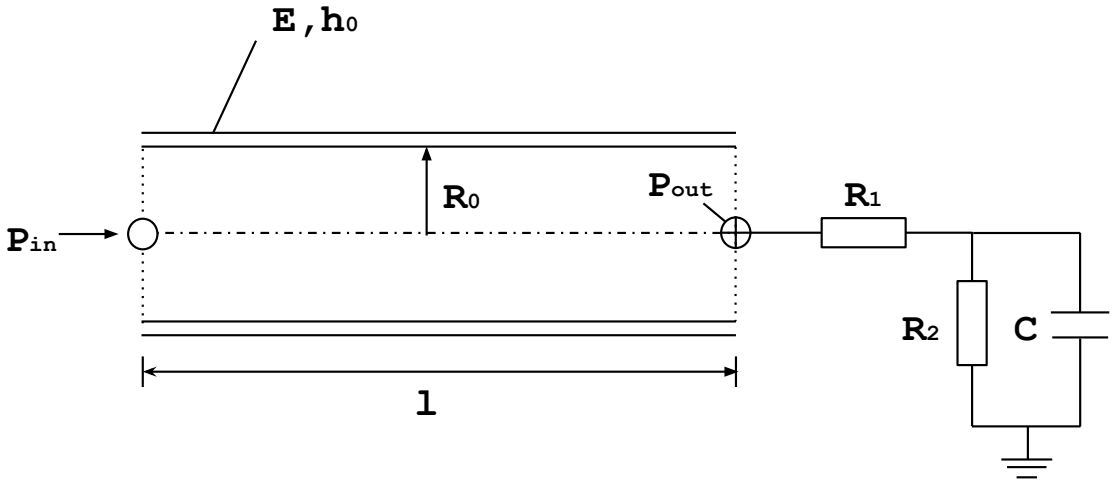

Figure 3-2: Technical drawing of the ascending aorta.

The short artery is modeled after the human ascending aorta. The technical diagram of the ascending aorta is provided in Figure 3-2.

The physical model parameters are taken from Melis [10] except the value of Young modulus, E, which is taken from Westerhof et al. [23] and are provided in Table 3-1.

Table 3-1: The physical model parameters of the human ascending aorta [10, 23].

Parameter	Value
Length, l	4.00 cm
Radius at reference pressure, R_0	1.47 cm
Wall thickness at reference pressure, h_0	1.65 mm
Young's modulus, E	400 kPa
Windkessel resistance 1, R_1	1.31×10^{7} Pa s m^{-3}
Windkessel resistance 2, R_2	2.22×10^{7} Pa s m^{-3}
Windkessel compliance C, C	1.61×10^{-8} Pa^{-1} m^{3}

3-1-2 Case II: Long Artery

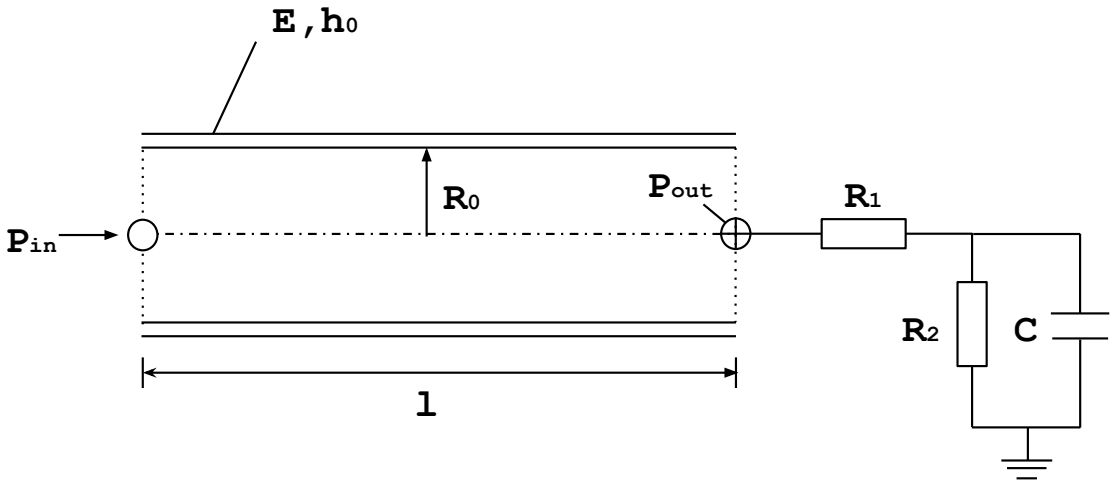

Figure 3-3: Technical drawing of the aorta from ascending part to the thoracic part.

The long artery is modeled after the human aorta from ascending part to the thoracic part. The technical diagram of the ascending aorta is provided in Figure 3-3.

The physical model parameters are taken from Melis [10] and are provided in Table 3-2.

Table 3-2: The physical model parameters of the human aorta, from ascending part to the thoracic part [10].

Parameter	Value
Length, l	24.1 cm
Radius at reference pressure, R_0	9.87 mm
Wall thickness at reference pressure, h_0	0.82 mm
Young's modulus, E	400 kPa
Windkessel resistance 1, R_1	1.17×10^{7} Pa s m^{-3}
Windkessel resistance 2, R_2	1.12×10^{8} Pa s m^{-3}
Windkessel compliance C, C	1.02×10^{-8} Pa^{-1} m^{3}

3-1-3 Case III: Branching Artery

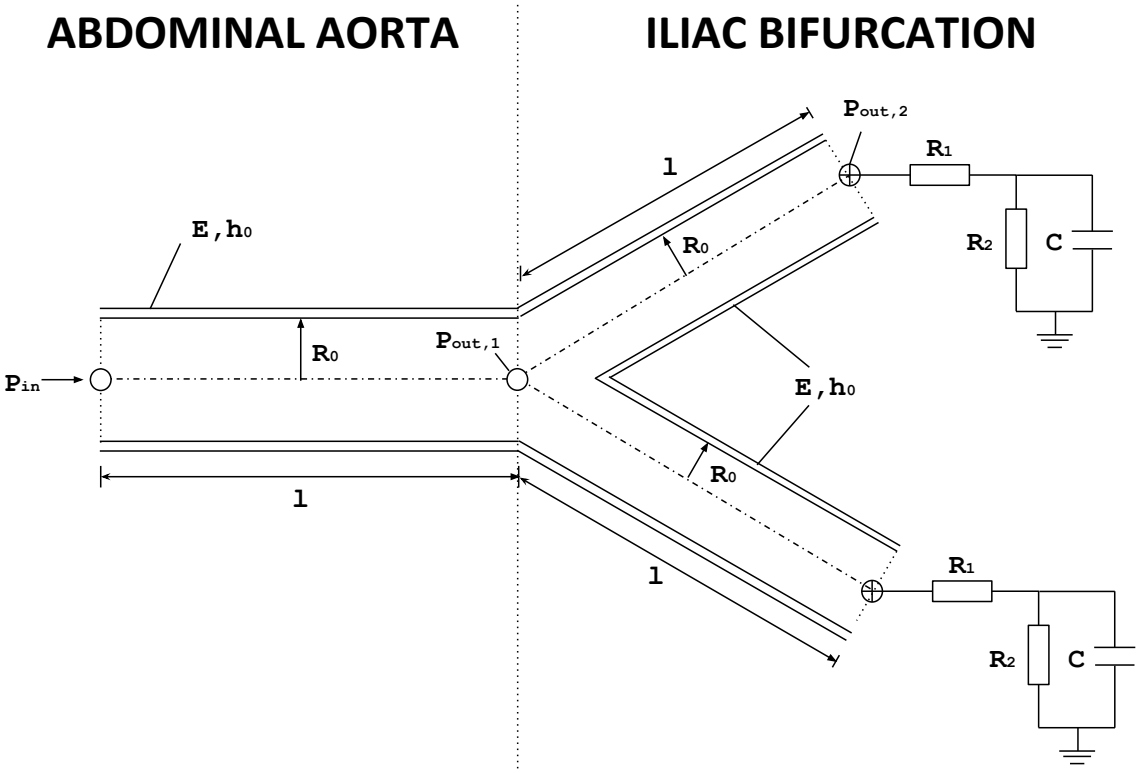

Figure 3-4: Technical Drawing of the abdominal aorta and the iliac bifurcation.

The network comprising of the human abdominal aorta and the human iliac bifurcation is considered for the third case study. The technical diagram of the network is provided in Figure 3-4. The input to the abdominal aorta is considered as the input to the network. The distal end of the abdominal aorta is considered to be connected to the proximal ends of iliac bifurcation which consists of two identical arteries. In the tests, the interconnection point of

the arteries is taken as the the first reference output and the output of one of the identical iliac arteries is taken as the second reference output.

The physical model parameters are taken from Melis [10]. The physical parameters of the abdominal aorta and iliac bifurcation components are provided in Tables 3-3 and 3-4 respectively.

Table 3-3: The physical model parameters of the abdominal aorta component

Parameter	Value
Length, l	8.60 cm
Radius at reference pressure, R_0	7.58 mm
Wall thickness at reference pressure, h_0	0.900 mm
Young's modulus, E	500 kPa

Table 3-4: The physical model parameters of the iliac bifurcation components

Parameter	Value
Length, l	8.50 cm
Radius at reference pressure, R_0	5.49 mm
Wall thickness at the reference pressure, h_0	0.680 mm
Young's modulus, E	700 kPa
Windkessel resistance 1, R_1	6.81×10^{7} Pa s m^{-3}
Windkessel resistance 2, R_2	3.10×10^{9} Pa s m^{-3}
Windkessel compliance C, C	3.67×10^{-10} Pa^{-1} m^{3}

3-2 Verification of the Matched KdV Models

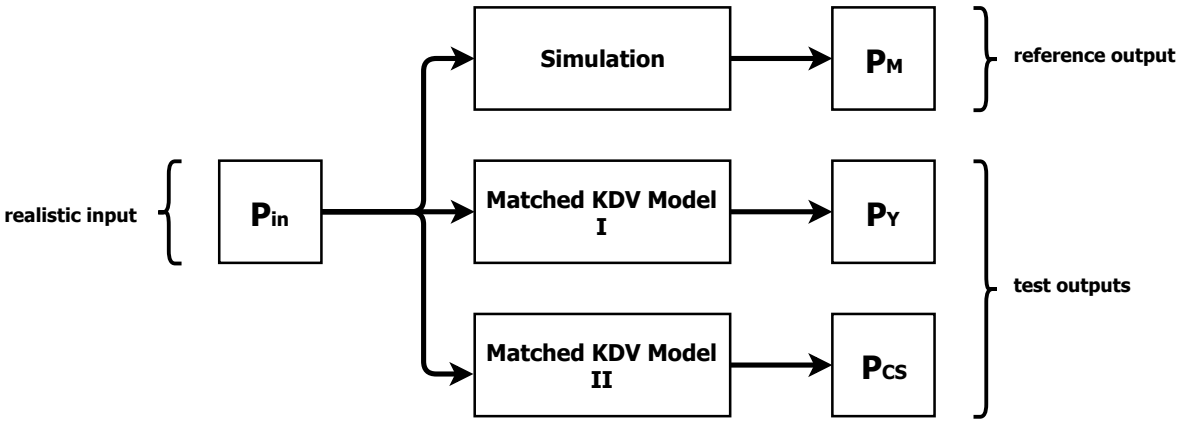

Figure 3-5: KdV verification test flowchart followed in each case study.

The flowchart of the verification test of the matched KdV models are provided in Figure 3-5. For the verification of the matched KdV models, we employ using a realistic inlet pressure data. The pressure output of the simulation, P_M, is considered to be the reference output. Using the same inlet, both timelike matched KdV equations (Equations 2-50 and 2-75) will be used to calculate the pressure at the outlet, P_Y and P_{CS}, corresponding to the output of the matched Yomosa model and the matched Crépeau and Sorine model respectively. The normalized 2-norm error between the reference and the matched KdV outputs will be used to evaluate the match:

$$\varepsilon_{\mathrm{Y}} = \frac{||P_M - P_Y||_2}{||P_M||_2}, \quad \varepsilon_{\mathrm{CS}} = \frac{||P_M - P_{CS}||_2}{||P_M||_2}, \tag{3-1}$$

where ε_{Y} is the error of the matched Yomosa model and $\varepsilon_{\mathrm{CS}}$ is the error of the matched Crépeau and Sorine model. The inlet boundary conditions for Case I is manually extracted from Brown et al. [43]. The pressure at the inlet is provided in Figure 3-6.

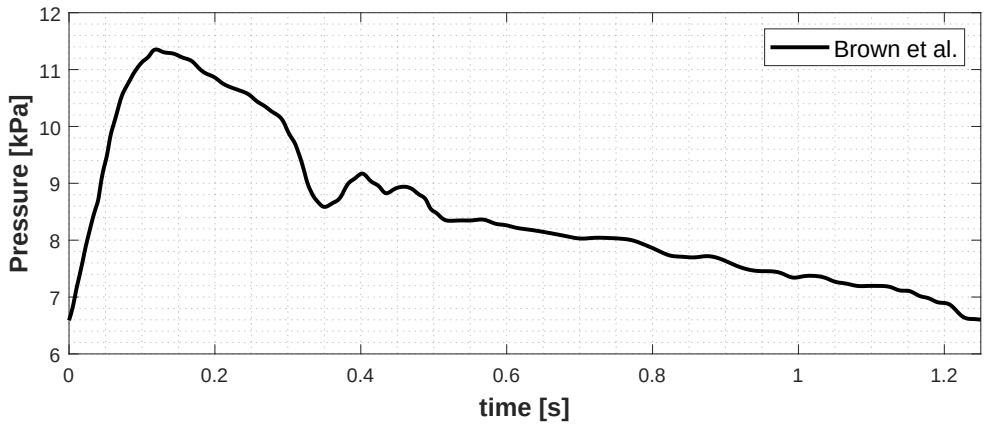

Figure 3-6: The manually extracted pressure data [43].

The blood density and the blood viscosity is also taken from Brown et al. [43] as 1056 kgm^{-3} and 3.5×10^{-3} Pa s respectively. The inlet boundary conditions for the other cases is taken as the simulation's pressure output from the previous case. Diastolic pressure, P_d, is calculated as the minimum value of the inlet pressure in each case.

For the matched model output calculations Chebfun is used, which is an open-source package for computing with functions to about 15-digit accuracy that runs on MATLAB [44]. The pressure at the inlet is converted to *chebfun* data type using interpolation of 100 point Chebyshev grid of the second kind using periodic boundary conditions. For the solution, *spin* function is used using 1000 time steps in the cardiac cycle ($T_C = 1.25\ s$). The position is discretized using 1 mm steps.

3-2-1 Short Artery Results

The measured and optimized parameters used for the matched models are

$$P_d = 6.590 \text{ kPa}, \quad E_C = 500 \text{ kPa}. \tag{3-2}$$

The outlet pressure of the simulation and the matched KdV models are provided in Figure 3-7.

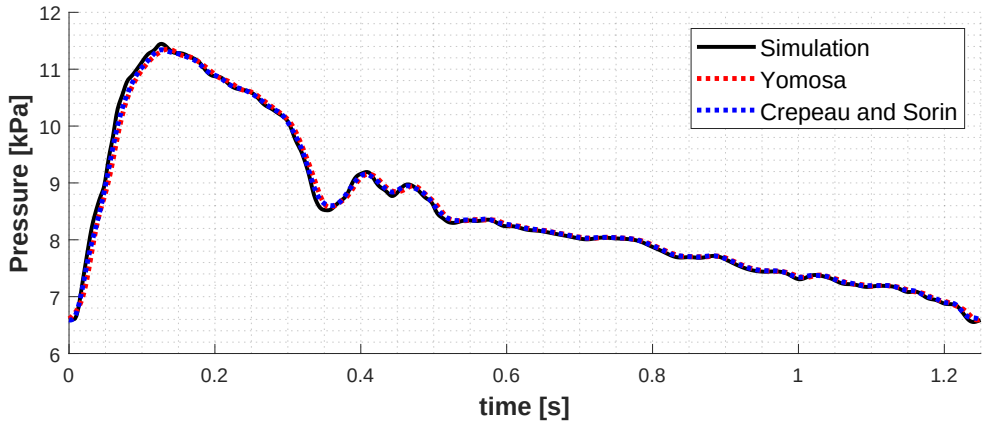

Figure 3-7: Short artery pressure output of the simulation and the matched KdV models ($\varepsilon_{\mathsf{Y}} = 0.0119,\ \varepsilon_{\mathsf{CS}} = 0.00714$).

The output of both matched KdV models are found to be in good agreement with the simulation output. However comparing the pressure at the inlet and the simulation pressure output (Figures 3-6 and 3-7 respectively), the inlet waveform is found to be well preserved at the outlet except a small time delay. As the artery is small in length, this is expected. Considering this, it is not possible to fully address whether the matched models are able to model the *nonlinear* phenomena of the pressure evolution in the arteries. In a way, the short artery test can only prove that the matched KdV models do no deviate too much from the reference behavior. The long artery test can provide us with more insight.

3-2-2 Long Artery Results

The measured and optimized parameters used for the matched models are

$$P_d = 6.550 \text{ kPa}, \quad E_C = 490 \text{ kPa}. \tag{3-3}$$

The outlet pressure of the simulation and the matched KdV models are provided in Figure 3-8.

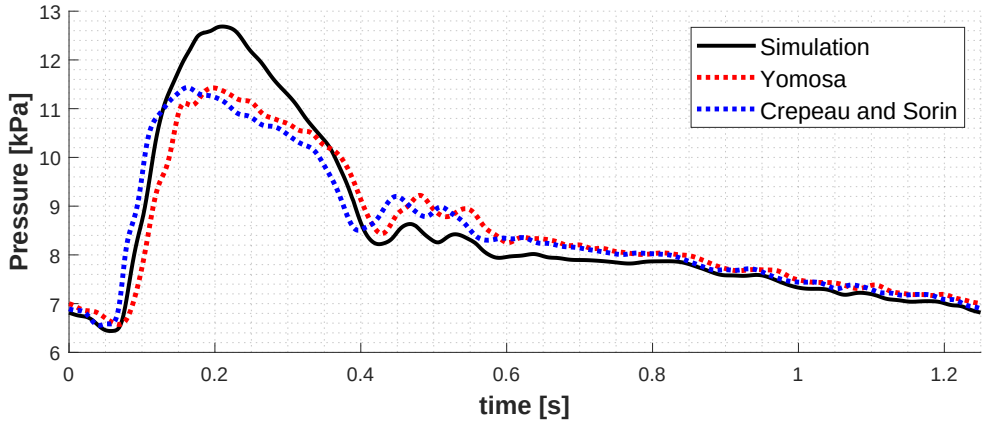

Figure 3-8: Long artery pressure output of the simulation and the matched KdV models ($\varepsilon_{\mathsf{Y}} = 0.0615,\ \varepsilon_{\mathsf{CS}} = 0.0629$).

The output of the both matched KdV models are found to differ from the simulation output, especially in the systolic part of the waveforms. In particular, we see a clear steepening behavior in the simulation output which is visible from the pressure increase in the systolic part compared to the pressure at the inlet taken as the simulation output in Figure 3-7. Steepening can be explained by the connection to other vessels, which is modeled using a 3-element Windkessel. To test this, we are neglecting the connection to the other vessels in the simulation by removing the Windkessel and using a reflection outlet type with zero reflection coefficient. The results are provided in Figure 3-9.

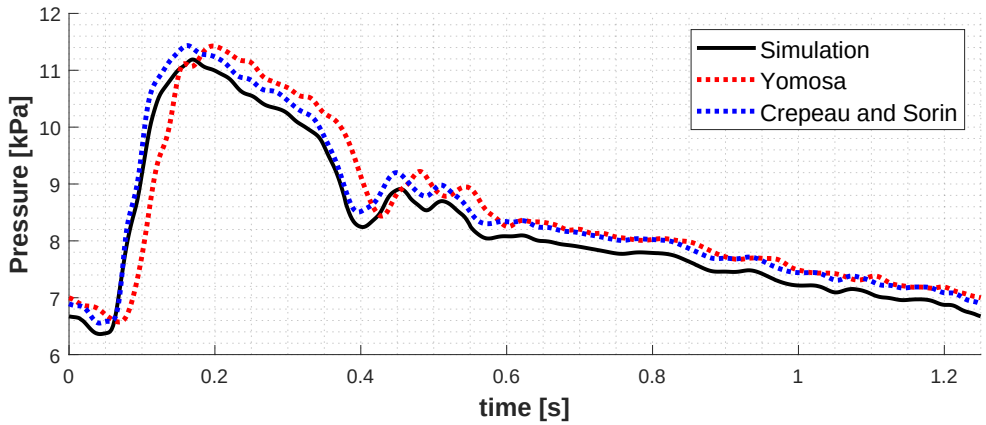

Figure 3-9: Long artery pressure output of the simulation and the matched KdV models. In the simulation, the reflection type outlet is chosen with $R_t = 0$ ($\varepsilon_{\mathsf{Y}} = 0.0579,\ \varepsilon_{\mathsf{CS}} = 0.0299$).

We see the removal of the steepening phenomena in the simulation output as a consequence. In fact, the simulation output is found to be smaller compared to the output of the matched models. The error between the matched models and the simulation output is found to decrease and the waveform shape of all outputs are found to be at a representative agreement level. The matched Yomosa output is found to be lagging compared to the matched Crépeau and Sorine output which seems to be in good agreement with the output in terms of phase. The difference between the simulation output and the matched models can be explained by frictional effects. Next, we also exclude the frictional effects in the simulation. The results are provided in Figure 3-10.

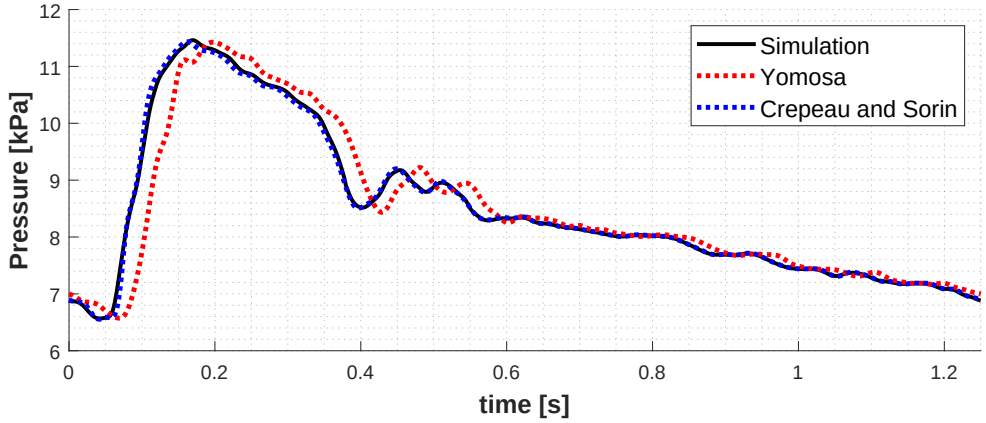

Figure 3-10: Long artery pressure output of the simulation and the matched KdV models. In the simulation, peripheral friction is neglected by setting $\mu = 0$ and the reflection type outlet is chosen with $R_t = 0$ ($\varepsilon_{\mathsf{Y}} = 0.0483,\ \varepsilon_{\mathsf{CS}} = 0.00648$).

With the additional exclusion of the peripheral friction, matched Crépeau and Sorine output is found to be almost identical with the simulation output. Although the shape of the matched Yomosa output waveform is in good agreement with the simulation output, it is found to be lagging by about 20-30 ms.

Based on the long artery tests, it was found out that in the long artery the matched KdV

models deviate from the simulation model when the connection to the other vessels is taken into account. In particular, the steepenin phenomena, which can be explained by a simple assignment of hydraulic impedance at the end of the vessel, can not be explained well based on the nonlinear superposition of solitons. We have also found out that the error between the simulation and both matched KdV outputs decrease significantly when the Windkessel is removed. The additional exclusion of frictional dynamics also reduce the error, making the matched KdV models reasonable approximations of the original system under the derivation assumptions. In all considered scenarios in this subsection, the error of the matched Crépeau and Sorine model is found to be less than the matched Yomosa model. An an important reminder, in Yomosa's original work [6] a spacelike KdV equation is derived and in our paper we converted it to timelike form based on Osborne and Petti [38] to derive the matched Yomosa model. This conversion is expected to increase the mismatch between the simulation and the matched Yomosa model so the conversion might be a causal or a contributing factor for the associated phase mismatch problem.

3-2-3 Branching Artery Results

The measured and optimized parameters used in the matched models are

$$P_d = 6.440 \text{ kPa}, \quad E_C = 633 \text{ kPa}. \tag{3-4}$$

The pressure of the simulation at the end of the abdominal aorta and the matched KdV models are provided in Figure 3-11.

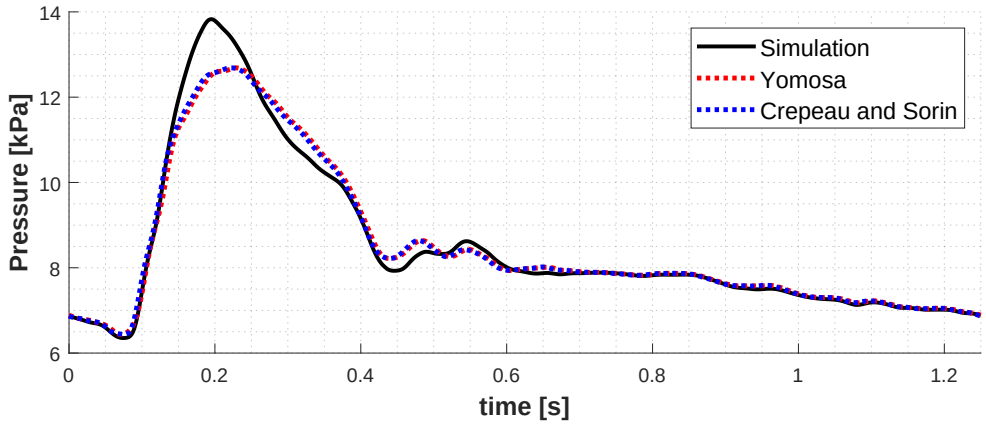

Figure 3-11: Branching artery pressure output of the simulation and the matched KdV models ($\varepsilon_{\mathsf{Y}} = 0.0381,\ \varepsilon_{\mathsf{CS}} = 0.0350$).

The output of the both matched KdV models are found to differ from the simulation output significantly, especially in the systolic part of the waveform. In particular, we see a clear steepening behavior in the simulation output which is visible from the pressure increase in the systolic part compared to the pressure at the inlet taken as the simulation output in Figure 3-8. As discussed in the previous case, the steepening can be explained by connection to the other vessels. To test this, we are neglecting the connection to the other vessels in the

simulation by removing the Windkessel and using a reflection outlet type with zero reflection coefficient. The results are provided in Figure 3-12.

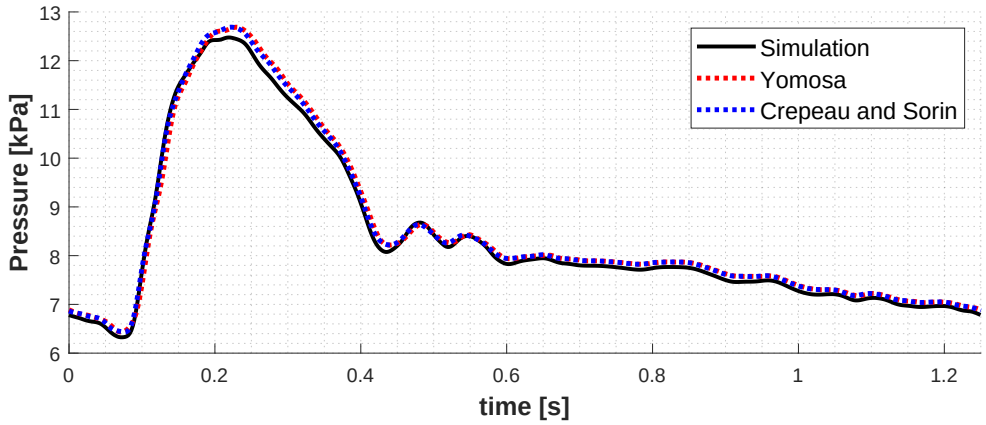

Figure 3-12: Branching artery pressure output of the simulation and the matched KdV models. In the simulation, the reflection type outlet is chosen with $R_t = 0$. ($\varepsilon_{\mathsf{Y}} = 0.0186,\ \varepsilon_{\mathsf{CS}} = 0.0140$).

Both matched models are found to be in good agreement with the simulation output after the removal of the Windkessel. However it should be mentioned that the removal of the Windkessel makes the reference output taken at the end of the abdominal aorta become independent of the bifurcation. In other words, the results in Figure 3-12 should be seen as the test of a medium length artery more than a branching artery. Like in the previous case, the exclusion of the friction leads to reduced error. The results are provided in Figure 3-13.

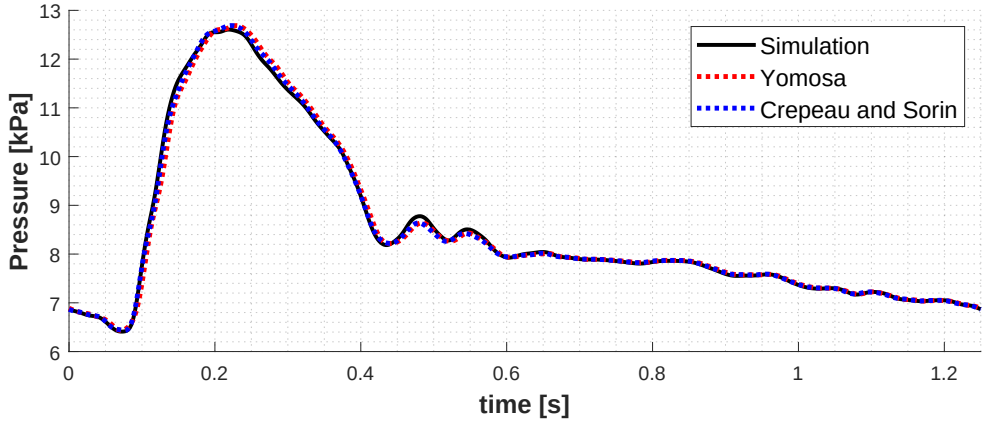

Figure 3-13: Branching artery pressure output of the simulation and the matched KdV models. In the simulation, peripheral friction is neglected by setting $\mu = 0$ and the reflection type outlet is chosen with $R_t = 0$ ($\varepsilon_{\mathsf{Y}} = 0.0137,\ \varepsilon_{\mathsf{CS}} = 0.00678$).

Like in the previous subsection, with the additional exclusion of the peripheral friction both matched models and the simulation output is found to be in good agreement. However the performance of the matched models in branching artery is not properly addressed so far as the first reference output is considered taken at the interconnection but not at the end of one of the identical branches. As the branches have different physical model parameters, to

test the performance of the matched models we need to use two KdV equations to compute the evolution of the inlet waveform. In particular, the matched KdV equations derived for the abdominal aorta is used to evolve the input from the proximal to the distal ends of the abdominal aorta, whereas the matched KdV equations derived for the iliac artery is used to evolve the pressure from the proximal to the distal end of the iliac artery.

$$E_C = 897 \text{ kPa}. \tag{3-5}$$

The outlet pressure of the simulation at the end of the iliac artery and the matched KdV models are provided in Figure 3-14.

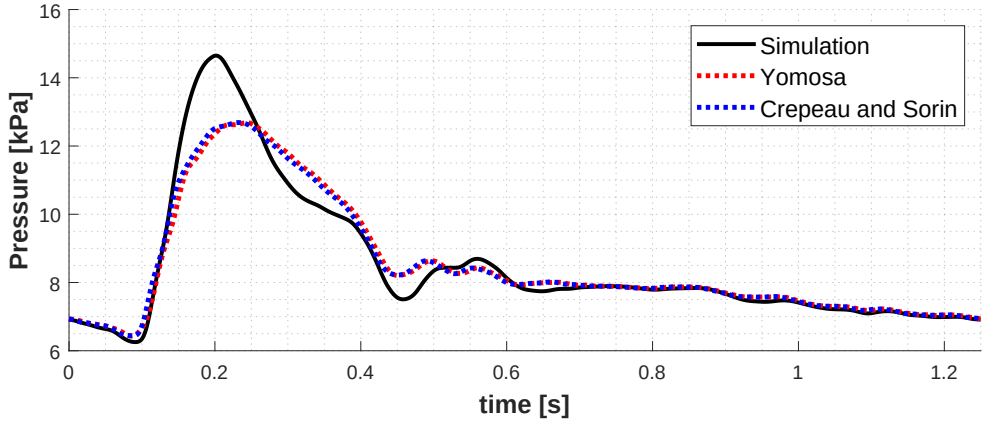

Figure 3-14: Branching artery pressure output of the simulation and the matched KdV models ($\varepsilon_{\mathsf{Y}} = 0.0693,\ \varepsilon_{\mathsf{CS}} = 0.0633$).

As it can be seen, the waveforms obtained from matched models are significantly different than the output waveform. Next, the Windkessel is removed to exclude the effects of connection of the iliac arteries to other arteries. The results are provided in Figure 3-15.

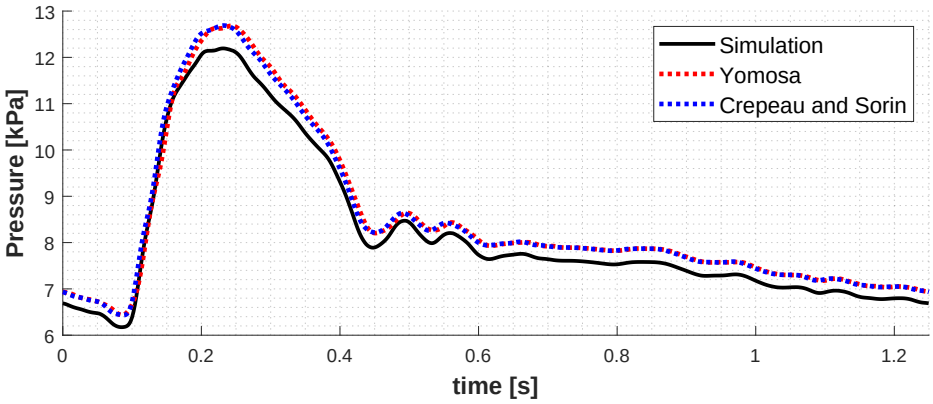

Figure 3-15: Branching artery pressure output of the simulation and the matched KdV models. In the simulation, the reflection type outlet is chosen with $R_t = 0$. ($\varepsilon_{\mathsf{Y}} = 0.0393,\ \varepsilon_{\mathsf{CS}} = 0.0367$).

The simulation output and the output of the matched models are in good agreement. As the Windkessel of both branches are removed, the effects of the other branch is also removed. In

other terms, the network becomes analogous to a serial connection of two arteries. Next, we remove the effects of friction. The results are provided in Figure 3-16.

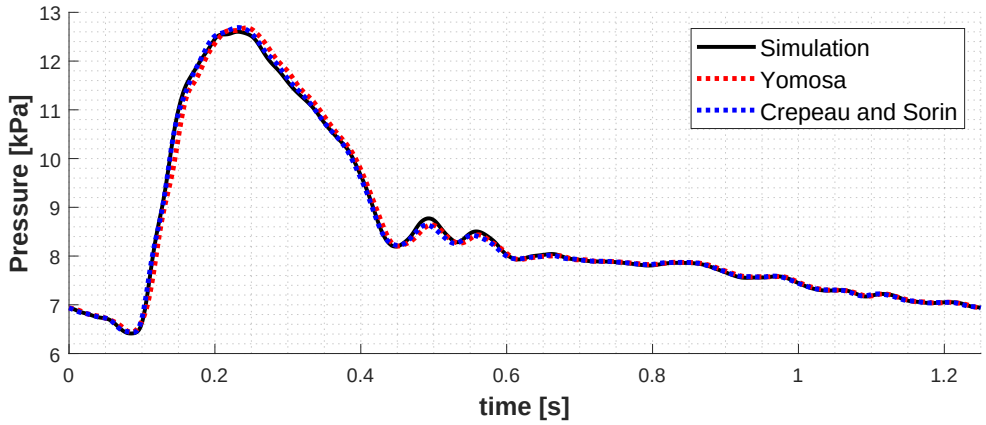

Figure 3-16: Branching artery pressure output of the simulation and the matched KdV models. In the simulation, peripheral friction is neglected by setting $\mu = 0$ and the reflection type outlet is chosen with $R_t = 0$ ($\varepsilon_{\mathsf{Y}} = 0.0142,\ \varepsilon_{\mathsf{CS}} = 0.00524$).

The simulation and the matched models' outputs almost become identical.

Based on the results for the branching artery, it was found that the connection to other arteries is not captured well by the matched models, similar to the results obtained in the long artery tests. The mismatch of the arterial blood pressure waveforms are especially visible in the second reference output, at the distal end of one of the branches. In the branching artery test, with the removal of the Windkessels, the matched KdV models outputs were found to be in good agreement at both reference points. The frictional effects are more visible at the second reference which can be explained by the longer space evolution. Similar to the results obtained in the long artery tests, the effects of the friction in the absence of the Windkessel is represented like a negative offset in the simulation output. In the branching artery test, we also used two matched KdV models back to back to evolve the inlet pressure till the distal end of one of the branches. The output was estimated accurately by the matched models in the absence of the Windkessel.

3-3 Testing of the Matched 1-Soliton Solutions

In this section the matched 1-soliton solutions provided in Equations 2-86 and 2-97 will be tested, corresponding to the matched Yomosa and the matched Crépeau and Sorine 1-soliton solution respectively. In a KdV-type medium, the associated 1-soliton solution is expected to propagate with constant velocity while maintaining its shape exactly. Based on this, if the derived KdV-type dynamics from the 1-D Navier-Stokes equations is a proper representation, we expect only phase difference at the simulation output when 1-soliton solution is provided as input. The flowchart describing the test is provided in Figure 3-17.

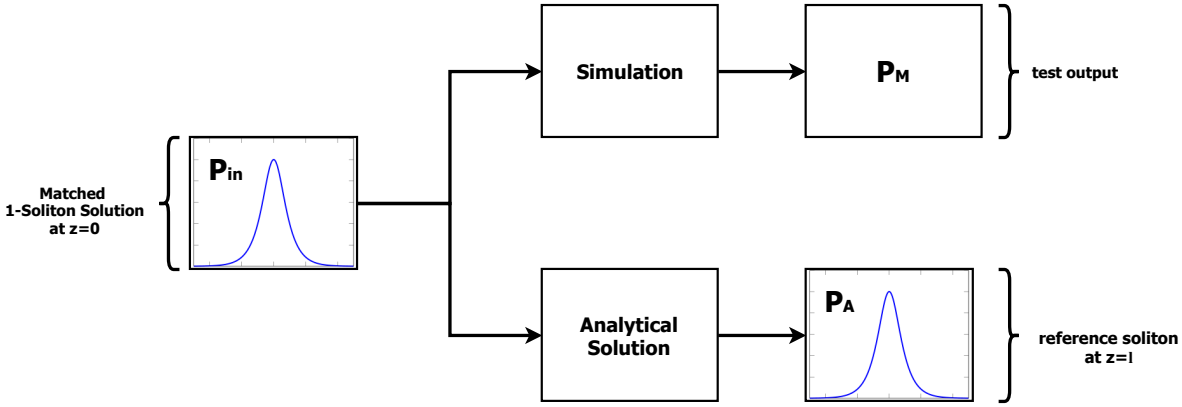

Figure 3-17: The testing of 1-soliton solution in each case study.

This test can be seen as an indirect verification method for the underlying KdV-type dynamics. Using the scattering transform of Gardner et al. [45], a discrete and a continuous spectrum can be acquired from the initial data governed by KdV type dynamics. The discrete spectrum is considered to represent finite number of solitons in the solution (N-solitons), whereas the continuous spectrum is considered to represent the reflections in transmissions. Therefore under the assumption that the arterial blood dynamics can be represented accurately by KdV type dynamics, we expect solitons in the arterial blood pressure waveform. As we are using a 1-soliton inlet over a realistic inlet, the continuous spectrum of the initial data is considered to be removed which can provide us insight on the integrity of discrete spectrum that can be obtained with the scattering transform.

As a reminder, the matched KdV models based on Yomosa [6] and Crépeau and Sorine [9] depend on the use of asymptotic methods. As it is the general case for asymptotic methods, the behavior is estimated accurately within a certain range. In particular, for both model derivations long wave estimation is used to scale the time and the position variables based on the length scales of a small amplitude KdV soliton as described in Appendix D. This potentially poses a fundamental problem in the soliton interpretation of arterial blood pressure waveforms. For a proper interpretation, we need the soliton contribution in the initial data to represent the waveform, which requires the solitons considered in the solution to have significantly high amplitudes. On the other hand, we expect the estimated KdV type dynamics to hold less for solitons with high amplitudes. Therefore 1-soliton test can also help us identify the amplitude range when the KdV type dynamics hold. The amplitude, the group velocity and the width of a soliton is scaled by the imaginary wavenumber, κ, which exists as a free variable in the considered solitons. Therefore the matched 1-soliton solutions will be tested

within a range of κ. As the scaling also depends on the physical model parameters and the coefficients of the matched KdV equations, the range for κ has to be adapted for each case and between models.

In the simulation, the connection to other vessels and the peripheral friction will be included, as the clinical measurements are subject to the same effects. Same P_d and E_C values used in the previous section in the case studies. The analytical solution, P_A, can be calculated easily using

$$P_A = P_s(l, t), \tag{3-6}$$

where P_s is the considered matched 1-soliton solution also used to calculate the pressure at the inlet, P_in, such that

$$P_{\text{ini}} = P_s(0, t). \tag{3-7}$$

As the analytical solution is considered to be the reference behavior, the normalized error, ϵ, is defined as

$$\epsilon = \frac{||P_M - P_A||_2}{||P_A||_2}. \tag{3-8}$$

In Case III tests, only the first reference output at the end distal of the abdominal aorta is considered. This is based on the fact that the 1-soliton solution for the abdominal aorta is not a 1-soliton solution to the iliac arteries. This is explained by the dependence of the matched KdV coefficients on physical model parameters.

3-3-1 Matched Yomosa Solution Results

Equation 2-86 is used to derive the inlet boundary conditions and the analytical solution. As an important remark, the matched 1-soliton solution is associated to the original spacelike equation derived by Yomosa [6], so the estimation errors caused by conversion to timelike form is not relevant. The normalized error is plotted for a range of κ in Figure 3-18.

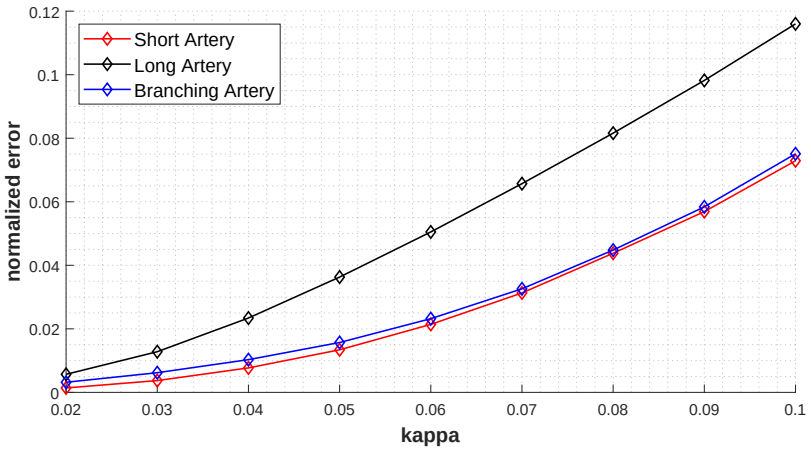

Figure 3-18: The plot of ϵ versus κ for the matched Yomosa solution.

The upper range of κ was chosen in such a way that the amplitude of the soliton at the inlet is between 6 to 8 kPa. The lower range of κ was chosen in such a way that the amplitude of the soliton at the inlet is between 200 to 400 Pa. The amplitude of the soliton, A_Y, can be easily derived from Equation 2-86:

$$A_Y = \frac{6p_0}{L}\kappa^2. \tag{3-9}$$

The normalized error is plotted against A_Y in Figure 3-19.

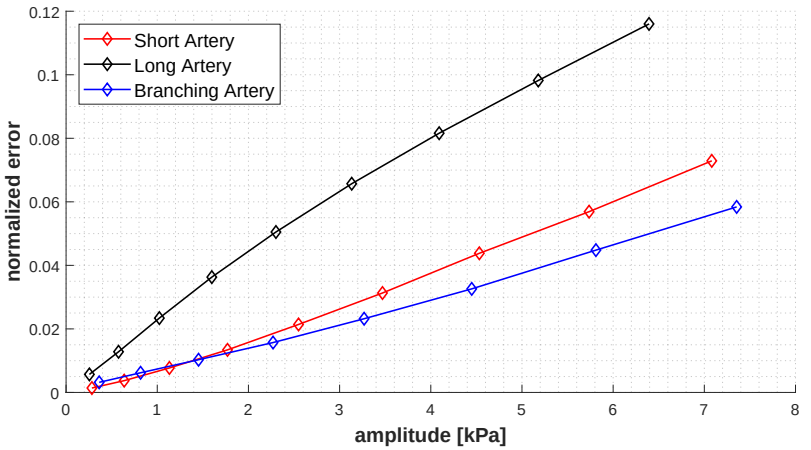

Figure 3-19: The plot of ϵ versus A_Y for the matched Yomosa solution.

Based on Figures 3-18 and 3-19, the normalized error is an increasing function of κ and A_Y. This is as expected due to long wave estimation. Although ϵ provides a measure of the match between the analytical solution and the simulation output, it is also important to study the time behavior. These differences are expected to be more visible in the long artery test as ϵ is higer at the same A_Y compared to the other cases. The analytical solution and the simulation output for high amplitude soliton in long artery test is provided in Figure 3-20.

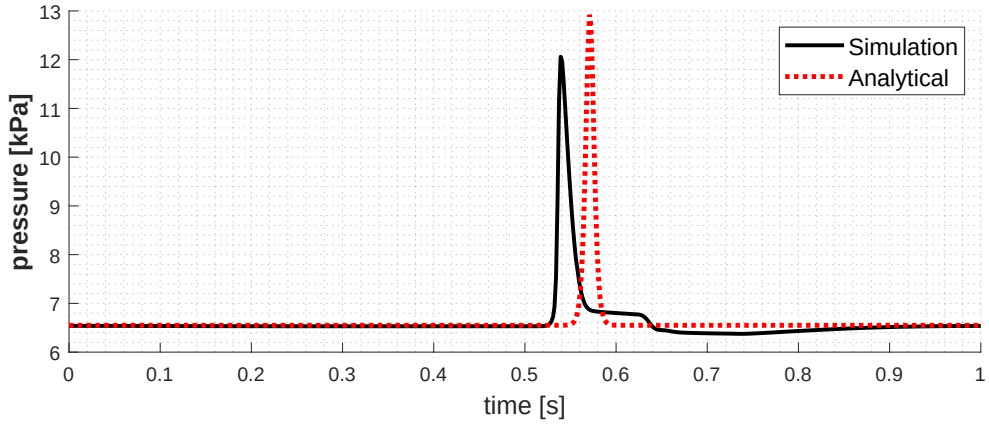

Figure 3-20: The comparison of the analytical solution and the simulation output in Case II ($\kappa = 0.1$).

Based on the plot, we see that the analytical solution is lagging. Furthermore the simulation output's peak pressure is less compared to the analytical solution and there is a visible deviation from soliton's characteristic sech-squared profile. The analytical solution and the simulation output for a lower amplitude soliton is provided in Figure 3-21.

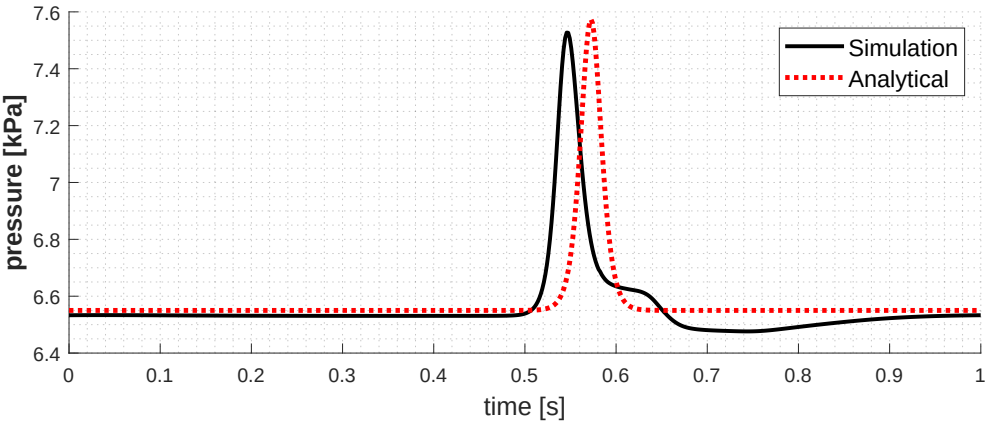

Figure 3-21: The comparison of the analytical solution and the simulation output in Case II ($\kappa = 0.04$).

We see similar results in a smaller pressure scale compared to high amplitude soliton results. However in comparison, the decrease of peak pressure and the phase difference is less noticeable.

3-3-2 Matched Crépeau and Sorine Solution Results

Equation 2-97 is used to derive the inlet boundary conditions and the analytical solution. As the solution is associated to a timelike KdV equation, the scaling κ range is different from the tests done in the previous subsection. The normalized error is plotted for a range of κ in Figure 3-22.

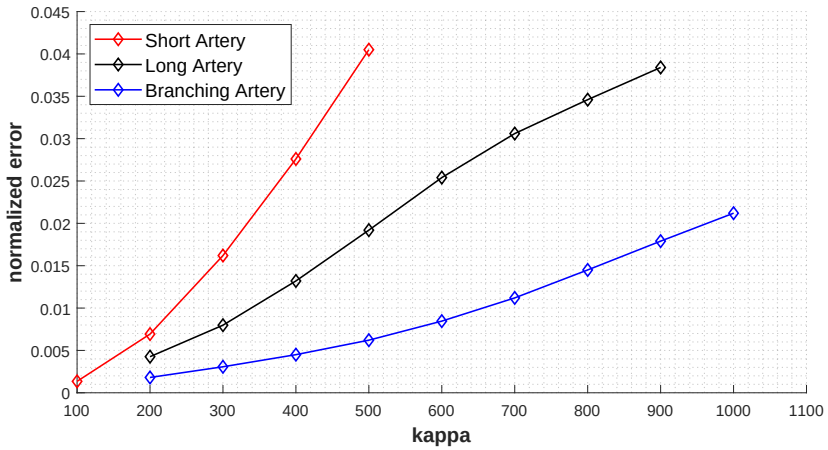

Figure 3-22: The testing of 1-soliton solution in each case study.

The upper range of κ was chosen in such a way that the amplitude of the soliton at the inlet is between 6 to 8 kPa. The lower range of κ was chosen in such a way that the amplitude of the soliton at the inlet is between 200 to 400 Pa. The amplitude of the soliton, A_{CS}, can be easily derived from Equation 2-97:

$$A_{CS} = \frac{3\rho c_0 d_2}{A_0 d_1}\kappa^2. \tag{3-10}$$

The normalized error is plotted against A_{CS} in Figure 3-23.

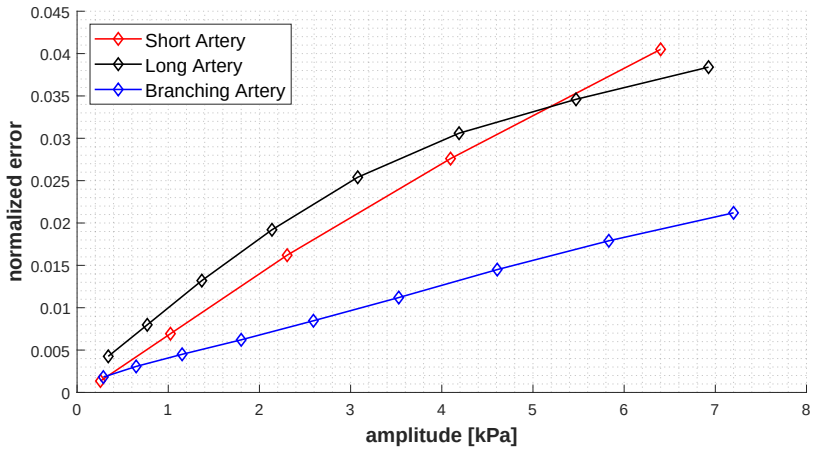

Figure 3-23: The plot of ϵ versus A_{CS} for the matched Crépeau and Sorine solution.

Based on Figures 3-22 and 3-23, the normalized error is an increasing function of κ and A_Y. This is as expected due to long wave estimation. As an important remark, the tested input solitons were found to be very steep in nature, which is expected to cause numerical errors in the simulation output as the provided time steps lead to misrepresentative discretization of the input in the tested high κ range. The steepness of the matched Crépeau and Sorine solutions are explained by the high nonlinear term scaling and low dispersion term scaling in the derived KdV equations. This problem could be solved by increasing the time steps in the simulation file but this was found to cause stability problems. As the steepest soliton solutions are tested in Case 2, this explains the difference of the error profile compared to other cases in the high κ range. Although ϵ provides a simplified measure of the match between the analytical solution and the simulation output, it is also important to study the time behavior. These differences are expected to be more visible in the long artery test but short artery test will be considered to study time behavior for high κ instead due to the described discretization problem. The analytical solution and the simulation output for high amplitude soliton in the short artery test is provided in Figure 3-24.

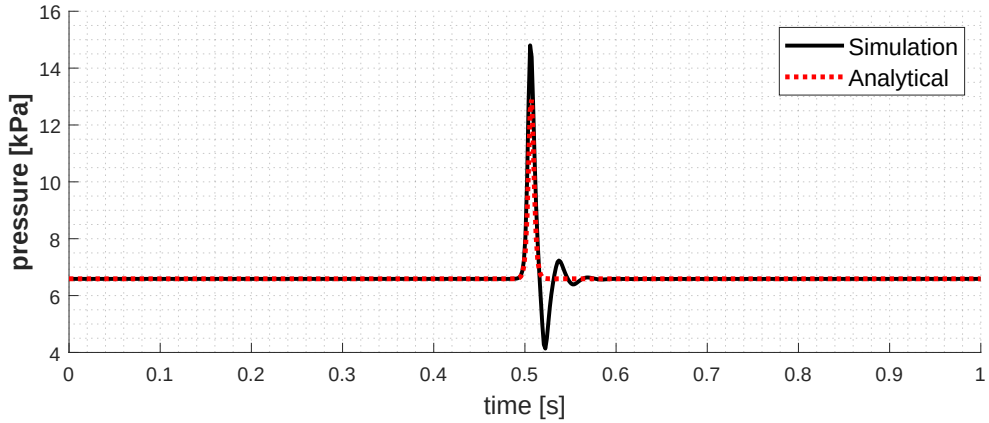

Figure 3-24: The comparison of the analytical solution and the simulation output in Case I ($\kappa = 500$).

Based on the plot, the simulation output's peak pressure is less compared to the analytical solution and there is a visible deviation from soliton's characteristic sech-squared profile. In fact the simulation output looks oscillatory, much like the response of an underdamped system. The analytical solution and the simulation output for a lower amplitude soliton in short artery test is provided in Figure 3-25.

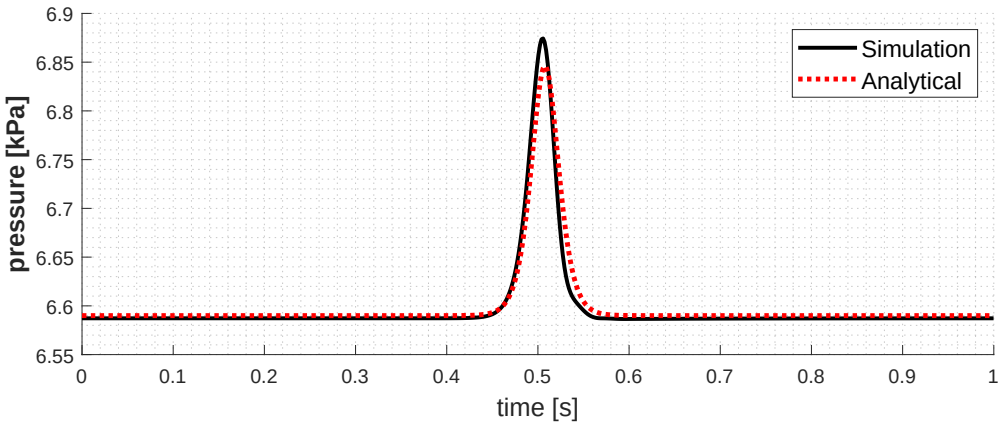

Figure 3-25: The comparison of the analytical solution and the simulation output in Case I ($\kappa = 100$).

The analytical solution and the simulation output are found to be in good agreement. To compare matched Crépeau and Sorine 1-soliton solution with matched Yomosa 1-soliton solution, the low amplitude soliton in long artery test is provided in Figure 3-26.

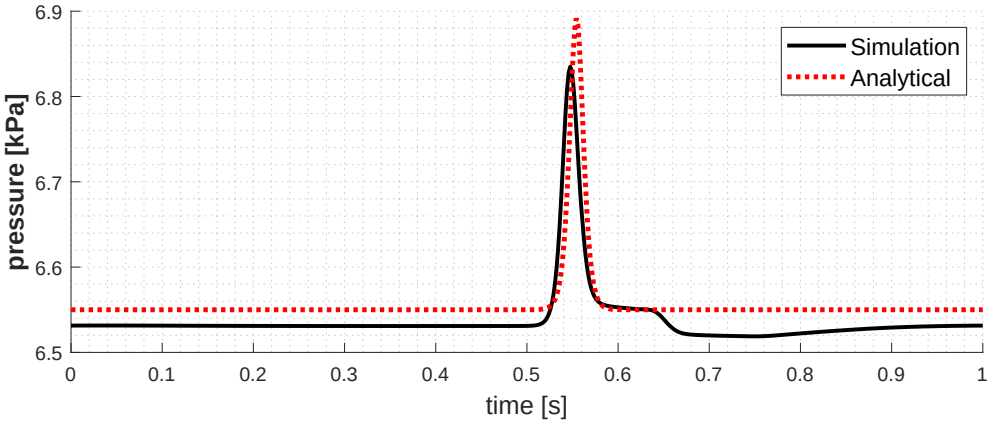

Figure 3-26: The comparison of the analytical solution and the simulation output in Case II ($\kappa = 200$).

The simulation output's waveform is found to be similar compared to the results obtained in the previous section (Figure 3-21). However unlike the results obtained for matched Yomosa solution, the phase difference between the analytical solution and the simulation is found to be minimal. As a reminder, matched Crépeau and Sorine model was also found to outperform matched Yomosa model in terms of phase estimation, when the realistic input were evolved based on the matched timelike KdV models (Figures 3-8, 3-9 and 3-10).

3-4 Nonlinear Fourier Analysis of Arterial Blood Pressure Waveform

In this test, the discrete spectrum of pressure at the inlet and at the outlet will be computed using the scattering transform proposed by Gardner et al. [45]. Unfamiliar readers can find more information on scattering transform in Appendix C. The matched Yomosa and the matched Crépeau and Sorine model will be used to derive the corresponding scattering problem parameter. Chebfun will be used for the computation of the spectrum. The discrete spectrum of the input and the output will be compared and discussed. The flowchart of this test is provided in Figure 3-27.

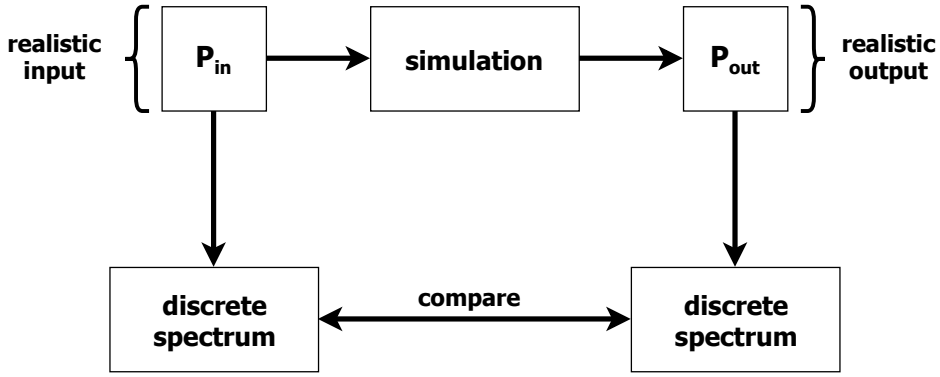

Figure 3-27: The task description in each case study.

The scattering transform is analogous to a nonlinear generalization of Fourier transform. In the literature, the study of system behavior from such spectra is referred to as Nonlinear Fourier Analysis which is explained in detail in Osborne [46].

Consider the following timelike KdV equation:

$$\hat{P} + C_1 \frac{\partial \hat{P}}{\partial t} + C_2 \hat{P} \frac{\partial \hat{P}}{\partial t} + C_3 \frac{\partial^3 \hat{P}}{\partial t^3} = 0. \tag{3-11}$$

Soliton solutions to Equation 3-11 propagate in space and considered to be fixed in the frame $\xi = t - C_1 z - C_3 \kappa^2 z$, where κ is the imaginary wavenumber. The group velocity, v, of the solitons then can be calculated based on ξ:

$$v(\kappa) = \frac{1}{C_1 + C_3 \kappa^2}. \tag{3-12}$$

Based on Gardner [45], the associated Schroedinger eigenvalue problem is

$$\frac{\partial^2 \Psi}{\partial t^2} + \lambda \hat{P}(z_0, t)\Psi + \kappa^2 \Psi = 0, \tag{3-13}$$

where $\Psi = \Psi(t)$ are the eigenfunctions associated with κ^2 eigenvalues and λ is a measure of nonlinearity to dispersion given by

$$\lambda = \frac{C_1}{6C_2}. \tag{3-14}$$

As we will use Chebfun for the calculation of spectrum, the definition used for the scattering problem by Chebfun has to be considered as well. In particular, the *quantumstates* function will be used in Chebfun and based on the documentation the Schroedinger eigenvalue problem defined as

$$h^2\frac{\partial^2\Psi}{\partial t^2} - V(z_0,t)\Psi + \tilde{\kappa}^2\Psi = 0, \tag{3-15}$$

where h is considered to be the parameter instead of λ. Equation 3-13 can be transformed into 3-15 by using the following transformations:

$$h = \left(\frac{1}{\lambda}\right)^{\frac{1}{2}}, \quad \tilde{\kappa} = h\kappa, \quad V(z_0,t) = -\hat{P}(z_0,t). \tag{3-16}$$

The coefficients of the matched Yomosa model (2-91) and the matched Crépeau and Sorine model (Equation 2-99) can be substituted into Equation 3-11 to calculate h. Additionally the initial data has to be reversed in sign and the scaling of the output wavenumbers should be considered in the spectrum calculations.

The number of negative eigenvalues included in the solution, N, will be finite, leading to N imaginary wavenumbers $\tilde{\kappa}_n$ and corresponding eigenfunctions Ψ_n. The calculated Ψ_n are normalized wavefunctions so that

$$\int_{-\infty}^{\infty} ||\Psi_n||_2 \, dt = 1, \quad \forall n \in \{1,...,N\}. \tag{3-17}$$

Ψ_n can be denormalized to original unit scaling using $\tilde{\kappa_n}$ [47]

$$\psi_n = 4h\tilde{\kappa_n}\Psi_n^2, \tag{3-18}$$

where ψ_n is the denormalized wavefunction.

If the continuous spectrum is neglected, the initial data can be reconstructed using the denormalized wavefunctions:

$$V(z_0,t) \simeq V_e(t) = \sum_{n=1}^{N} \psi_n, \tag{3-19}$$

where V_e is the estimate signal from the discrete spectrum. Based on Yomosa [6] and Crépeau and Sorine [9] 2 or 3 solitons can be used represent arterial blood pressure waveform. Based on this hypothesis, in the case our calculations result with the calculation of more discrete components ($N > 3$), we will use the first 3 ψ_n to calculate V_e. As an important remark, the first 3 ψ_n correspond to the highest 3 $\tilde{\kappa}_n$ based on the calculation of the discrete spectrum so

the most significant contributions will be included in the truncated estimates. The normalized error between the arterial blood pressure waveform, P_{ABP}, and V_e is calculated as

$$\epsilon = \frac{||P_{\text{ABP}} - V_e||_2}{||P_{\text{ABP}}||_2}. \tag{3-20}$$

3-4-1 Short Artery Results

First h_Y is calculated based on matched Yomosa model:

$$h_Y = 4.30. \tag{3-21}$$

Using the calculated h_Y, we get 3 imaginary wavefunctions both for the input and the output. The denormalized wavefunctions and the arterial blood pressure waveform is provided in Figure 3-28.

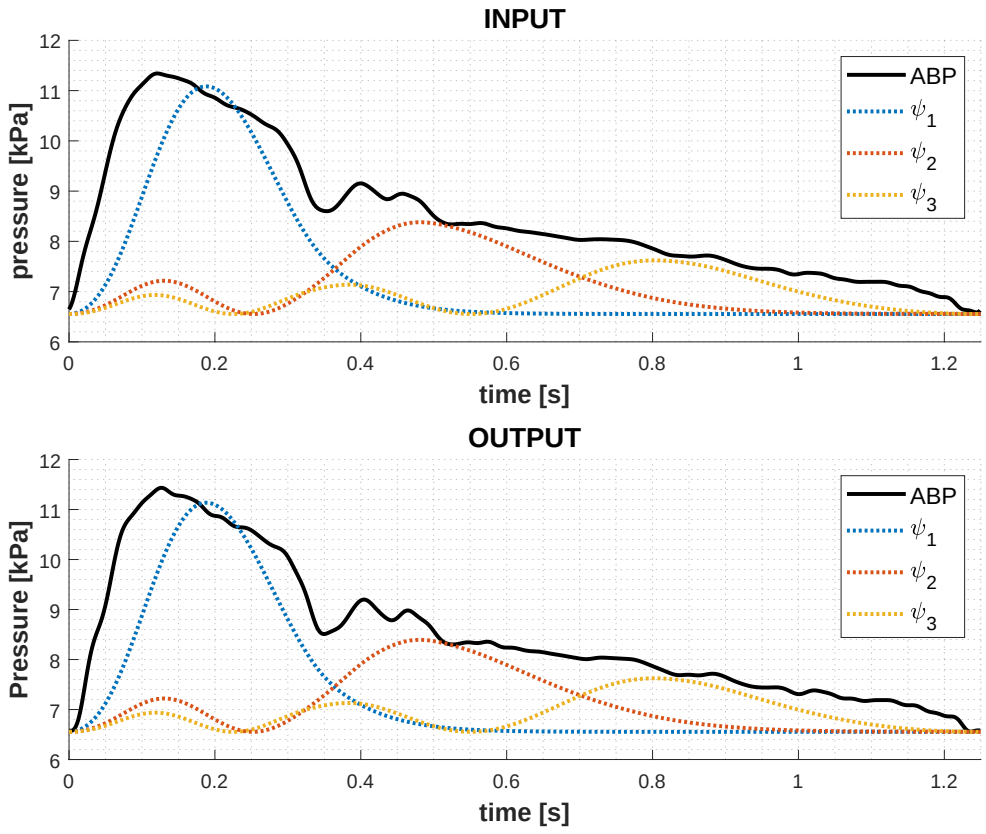

Figure 3-28: Calculated denormalized wavefunctions using matched Yomosa model for Case I.

Imaginary $\tilde{\kappa}$ values of the calculated input spectrum are given as

$$\tilde{\kappa} \in \{56.5,\ 39.0,\ 27.5\}, \tag{3-22}$$

which correspond to solitons moving with group velocities between 4.32 and 4.33 ms^{-1}. Imaginary $\tilde{\kappa}$ values of the calculated output spectrum are given as

$$\tilde{\kappa} \in \{56.8,\ 39.0,\ 27.5\}, \tag{3-23}$$

which also correspond to solitons moving with group velocities between 4.32 and 4.33 ms^{-1}. Plot of the calculated κ spectrum is provided in Figure 3-29.

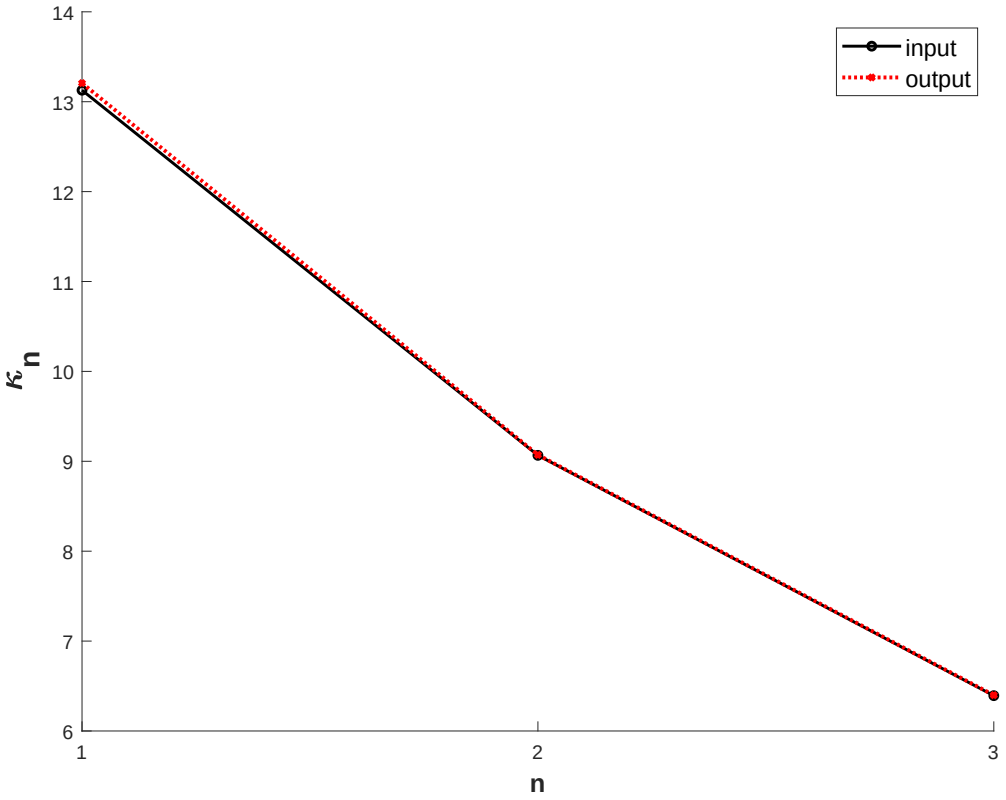

Figure 3-29: Plot of κ_n using matched Yomosa model for Case I.

The wavenumbers describing the discrete input and output spectra are found to be in good agreement. The group velocities of the solitons associated to the solutions were found to be in a narrow range. This can be explained by high C_1 to C_3 ratio in Equation 3-12.

As a reminder, based on previous verification tests for the short artery (Figure 3-7), we expect negligible change in the output waveform and a small time shift so the spectrum match of the input and the output can be specific to this case. Next, we calculate V_e by summing all ψ_n which is provided in Figure 3-30.

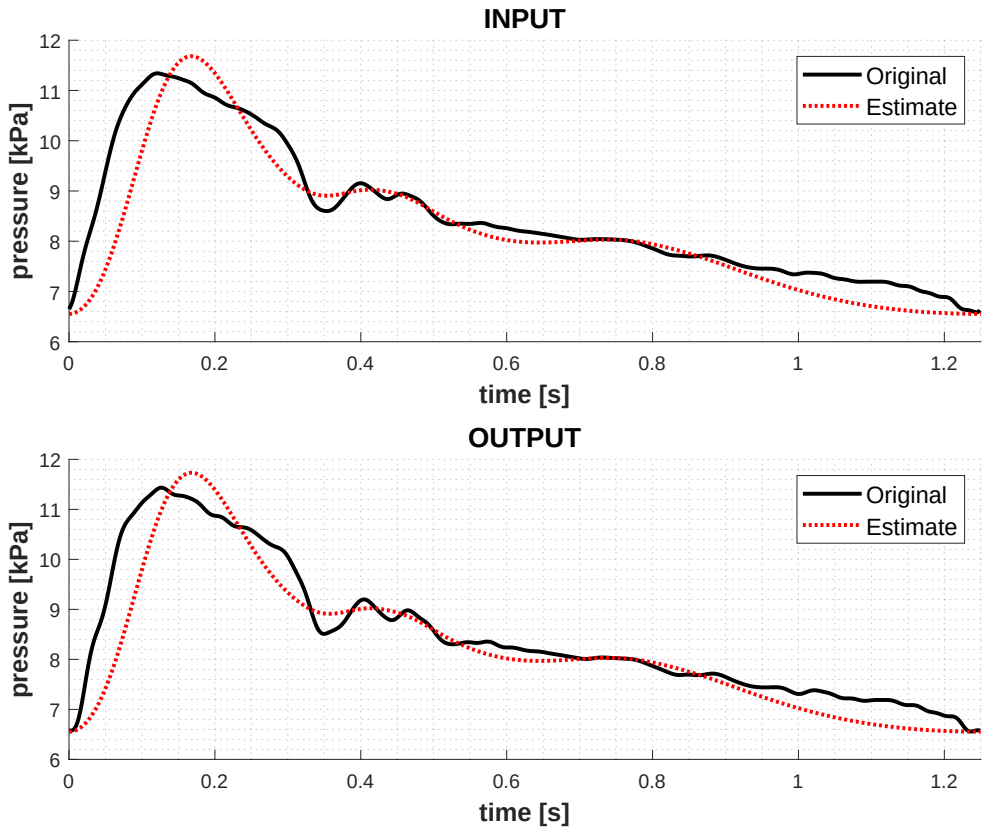

Figure 3-30: The estimate of ABP waveform from the discrete spectrum using matched Yomosa model for Case I.

The normalized errors associated to the estimates are calculated as

$$\epsilon_{\text{in}} = 0.237, \quad \epsilon_{\text{out}} = 0.229. \tag{3-24}$$

Based on Figure 3-30, the reconstruction of the waveform based on the matched Yomosa model results with a simplified waveform that captures the main variations in the original waveform. However the minor variations of the original waveform are not captured well in the reconstructed signal.

Considering the soliton interpretation of the arterial blood pressure waveform and referring to Figure 3-28, ψ_1 is considered to represent the systolic phenomena in which the wave group velocity and amplitude is the highest. ψ_3 is considered to represent the diastolic phenomena in which the wave group velocity and the amplitude is lowest. ψ_2 can be associated to an intermediate wave which seems to be dominant following the closing of the aortic valve.

Next h_{CS} is calculated based on matched Crépeau and Sorine model:

$$h_{CS} = 0.226. \tag{3-25}$$

Using the calculated h_{CS}, we get 71 imaginary wavefunctions both for the input and the output. This is explained by the smallness of h_{CS} as N included in the solution is a decreasing function of h used for analysis. However the results contradict with Crépeau and Sorine and coworkers' results [9, 11] as 3 solitons chosen from such spectrum is not expected to represent the waveform well. The first three denormalized wavefunctions and the arterial blood pressure waveform are provided in Figure 3-31.

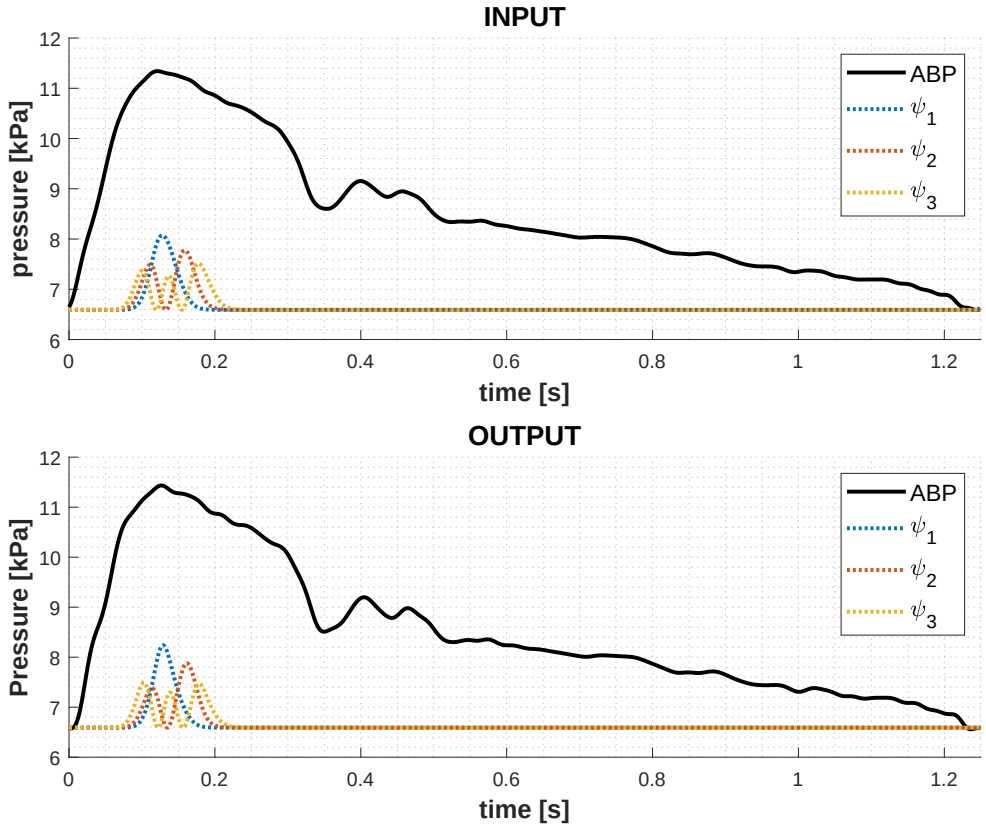

Figure 3-31: Calculated first 3 denormalized wavefunctions using matched Crépeau and Sorine model for Case I.

Considering the fact that the first three wavefunctions belong to the highest amplitude and group velocity solitons, the rest of the denormalized wavefunctions will have even smaller contribution. Next, we calculate V_e by summing the first 3 ψ_n which is provided in Figure 3-32.

The normalized errors associated to the estimates are calculated as

$$\epsilon_{\text{in}} = 0.892, \quad \epsilon_{\text{out}} = 0.891. \tag{3-26}$$

The estimates do not represent the original waveform. The results indicate that matched Crépeau and Sorine model rather explains a soliton interpretation of the arterial blood pressure waveform corresponding to the transmission of many small amplitude solitons. Referring

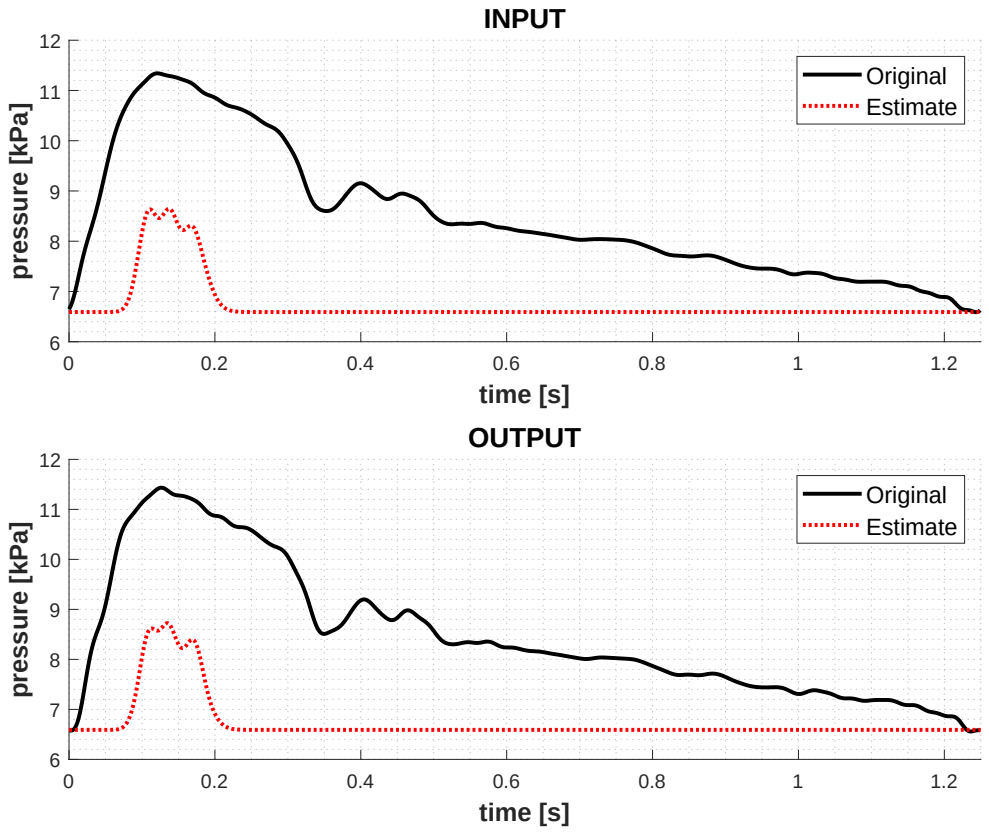

Figure 3-32: The estimate of ABP waveform from the discrete spectrum using matched Crépeau and Sorine model for Case I using the first 3 denormalized wavefunctions.

back to the previous results, the 1-soliton solutions to matched Crépeau and Sorine model were found to be too steep, which in a way requires many solitons in the solution to represent the entire waveform. As an example, in Figure 3-33 all 71 denormalized wavefunctions are used for the estimation of V_e.

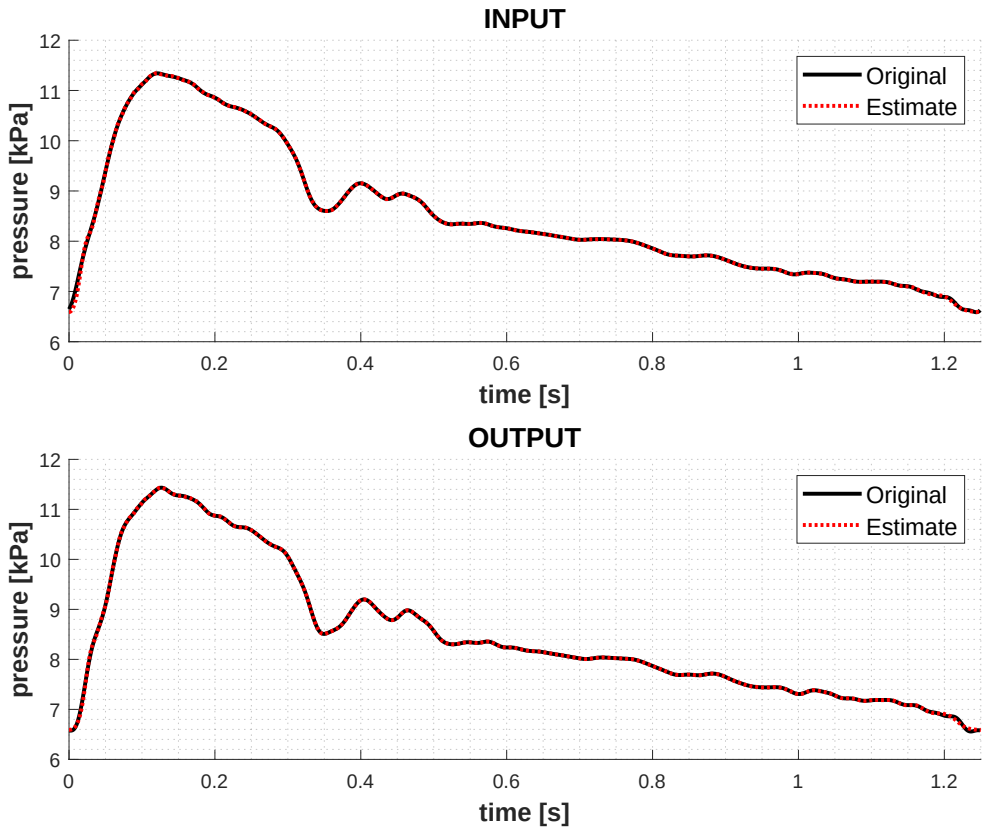

Figure 3-33: The estimate of ABP waveform from the discrete spectrum based on matched Crépeau and Sorine model for Case I using all 71 denormalized wavefunctions.

The normalized errors associated to the estimates are calculated as

$$\epsilon_{\text{in}} = 0.00458, \quad \epsilon_{\text{out}} = 0.00876. \tag{3-27}$$

The estimate and the original signal seem to be identical but this can alternatively be seen as an overfitting problem. The estimate error between the reconstructed signal from the discrete spectrum and the original signal, is a decreasing function of h. As a consequence, if h is chosen smaller than what it should be based on the physics of the medium, the continuous solution would be forced to become negligible and the scattering data would be representing unphysical phenomena. The process can be seen analogous to modeling a signal using sech-squared functions - as long as we include enough of them in the solution, the estimation error will vanish.

Plot of the calculated κ spectrum is provided in Figure 3-34.

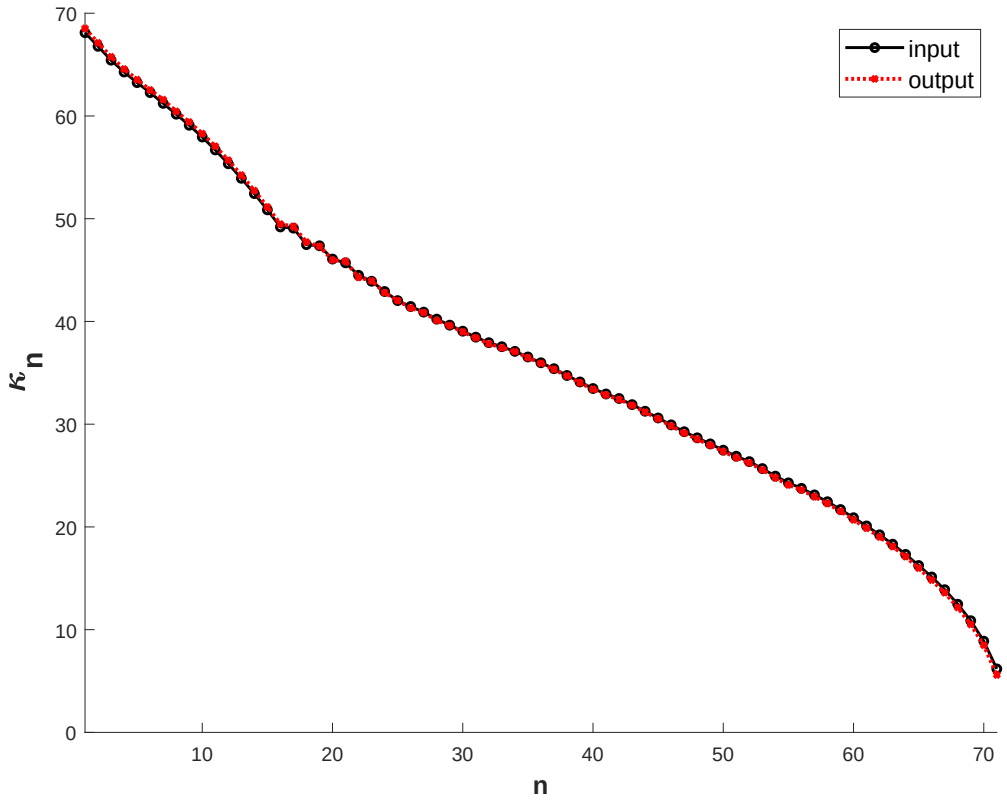

Figure 3-34: Plot of κ_n of matched Crépeau and Sorine model for Case I.

The input and the output spectrum are found to be in good agreement. Soliton solutions associated to the input and the output were found to have group velocities between 5.15 to 5.38 m^{-1}. Based on Figure 3-34, we see change of profile after $n = 16$. Following this intuition, the fastest 16 solitons are grouped together to estimate a systolic component which is given in Figure 3-35.

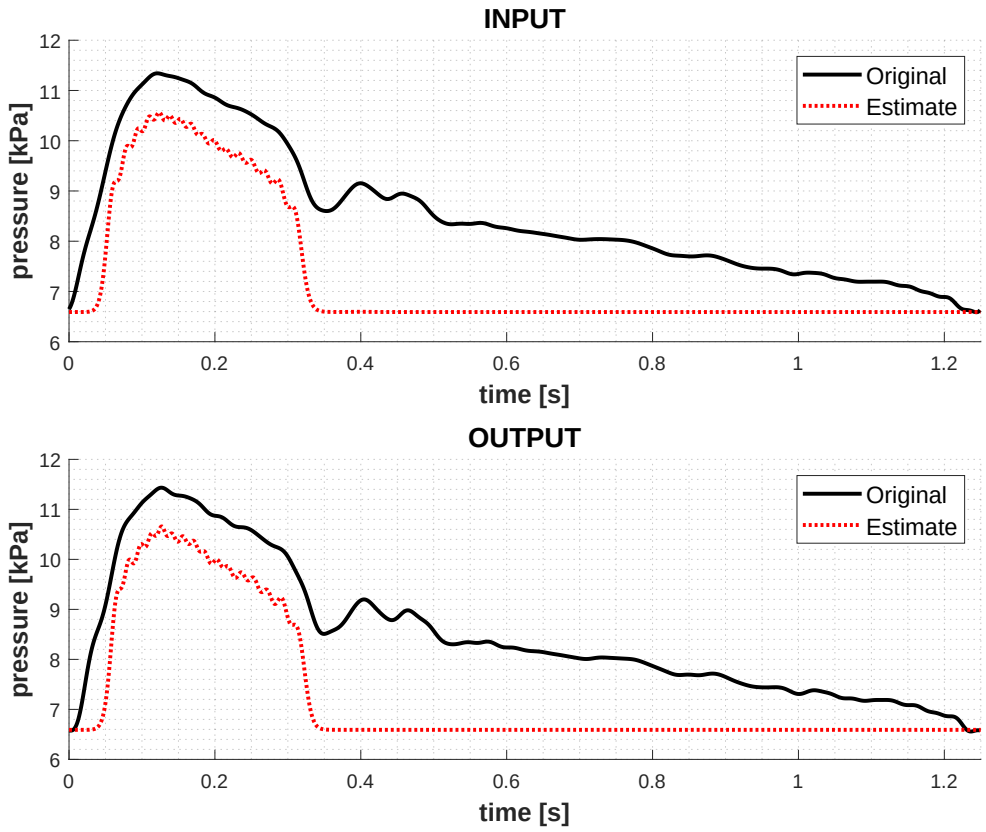

Figure 3-35: The systolic estimate of ABP waveform from the discrete spectrum based on matched Crépeau and Sorine model for Case I using the first 16 denormalized wavefunctions.

As it can be seen from the systolic estimate, all the considered wavefunctions are dominant only in the systolic part of the original waveform. The systolic estimate can be used to estimate the cardiac output with a systolic area method. Studying the accuracy and the robustness of such an algorithm would require future work as simultaneous clinical measurements of both pressure and flow would be needed for a proper benchmark test.

As a side remark, a similar approach is followed to reconstruct a systolic estimate in Laleg-Kirati et al. [14] based on grouping the fastest solitons in the spectrum; in this work the estimate is used to determine *end-systole* which marks the time instant between the systolic and the diastolic part of the pressure waveforms. The determination of the end-systole is non-trivial in original waveforms and usually one third of the cardiac cycle or the position of the dicrotic notch is taken as an estimate. For the unfamiliar readers, the dicrotic notch is generally considered as the local minimum that follows the systolic component. However based on the pressure waveform measurements, the notch might correspond to a saddle point or it might be visually hidden in either systolic or the diastolic part of the waveform. Accurate determination of the end-sytole can be useful for the pulse contour methods which depend on this parameter. In particular, the area under the pressure waveform from the initial time to the end systole is assumed to correlate with cardiac output by some systolic area methods. However the dependency on this correlation assumption pose a more fundamental inaccuracy problem for the pulse contour methods - potentially a more accurate estimate of

the end-systole might work as good as a rough estimate in terms of global flow estimation.

Major differences were found between matched Yomosa and Crépeau and Sorine models in the discrete spectrum analysis. Nonlinear Fourier analysis based on Matched Yomosa model returned 3 high amplitude solitons propagating relatively with similar group velocities, specifically between 4.32 and 4.33 ms^{-1}. Nonlinear Fourier analysis based on Matched Crépeau and Sorine model returned 71 low-amplitude solitons propagating relatively with more diverse group velocities, specifically between 5.15 and 5.38 ms^{-1}.

3-4-2 Long Artery Results

First h_Y is calculated based on the matched Yomosa model:

$$h_Y = 2.07. \tag{3-28}$$

Using the calculated h_Y, we get 8 and 7 imaginary wavefunctions for the input and the output respectively. The first 3 denormalized wavefunctions and the arterial blood pressure waveform is provided in Figure 3-36.

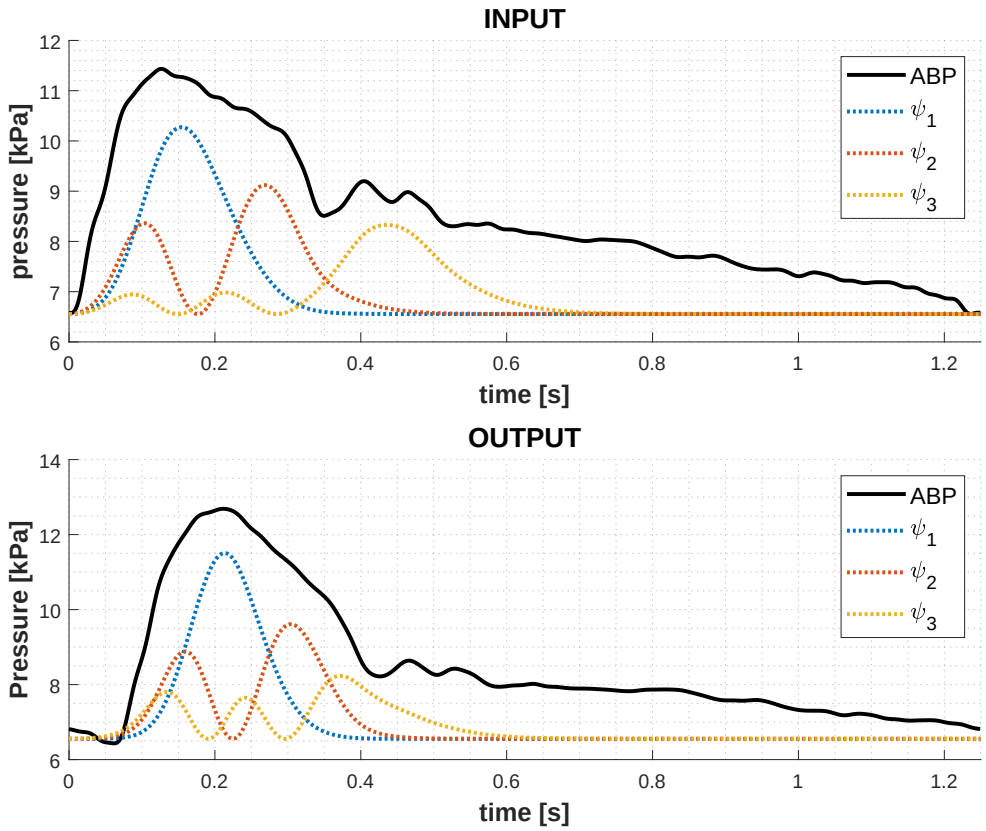

Figure 3-36: Calculated first three denormalized wavefunctions using matched Yomosa model for Case II.

Imaginary $\tilde{\kappa}$ values of the calculated input spectrum are given as

$$\tilde{\kappa} \in \{63.6,\ 52.9,\ 43.8,\ 37.3,\ 32.9,\ 27.4,\ 20.6,\ 6.34\}. \tag{3-29}$$

which correspond to solitons moving with group velocities between 3.31 and 3.34 ms^{-1}. Imaginary $\tilde{\kappa}$ values of the calculated output spectrum are given as

$$\tilde{\kappa} \in \{71.6,\ 58.2,\ 43.8,\ 36.7,\ 32.0,\ 25.5,\ 17.7\}. \tag{3-30}$$

which correspond to solitons moving with group velocities between 3.32 and 3.34 ms^{-1}. Plot of the calculated κ spectrum is provided in Figure 3-37.

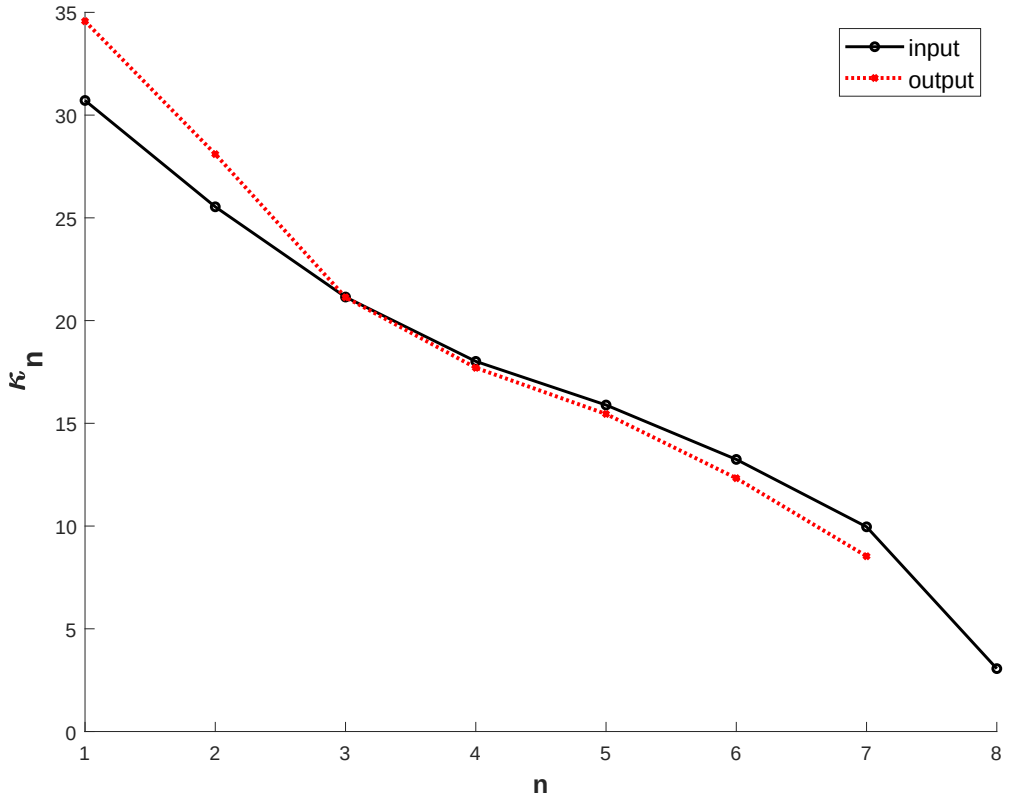

Figure 3-37: Plot of κ_n using matched Yomosa model for Case II.

The first two wavenumbers for the input and the output are found to be higher in the output. The rest of the wavenumbers are found to be in good agreement. As a reminder, based on previous verification tests for the long artery (Figure 3-8), the simulation output had higher values in the systolic portion of the waveform whereas the diastolic portion was found to be in good agreement. The calculated imaginary wavenumbers provide us a similar insight, as the high wavenumbers are associated to the systolic portion of the wavenumber, whereas the lower ones are associated to the diastolic portion. Examining Figure 3-36, in the input

waveform we see the first two wavefunctions are in the systolic portion, whereas the third one is located in the portion associated to the closing of the aortic valve. In the output waveform, the third wavefunction is absorbed into the systolic portion seemingly moving backward. This can be explained steepening which can be addressed by connections to other vessels but not properly by matched KdV model based on previous results for KdV type dynamics verification. Additionally based on test the results of the associated 1-soliton solutions, we expect low amplitude solitons at the inlet to be more preserved at the outlet, which can be seen from the agreement of lower $\tilde{\kappa}$ values.

Next, we calculate V_e by summing the first 3 ψ_n which is provided in Figure 3-38.

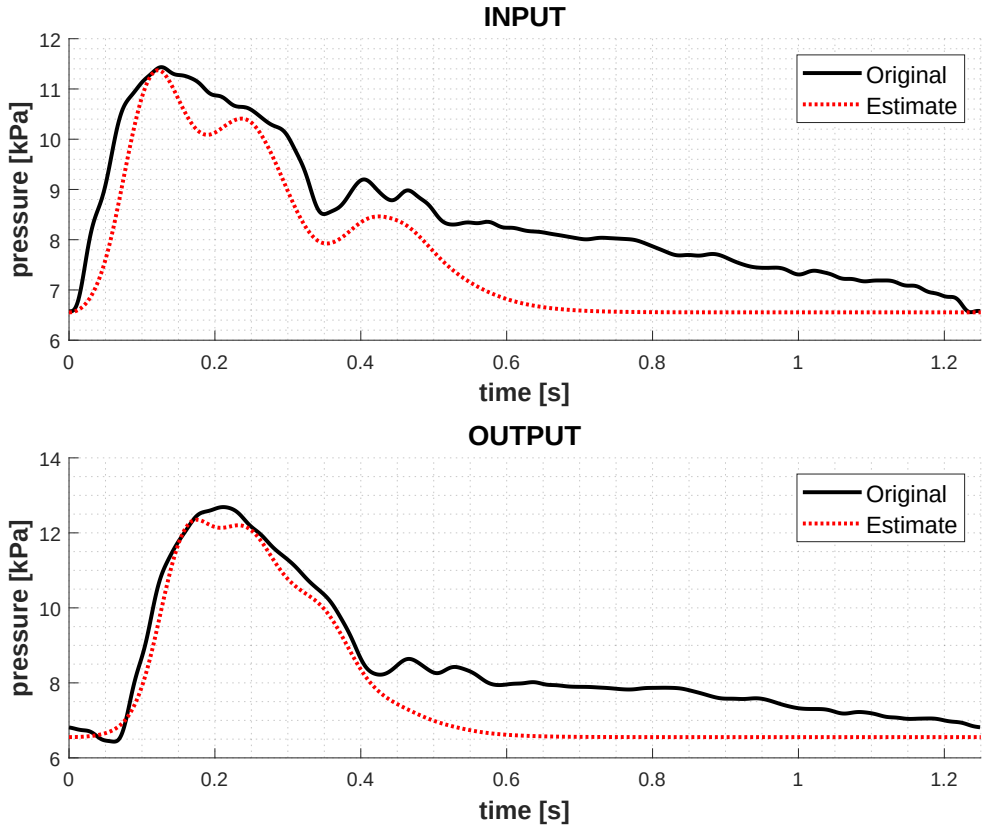

Figure 3-38: The estimate of ABP waveform from the discrete spectrum using matched Yomosa model for Case II using the first 3 denormalized wavefunctions.

The normalized errors associated to the estimates are calculated as

$$\epsilon_{\text{in}} = 0.357, \quad \epsilon_{\text{out}} = 0.412. \tag{3-31}$$

Based on Figure 3-38, the reconstruction of the waveform using the first wavefunctions yield a good representation only in the systolic portion as discussed before, especially at the output. The estimate can be improved by including all the calculated denormalized wavefunctions, which is shown in Figure 3-39.

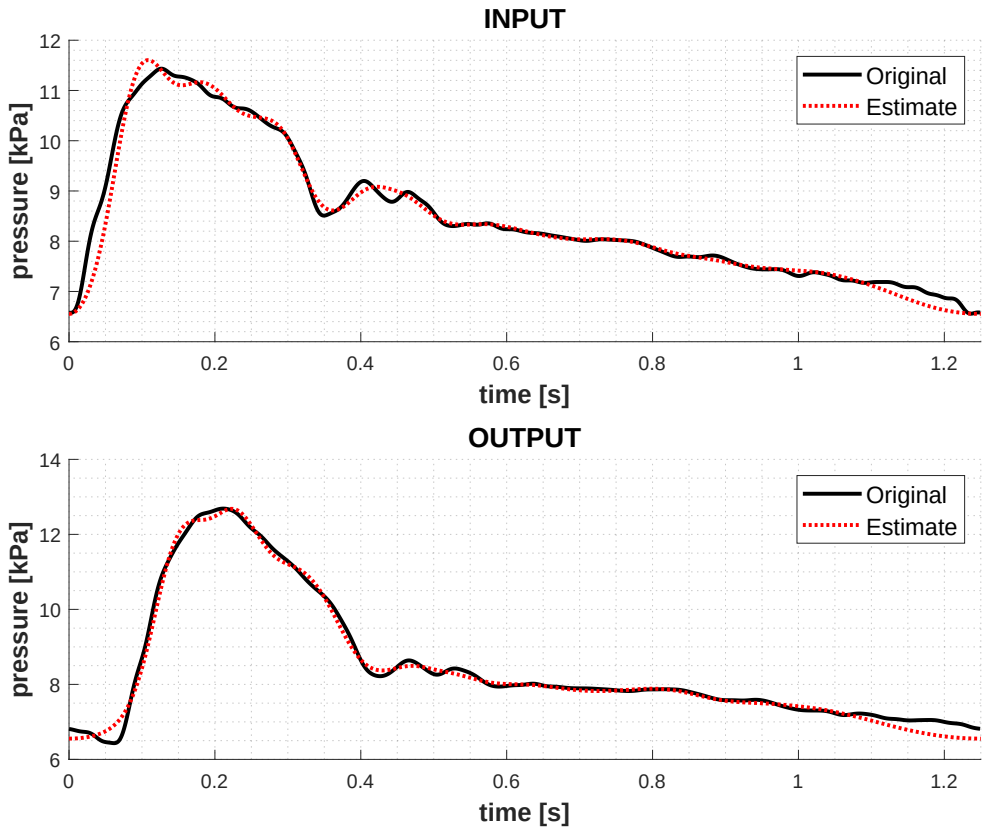

Figure 3-39: The estimate of ABP waveform from the discrete spectrum using matched Yomosa model for Case II using all denormalized wavefunctions.

The normalized errors associated to the new estimates are calculated as

$$\epsilon_{\text{in}} = 0.0632, \quad \epsilon_{\text{out}} = 0.0847. \tag{3-32}$$

The estimate error are low, which can be associated to the reduce value of h_Y. As an important remark, the difference of h_Y value in the short and the long artery case, change the interpretation of the same waveform as the input of the long artery test is assigned as the short artery test, which essentially were found to have different κ spectra with different group velocities between the cases. This is as expected as the analysis method depends on different dynamics. The finding also suggests that a global nonlinear Fourier analysis might be problematic using the matched Yomosa model as the local interpretation of the same waveform differs a lot between different vessels.

Next h_{CS} is calculated based on matched Crépeau and Sorine model:

$$h_{CS} = 0.226. \tag{3-33}$$

Using the calculated h_{CS}, we get 69 and 71 imaginary wavefunctions for the input and the output respectively. It should be pointed out that the calculated h_{CS} has the same value in

the short artery test. This is a promising result for global nonlinear Fourier analysis, as the parameter was found to be invariant between different arteries. Based on the results obtained from the short artery test, discussion based on the first 3 solitons are avoided as the first 3 solitons out of many were not found to be good representatives for the matched Crépeau and Sorine model.

Plot of the calculated κ spectrum is provided in Figure 3-40.

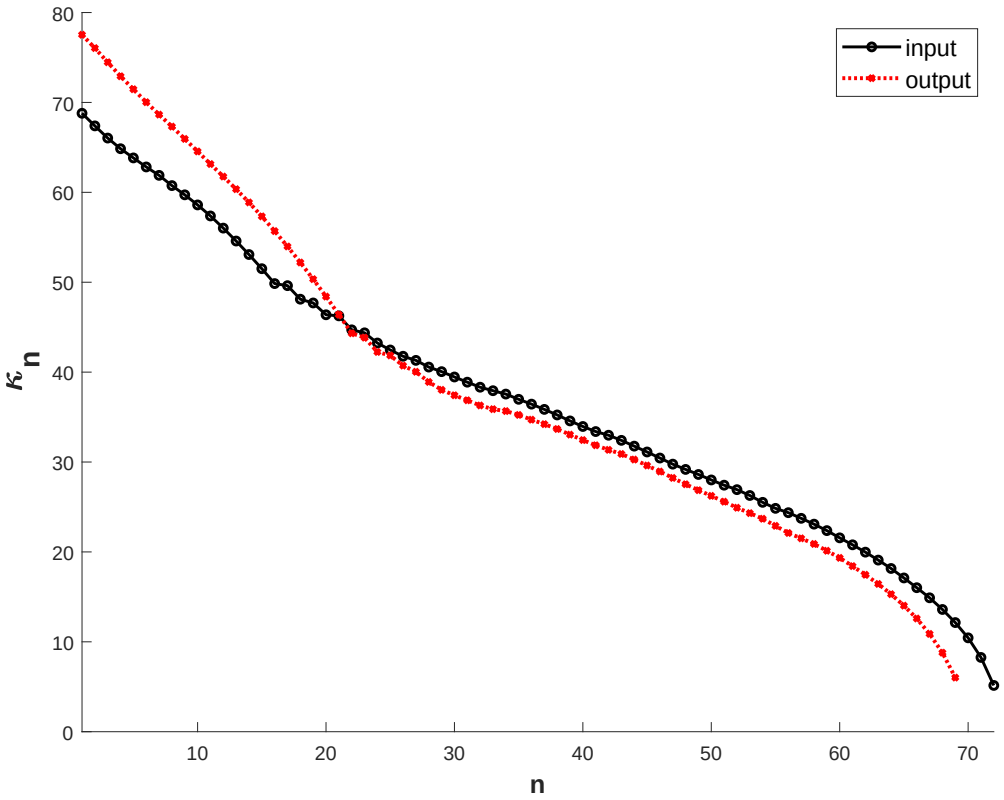

Figure 3-40: Plot of κ_n of matched Crépeau and Sorine model for Case II.

Based on the plot, the imaginary wavenumber spectrum varies significantly in the input and the output spectrum. As the output pressure is calculated based on the simulation model, it is important to consider the results obtained in the long artery KdV type dynamics verification test (Figure 3-8). The simulation output had increased pressure in the systolic part, which was explained in the context of steepening caused by connection to the other vessels and there was a general pressure reduction in the output waveform due to the inclusion of friction. Figure 3-40 provides us a similar insight, as in general κ values of the output are smaller with respect to the input except for the highest κ values which were found to increase at the output. As a reminder, the high κ values are associated to the systolic part of the waveform and the low κ values are associated to the diastolic part so by inspecting Figure 3-40 we can extrapolate the differences in time behavior and vice versa.

The group velocities of the input solitons were found between 5.16 and 5.38 ms^{-1} which

matches the group velocities found for the output in the short artery test. The group velocities of the output solitons were found between 5.16 and 5.45 ms^{-1}.

Next we calculate V_e based on all calculated denormalized wavefunctions which is provided in Figure 3-41.

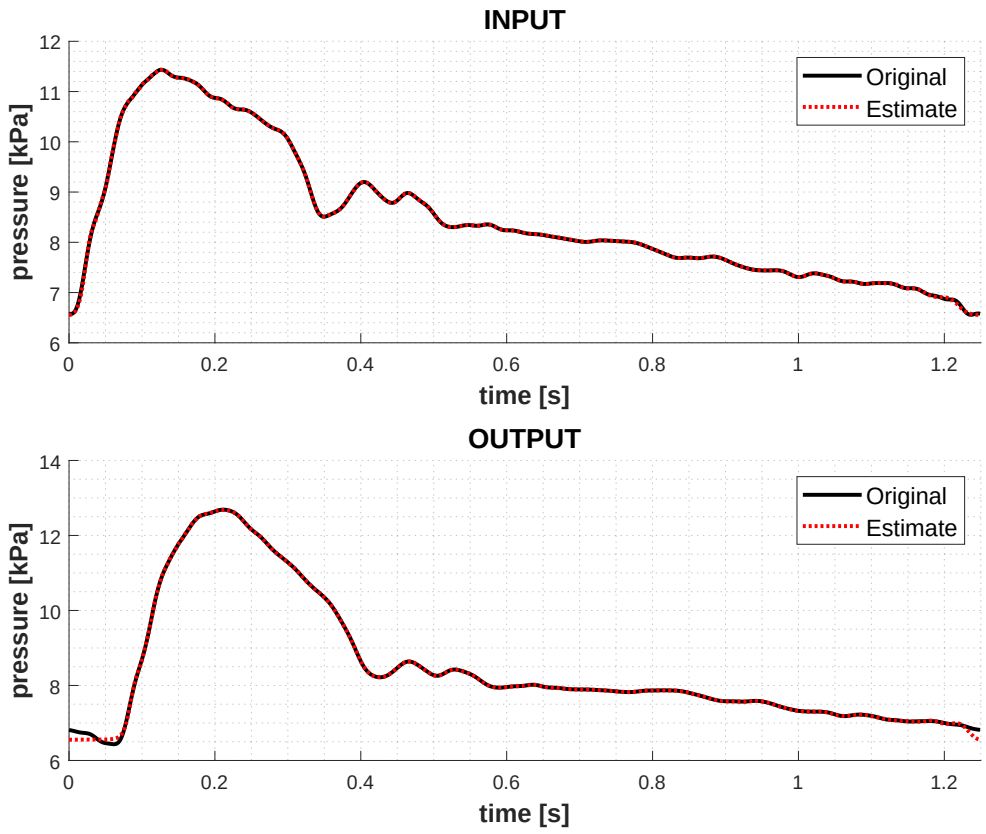

Figure 3-41: The estimate of ABP waveform from the discrete spectrum based on matched Crépeau and Sorine model for Case II using all calculated denormalized wavefunctions.

The normalized errors associated to the estimates are calculated as

$$\epsilon_{\text{in}} = 0.0174, \quad \epsilon_{\text{out}} = 0.00421. \tag{3-34}$$

As many solitons are included in the solution, the reconstruction error is found to be minimal.

Next we only consider the first 16 wavefunctions in the reconstruction to estimate a systolic component which is provided in Figure 3-42.

Like the results obtained in the short artery analysis, the first 16 wavefunctions are found to be dominant in the systolic portion of the waveform. As discussed in the short artery analysis, the systolic estimate can be potentially used to estimate global flow and/or to determine end-systole.

Major differences were found between matched Yomosa and Crépeau and Sorine models in the discrete spectrum analysis in the long artery case. The analysis based on matched Yomosa

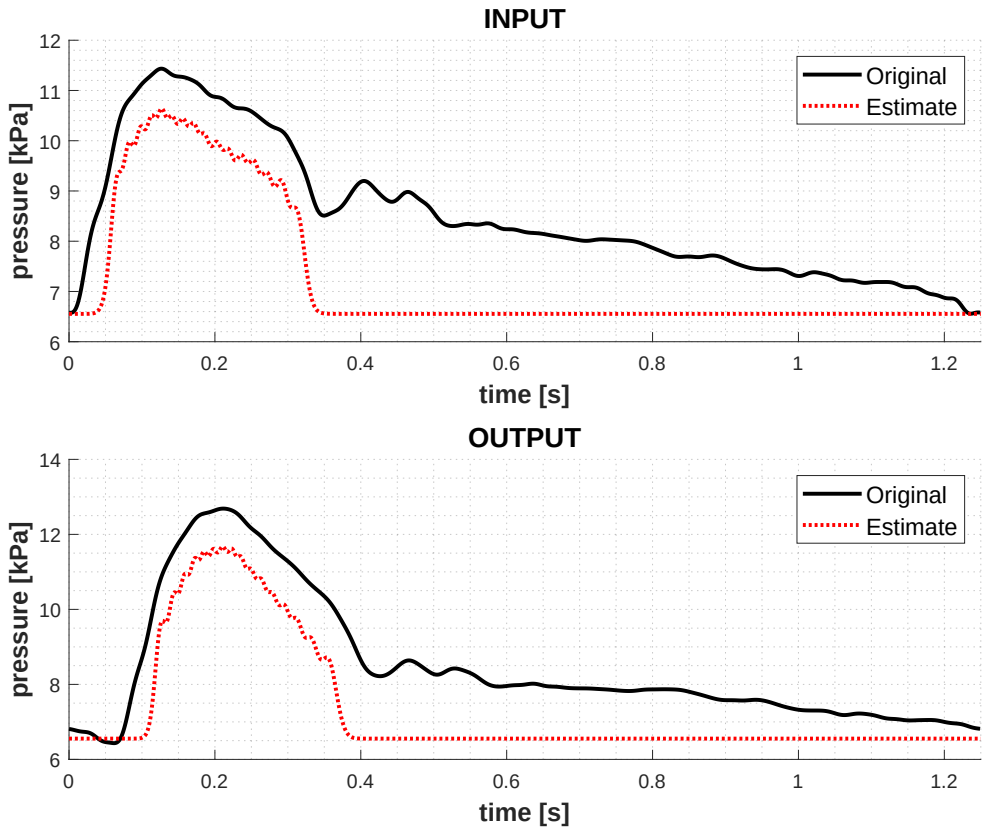

Figure 3-42: The systolic estimate of ABP waveform from the discrete spectrum based on matched Crépeau and Sorine model for Case II using the first 16 denormalized wavefunctions.

model resulted in a different spectrum for the same waveform. In contrast, analysis based on matched Crépeau and Sorine model resulted with identical spectrum for the same waveform. However based on the KdV-type dynamics verification results for the long artery, the matched Crépeau and Sorine model was found inadequate to model the effects of connection to the other vessels which can be also observed in the differing κ spectrum of the input and the output. Although the matched Crépeau and Sorine model was found compatible for global analysis, the mismatch in the simulation and the matched Crépeau and Sorine dynamics from the dynamics verification test suggest that information obtained from the analysis might be representing mathematical phenomena rather than physical phenomena.

3-4-3 Branching Artery Results

First h_Y is calculated based on the matched Yomosa model:

$$h_Y = 2.86. \tag{3-35}$$

Using the calculated h_Y, we get 5 imaginary wavefunctions both for the input and the output. The first 3 denormalized wavefunctions and the arterial blood pressure waveform is provided in Figure 3-43.

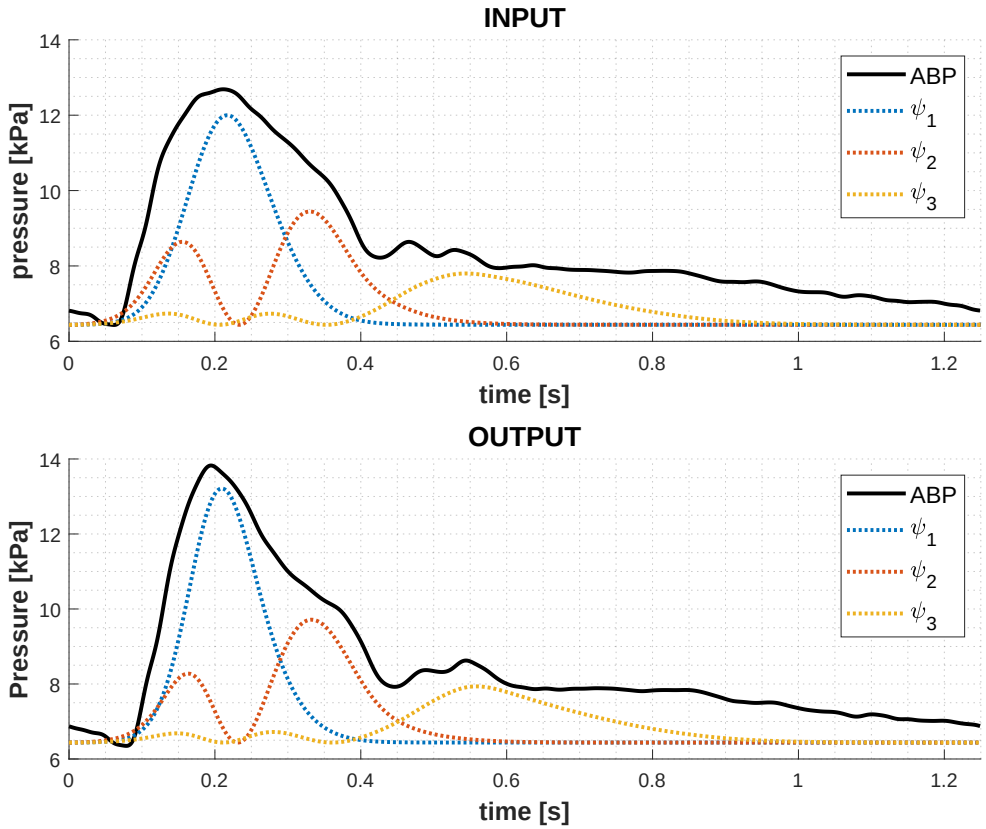

Figure 3-43: Calculated first 3 denormalized wavefunctions using matched Yomosa model for Case III.

Imaginary $\tilde{\kappa}$ values of the calculated input spectrum are given as

$$\tilde{\kappa} \in \{70.0,\ 51.5,\ 37.8,\ 31.5,\ 22.3\}, \tag{3-36}$$

which correspond to solitons moving with group velocities between 5.30 and 5.32 ms^{-1}.

Imaginary $\tilde{\kappa}$ values of the calculated output spectrum are given as

$$\tilde{\kappa} \in \{73.1,\ 51.4,\ 37.7,\ 31.0,\ 21.4\}. \tag{3-37}$$

which correspond to solitons moving with group velocities between 5.30 and 5.33 ms^{-1}.

The wavenumbers for the input and the output are found to be in good agreement except the first one which is increased in the output. As a reminder, based on previous verification tests for the branching artery (Figure 3-11), we expect negligible change in the first reference output waveform except an increase in the systolic portion which can be explained by the increase in the first wavenumber. Next, we calculate V_e by summing the first three ψ_n which is provided in Figure 3-44.

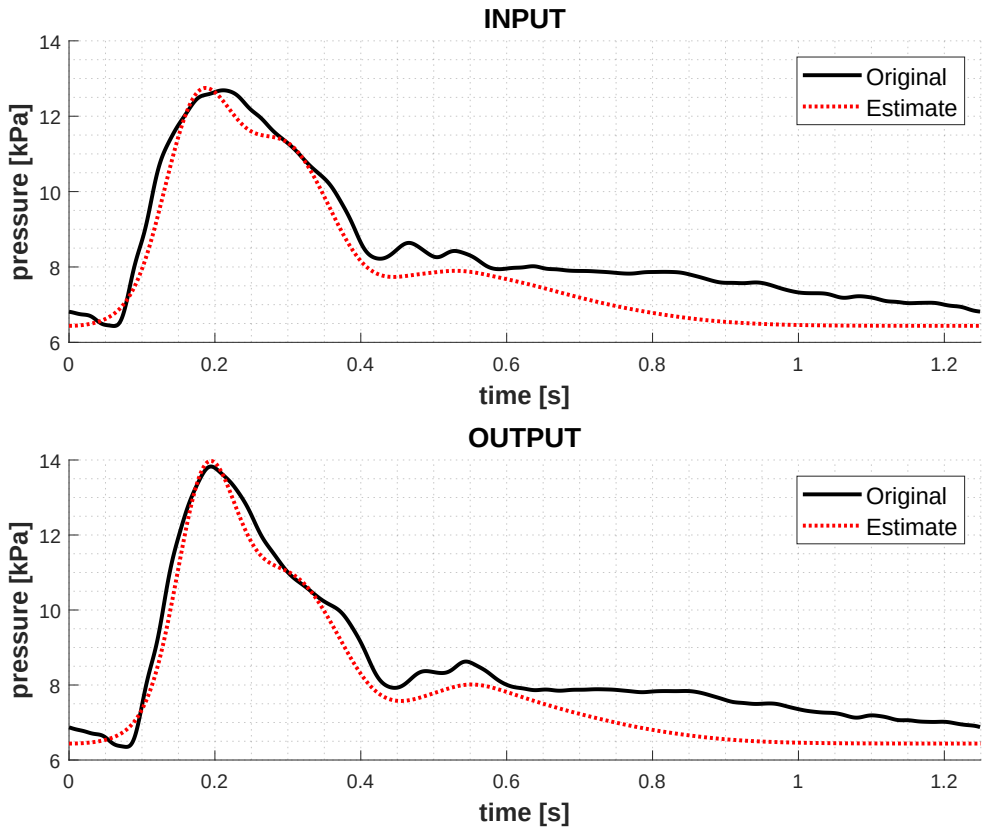

Figure 3-44: The estimate of ABP waveform from the discrete spectrum using matched Yomosa model for Case III using the first 3 denormalized wavefunctions.

The normalized errors associated to the estimates are calculated as

$$\epsilon_{\text{in}} = 0.245, \quad \epsilon_{\text{out}} = 0.260. \tag{3-38}$$

The estimate can be improved by including all the calculated denormalized wavefunctions, which is shown in Figure 3-45.

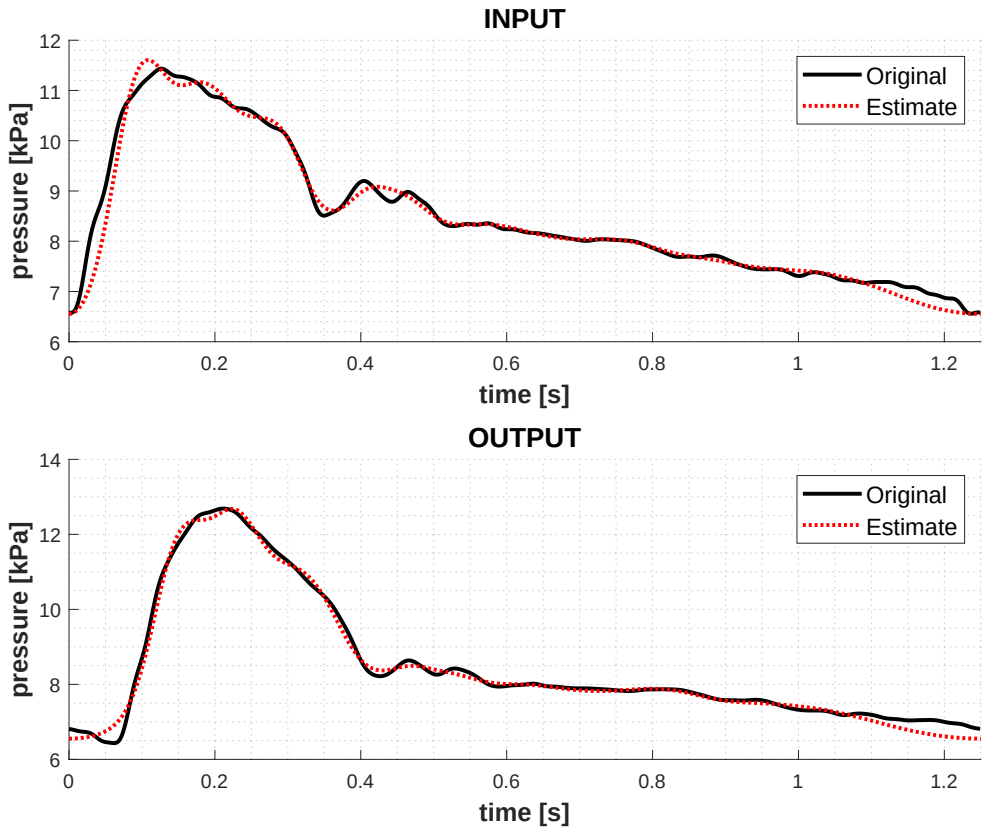

Figure 3-45: The estimate of ABP waveform from the discrete spectrum using matched Yomosa model for Case III using all denormalized wavefunctions.

The normalized errors associated to the new estimates are calculated as

$$\epsilon_{\text{in}} = 0.0913, \quad \epsilon_{\text{out}} = 0.0920. \tag{3-39}$$

As the output of the long artery case is considered to be the input of the branching artery case, we observe difference in spectrum for the same waveform. As discussed in the analysis of the long artery case, this is explained by the difference in h_Y used in analysis.

Next h_{CS} is calculated based on matched Crépeau and Sorine model:

$$h_{CS} = 0.226. \tag{3-40}$$

The value of h_{CS} matches its value in the other case studies.

Using the calculated h_{CS}, we get 73 and 72 imaginary wavefunctions for the input and the output respectively. Based on the results obtained from the short artery test, interpretation based on the first 3 solitons are avoided as the first 3 solitons out of many were not found to be good representatives.

Plot of the calculated κ spectrum is provided in Figure 3-46.

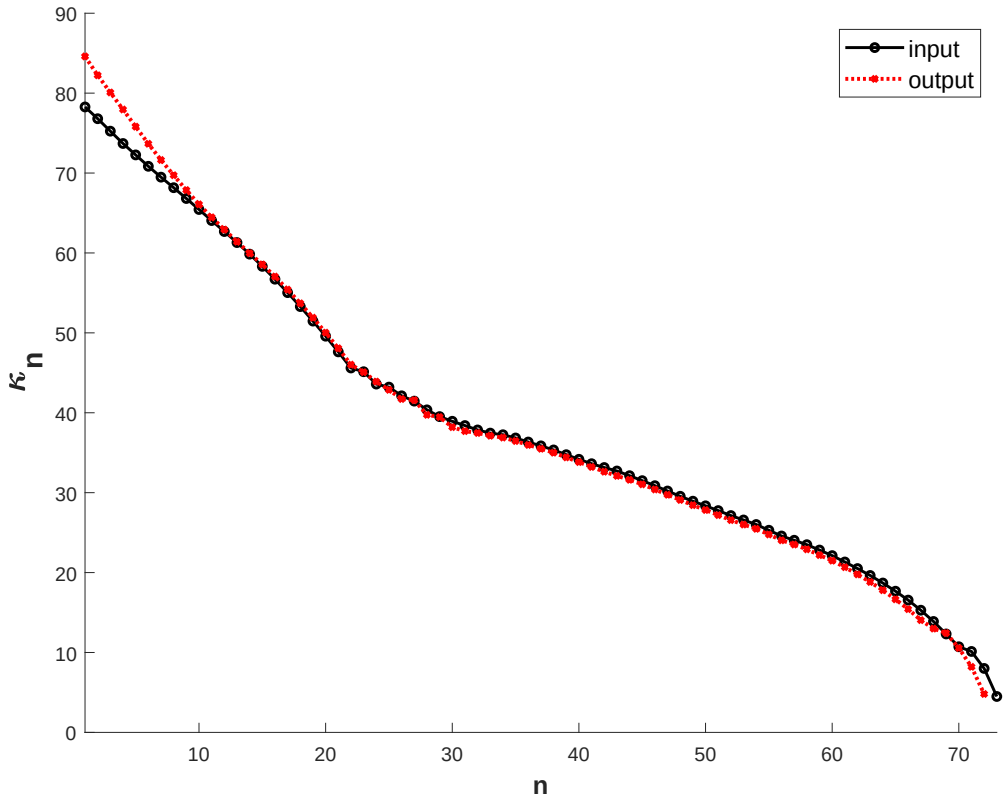

Figure 3-46: Plot of κ_n of matched Crépeau and Sorine model for Case III.

The input and output spectra were found to be in good agreement. We observe increase in the highest κ values at the output which can be explained by the steepening behavior caused by the connection to the other vessels.

The group velocities of the input solitons were found between 5.16 and 5.45 ms^{-1} which matches the group velocities found for the output in the short artery test. The group velocities of the output solitons were found to be between 5.16 and 5.51 ms^{-1}.

Next we calculate V_e based on all calculated denormalized wavefunctions which is provided in Figure 3-47.

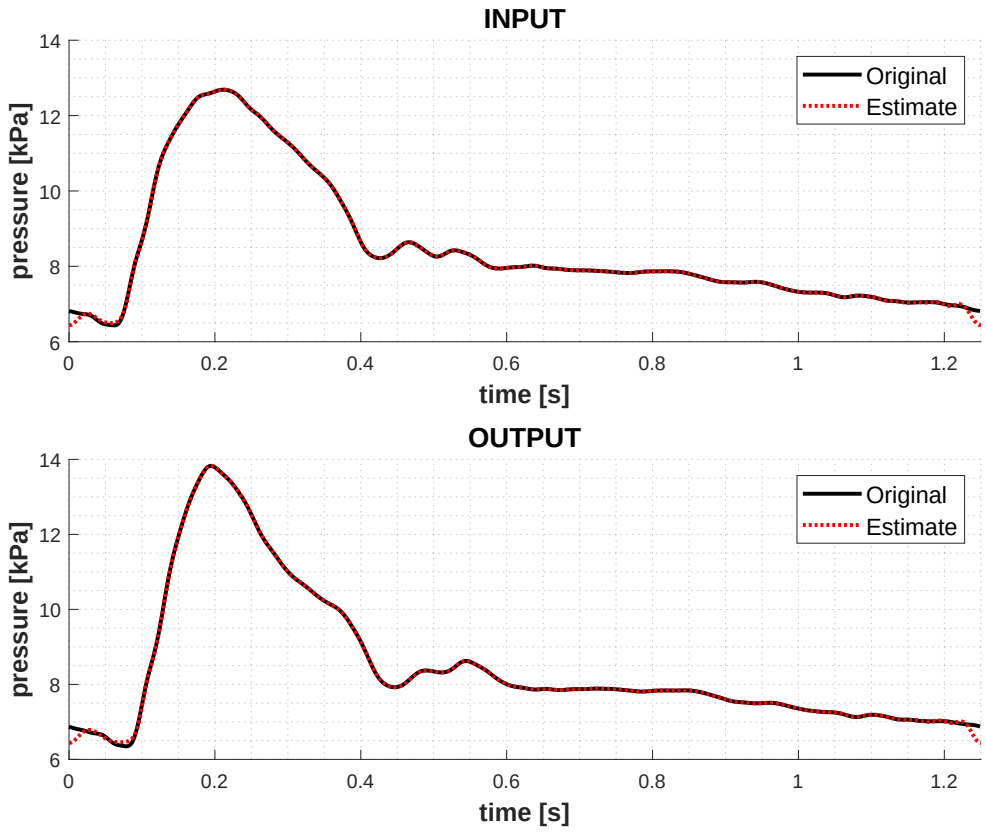

Figure 3-47: The estimate of ABP waveform from the discrete spectrum based on matched Crépeau and Sorine model for Case III using all calculated denormalized wavefunctions.

The normalized errors associated to the estimates are calculated as

$$\epsilon_{\text{in}} = 0.0198, \quad \epsilon_{\text{out}} = 0.0174. \tag{3-41}$$

The reconstruction error is found to be minimal.

Next we only consider the first 16 wavefunctions in the reconstruction to estimate a systolic component which is provided in Figure 3-48.

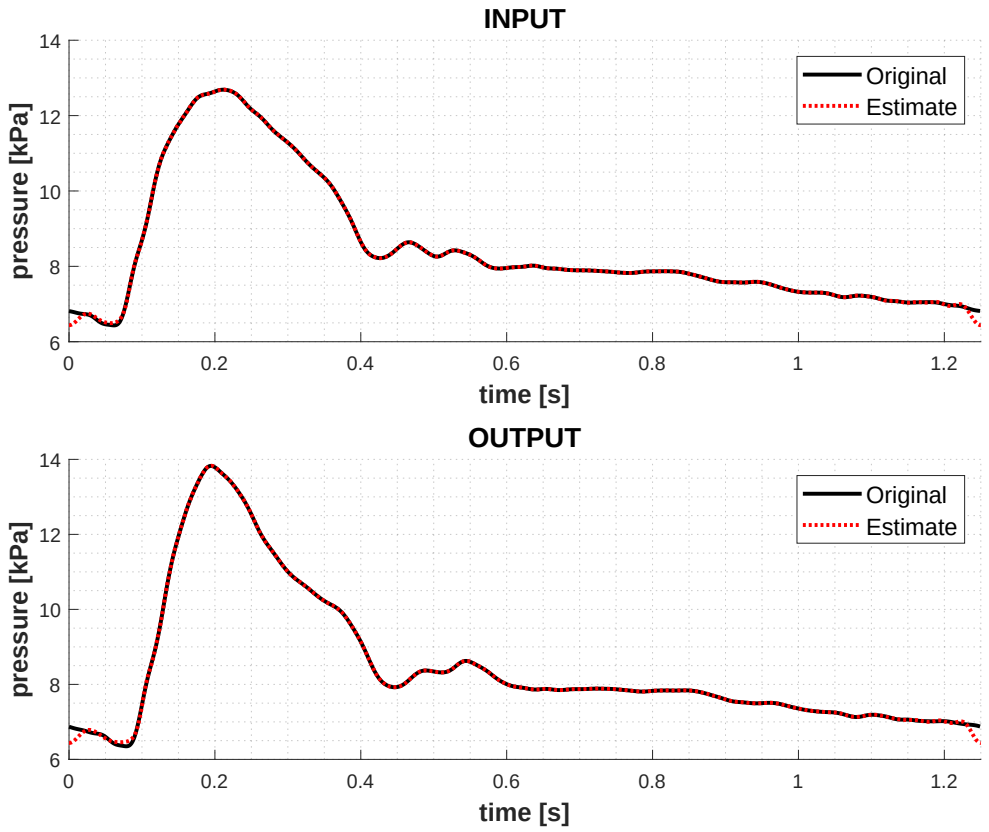

Figure 3-48: The systolic estimate of ABP waveform from the discrete spectrum based on matched Crépeau and Sorine model for Case III using the first 16 denormalized wavefunctions.

Like the results obtained in the analysis of the previous cases, the first 16 wavefunctions are found to be dominant in the systolic portion of the waveform. As discussed in the short artery analysis, the systolic estimate can be potentially used to estimate global flow and/or to determine end-systole.

As the scattering transform parameter was found to be invariant between cases, we also repeat the analysis based on matched Crépeau and Sorine at the outlet of the branches. In particular, the input corresponds to the inlet of the abdominal aorta and the output corresponds to the outlet of one of the iliac arteries in the following tests.

Using the same h_{CS}, we get 73 and 71 imaginary wavefunctions for the input and the output respectively.

Plot of the calculated κ spectrum is provided in Figure 3-49.

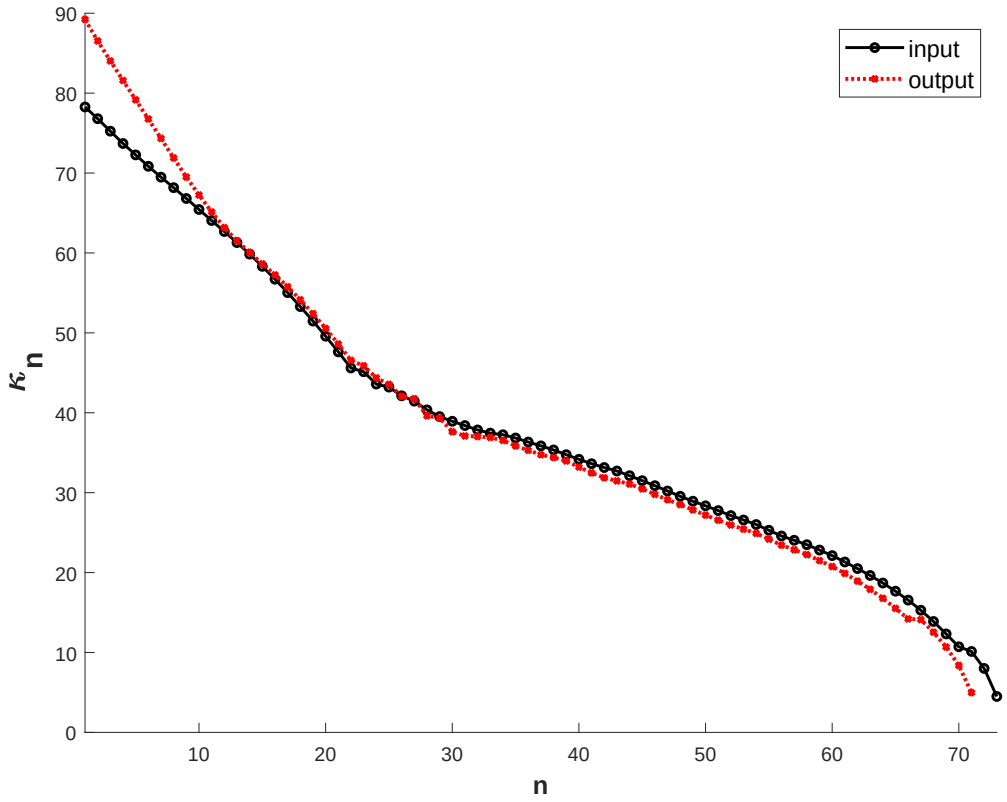

Figure 3-49: Plot of κ_n of matched Crépeau and Sorine model for Case III.

The differences between the input and the output spectrum are found to be greater, compared to the results obtained for the first reference pressure in the same case study. Similarly, we observe increase in the highest κ values at the output which can be explained steepening behavior caused by the connection to the other vessels.

The group velocities of the output solitons were found between 5.16 and 5.55 ms^{-1}.

Next we calculate V_e based on all calculated denormalized wavefunctions which is provided in Figure 3-50.

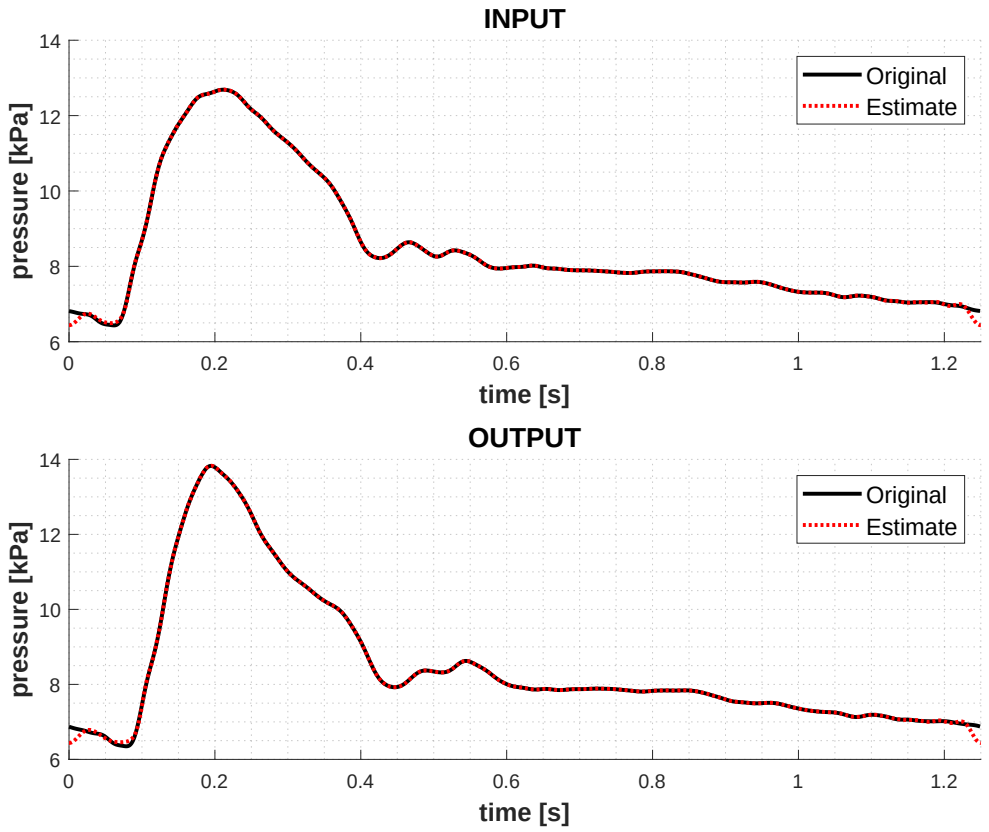

Figure 3-50: The estimate of ABP waveform from the discrete spectrum based on matched Crépeau and Sorine model for Case III using all calculated denormalized wavefunctions.

The normalized errors associated to the estimates are calculated as

$$\epsilon_{\text{in}} = 0.0198, \quad \epsilon_{\text{out}} = 0.0174. \tag{3-42}$$

The reconstruction error is found to be minimal.

Next we only consider the first 16 wavefunctions in the reconstruction to estimate a systolic component which is provided in Figure 3-51.

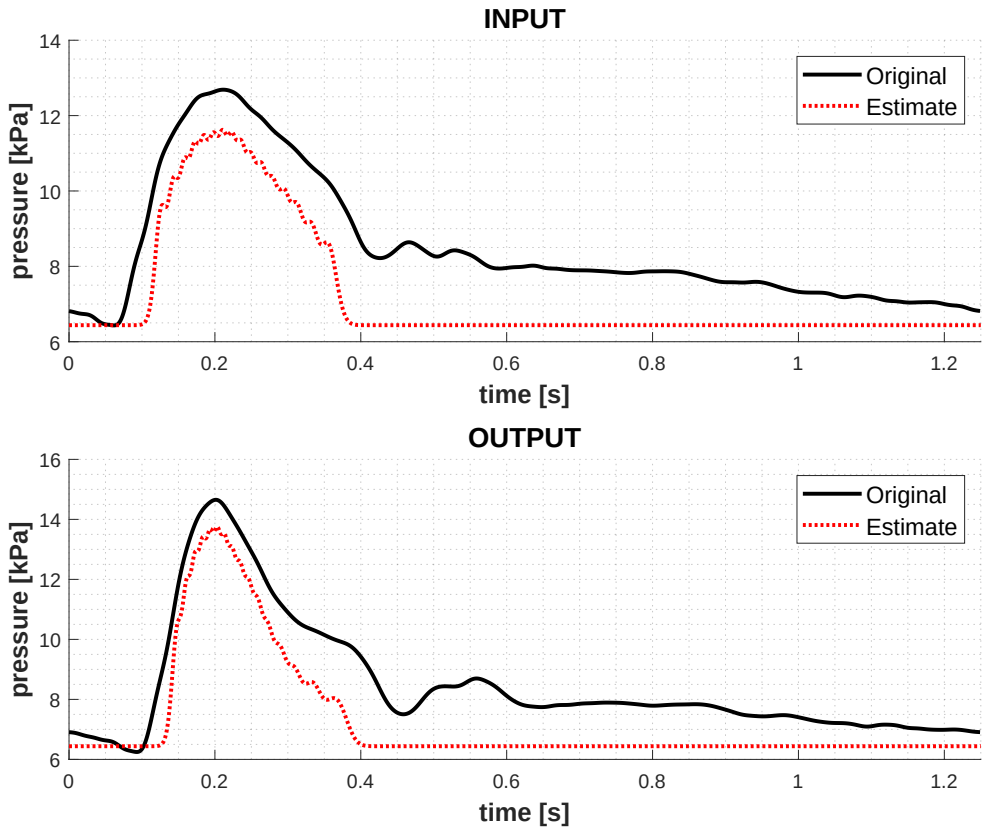

Figure 3-51: The systolic estimate of ABP waveform from the discrete spectrum based on matched Crépeau and Sorine model for Case III using the first 16 denormalized wavefunctions.

The first 16 wavefunctions are found to be dominant in the systolic portion of the waveform.

Compared to the analysis of the longest artery, the analysis of the branching artery provides us similar insight on the applicability of nonlinear Fourier analysis to extract information. As a reminder and a summary:

1. Results obtained from the analysis between the matched models differ significantly.
2. h_{CS} value is consistent between different vessels. On contrary, h_Y varies between different vessels, making even the analysis of the same waveform inconsistent between different cases.
3. Based on the results of the verification of KdV type dynamics, the model mismatches between the tested KdV models and the simulation are reflected in the input and output spectra. Considering model mismatches, the results obtained from the nonlinear Analysis might be representing mathematical phenomena rather than physical phenomena.

Chapter 4

Conclusion

Biomechanical Design Part addresses the clinical importance of modeling arterial blood pressure waveforms in the context of improving non-invasive cardiac output measurements and includes the derivation of dynamics from the basics of fluid motion to the two arterial blood pressure KdV models proposed by Yomosa [6] and Crépeau and Sorine [9]. Using the normalization steps provided in both papers, we derive KdV equation coefficients for the original pressure variable. Yomosa's spacelike KdV equation is converted into timelike form to address space evolution in an artery instead of time evolution, as clinical pressure measurements are done at fixed locations in continuous time. Using the KdV equation in the original pressure variable from Crépeau and Sorine, the corresponding 1-soliton solution for pressure is also derived. The explicit and underlying assumptions of both works are explained in detail. Additional assumptions on the physical parameters are made to make both models consistent with the simulation software, openBF [10], resulting with the matched KdV models and the associated matched 1-soliton solutions.

Systems and Control Part includes the description of the case studies, verification of both matched models' KdV type dynamics and associated 1-soliton solutions, and analysis of arterial blood pressure waveform using scattering transform. The case studies comprise of a short artery, a long artery and a branching artery network which are considered to be the sections of a simplified arterial network from aortic root to the distal end of both iliac arteries.

In the KdV type dynamics verification tests, a realistic pressure waveform is considered as the input for the simplified arterial network and the pressure output is calculated based on the matched KdV equations. The outputs of the matched KdV models are compared to the simulation output to evaluate fits. Both matched KdV model outputs were found to be in good agreement with the simulation output in the short artery case. In the long artery and in the branching artery cases, the systolic parts of both matched KdV model outputs were found to differ from the simulation output. The matched KdV models were found to be inadequate at modeling the steepening phenomena, when the tested vessel or network is assumed to be connected to the other vessels. The effects of including peripheral friction were found to be small but still relevant for the mismatches. Overall the matched Crépeau and Sorine model output was found to a better fit for the simulation output in all case studies.

In the 1-soliton solutions test, the matched 1-soliton solution of Yomosa [6] and the matched 1-soliton solution derived based on Crépeau and Sorine [9], were used as an inlet to the simulation to test soliton propagation. The analytical solution and the simulation output were compared for both models and it was found that the 1-soliton solutions provided at the inlet can not maintain their shape exactly once they arrive at the outlet. However, the soliton behavior was found to be more preserved for low amplitude solitons which was explained in the context of the long wave estimation and the perturbation expansion methods used for the derivation of both KdV models. Overall the analytical results and the simulation outputs were in better agreement for the matched Crépeau and Sorine 1-soliton solution, as the phase differences between the simulation and analytical output were found to be small compared to the matched Yomosa 1-soliton solution.

Finally, the matched timelike KdV equations were used to define the parameter of the associated scattering problems. The scattering problem was used to calculate the discrete spectrum of the input and at the output in all cases, when a realistic inlet is used input to the simplified network. The input and the output spectra for the short artery case were found to be in good agreement. The input and the output spectra for the other cases were found to be different. In particular, highest imaginary wavenumbers in the long and the branching artery cases were found to increase significantly at the output spectra which was explained in the context of steepening. The parameter used in the scattering transform was found to change between different case studies when the parameter is calculated based on the matched Yomosa model. On the contrary, the parameter used in the scattering transform was found to be same when the parameter is calculated based on the matched Crépeau and Sorine model. Scattering transform based on the matched Yomosa model were found to describe a spectrum of slow high amplitude 3 to 7 solitons. Scattering transform based on the matched Crépeau and Sorine model were found to describe a spectrum of relatively fast low amplitude 69 to 73 solitons. Using the spectrum obtained based on matched Crépeau and Sorine model, systolic wave estimates based on grouping the fastest 16 solitons were also included.

Appendix A

Korteweg-De Vries Equation

The KdV Equation is a nonlinear partial differential equation given as

$$\frac{\partial u}{\partial t} + 6u\frac{\partial u}{\partial z} + \frac{\partial^3 u}{\partial z^3} = 0. \tag{A-1}$$

In fact any equation of the form

$$\frac{\partial U}{\partial T} + \alpha U\frac{\partial U}{\partial Z} + \beta\frac{\partial U}{\partial Z} + \gamma\frac{\partial^3 U}{\partial Z^3} = 0, \tag{A-2}$$

where α, β and γ are the scaling constants, is considered to be of KdV type. If the additional term $\beta\frac{\partial U}{\partial Z}$ is associated to a vertical offset in U, the following linear transformations

$$T = \frac{1}{\gamma}t, \quad U = 6\frac{\gamma}{\alpha}u - \frac{\beta}{\alpha}, \quad Z = z, \tag{A-3}$$

can be used to scale Equation A-2 to the standard form. Instead, if the additional term $\beta\frac{\partial U}{\partial Z}$ is associated to a group velocity offset in U, the following transformations

$$T = \frac{1}{\gamma}t, \quad U = 6\frac{\gamma}{\alpha}u, \quad Z = z - \beta t, \tag{A-4}$$

can be used to scale Equation A-2 to the standard form.

The KdV equation has exact solutions when the initial data, $u(z, t_0)$, decays sufficiently rapidly. The initial data decays sufficiently rapidly iff

$$\lim_{|z|\to\infty} \frac{d^n u(z, t_0)}{dz^n} = 0, \quad \forall n \in \mathbb{N}. \tag{A-5}$$

Lax [48] has derived a general principle for associating nonlinear equations evolutions with linear operators. In particular, the KdV Equation can be expressed as a Lax integrable system using linear operator pair, A and L, such that

$$\frac{\partial L}{\partial t} = [A, L] = LA - AL = -\frac{\partial u}{\partial t} = 6u\frac{\partial u}{\partial z} + \frac{\partial^3 u}{\partial z^3}, \tag{A-6}$$

with

$$L = -\frac{\partial}{\partial z} - u \tag{A-7}$$

$$A = 4\frac{\partial^3}{\partial z^3} + 6u\frac{\partial}{\partial z} + 3\frac{\partial u}{\partial z}, \tag{A-8}$$

where $[.,.]$ is the commutator.

Appendix B

Solitons

In a linear non-dispersive medium, any wave propagates without deformation. In a linear dispersive medium, only sinusoidal wave can propagate without deformation. In a nonlinear non-dispersive medium, any wave propagates with deformation. In a nonlinear dispersive medium, if the nonlinear effects compensate the dispersive effects, it results with a special wave called soliton. In particular, solitons are traveling wave solutions of some widespread class of weakly nonlinear dispersive partial differential equations.

Solitons have some characteristic physical properties:

1. Solitons propagate with constant group velocities.
2. Solitons move in one direction.
3. Solitons preserve their shape during their evolution.
4. If a faster soliton takes over a slower one, after their interaction both solitons preserve their form and velocity.
5. The amplitude, the horizontal scaling and the group velocity of the solitons are related in a special way.

The KdV equation admit soliton solutions. In particular, if the initial data evolves according to a KdV type dynamics (Equation A-5), the exact solution can be expressed in terms of finite number of soliton solutions, N-solitons, and a continuous solution associated with the reflections in the transmission. For a KdV equation expressed in the standard form (Equation A-1), the 1-soliton solution is given as

$$u(z,t) = \frac{1}{2}\kappa^2 \mathrm{sech}^2\left(\frac{\kappa}{2}(z-\kappa^2 t)+\delta\right), \tag{B-1}$$

where κ is the imaginary wavenumber and δ is the phase. Equation B-1 describes a normalized soliton traveling to the right with the group velocity κ^2.

Appendix C

Nonlinear Fourier Transform

In 1967, Gardner et al. [45] have developed a method for deriving exact solutions for KdV equation. The method makes use of the spectral problem, for which the solution is interpreted as the potential in 1-D Schroedinger Eigenvalue Problem:

$$-\hbar^2\frac{\partial^2\Psi}{\partial z^2} - u\Psi = \lambda\Psi, \tag{C-1}$$

where $\hbar$ is the spectral parameter, $\Psi = \Psi(z,t) > 0$ are the wavefunctions associated with $\lambda(t)$ eigenvalues. For KdV Equations expressed in the standard form (Equation A-1), $\hbar = 1$. For scaled KdV Equations (Equation A-2), the spectral parameter can be derived using the Lax Pair for the standard KdV equation (A-6) and the linear transformations provided in Equation A-3. In particular, L (Equation A-7) is the Schroedinger operator associated with the spectral problem and L can be derived using the linear transformations of z and u

$$L = -\frac{\partial^2}{\partial Z^2} - \frac{\alpha}{6\gamma}U - \frac{\beta}{6\gamma}. \tag{C-2}$$

The associated spectral problem with Equation A-2 then becomes

$$-\frac{\partial^2\Psi}{\partial Z^2} - \left(\frac{\alpha}{6\gamma}U + \frac{\beta}{6\gamma}\right)\Psi = \lambda\Psi, \tag{C-3}$$

The terms can be rearranged and scaled such that

$$-\hbar^2\frac{\partial^2\Psi}{\partial Z^2} - U\Psi = \left(\frac{6\gamma}{\alpha}\lambda + \frac{\beta}{\alpha}\right)\Psi, \tag{C-4}$$

with

$$\hbar = \sqrt{\frac{\beta}{6\gamma}}. \tag{C-5}$$

Based on Gardner et al. [45], the discrete and the continuous spectrum can be derived. The discrete spectrum consists of N-solitons and the continuous spectrum is associated to the reflections. The derivation of such spectra is referred to as scattering transform, which is analogous to a nonlinear generalization for the Fourier transform.

Considering KdV equation in the standard form (Equation A-1) and the associated scattering problem (Equation C-1), the discrete eigenvalues are negative ($\lambda_n < 0$), finite and constant over time, and the corresponding Ψ_n are given as [45]:

$$\Psi_n \approx d_n(t_0) e^{4\kappa_n^3 t - \kappa_n z}, \quad \text{for } z \to \infty, \tag{C-6}$$

where d_n is the coefficient of the nth discrete wavefunction at $z \to \infty$, $\kappa_n = \sqrt{-\lambda_n} > 0$ is the nth imaginary wave number.

The spectrum for $\lambda > 0$ is continuous. For constant λ, boundary conditions at $z \to \pm\infty$ are imposed to describe the corresponding Ψ [45]:

$$\begin{aligned} \Psi &\approx e^{-ikz} + b(k, t_0) e^{ikz + 8ik^3 t}, \quad \text{for } z \to \infty, \\ \Psi &\approx a(k, t_0) e^{-ikz}, \text{ for } \quad z \to -\infty, \end{aligned} \tag{C-7}$$

where $k = \sqrt{\lambda}$ is the real wavenumber, a is the transmission coefficient and b is the reflection coefficient. These coefficients are scaled such that

$$|a|^2 + |b|^2 = 1.$$

Given b, κ_n and d_n, the inverse scattering transform can be also defined. The reconstruction is also referred to as inverse nonlinear Fourier transform as it is analogous to nonlinear generalization of inverse Fourier transform. Let K for $Z \geq z$ be the solution of the Gel'fand-Levitan equation [45]:

$$K(z, Z) + B(z + Z) + \int_z^\infty K(z, Z) B(z + Z) dZ = 0, \tag{C-8}$$

with

$$B(\tau) = \frac{1}{2\pi} \int_{-\infty}^{\infty} b(k) e^{ik\tau} dk + \sum_n c_n^2 e^{\kappa_n \tau}. \tag{C-9}$$

Then the original signal can be reconstructed using

$$u(z, t) = 2 \frac{dK(z, z)}{dz}. \tag{C-10}$$

Kay and Moses [47] have given the general solution for u where it decomposes exactly into N_h solitons when there is no reflection ($b = 0$) leading to a purely discrete spectrum:

$$u(t) = 4\hbar \sum_{n=1}^{N} \kappa_n \Psi_n^2(t), \tag{C-11}$$

where N is the number of discrete eigenvalues. Depending on the initial data and $\hbar$, N will be finite and fixed.

Appendix D

Long Wave Estimation

Gardner and Morikawa [49] proposed the reductive perturbation method to derive simplified models describing nonlinear wave propagation and interaction. The method is closely related to the soliton theory and it was classically first established for the long wave approximation based on the work of Taniuti and Wei [50]. Long wave approximation is applicable to small amplitude solitons propagating in much longer distance. In principle, first a small positive parameter, ϵ, is introduced such that $\epsilon \ll 1$. Variables in the original equations are expressed as a power series of ϵ. For small ϵ higher order terms are neglected so that the variables are approximated as a polynomial function of ϵ.

As an example, consider a soliton solution to a KdV equation with long L, a small amplitude A and a much larger propagation distance D. For the case $\epsilon \sim \frac{1}{L}$, the scaling of A and D are dependent on ϵ, which is illustrated in Figure D-1.

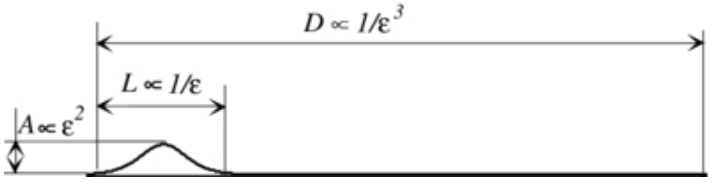

Figure D-1: Length scales of the KdV soliton with small amplitude and much larger propagation distance [51].

These length scales can be proven by considering the terms in the KdV Equation (Equation A-1). Consider the following scaling of the time and space parameters:

$$\frac{\partial u}{\partial t} \sim \frac{1}{D}u, \quad \frac{\partial u}{\partial z} \sim \epsilon u.$$

Then as a consequence, the scale of the dispersive term can be determined:

$$\frac{\partial^3 u}{\partial z^3} \sim \epsilon^3 u. \tag{D-1}$$

For the KdV soliton the nonlinear term and the dispersive term has to compensate for each other, so the scaling of these terms match each other which can be used to determine the scaling of u:

$$u\frac{\partial u}{\partial z} \sim \epsilon u^2 = \epsilon^3 u \rightarrow u \sim \epsilon^2, \tag{D-2}$$

which gives us the fundamental relationship, $A \propto \epsilon^2$. Contribution of the time derivative and the dispersive term can be set to equal each other to derive the scale of D with respect to ϵ:

$$\frac{\partial u}{\partial t} \sim \frac{1}{D}u = \epsilon^3 u \rightarrow D \propto \epsilon^{-3}. \tag{D-3}$$

Bibliography

[1] M. Willemet, P. Chowienczyk, and J. Alastruey, "A database of virtual healthy subjects to assess the accuracy of foot-to-foot pulse wave velocities for estimation of aortic stiffness," *American Journal of Physiology-Heart and Circulatory Physiology*, vol. 309, no. 4, pp. H663–H675, 2015.

[2] F. Otto, "Die grundform des arteriellen pulses," *Zeitung fur Biologie*, vol. 37, pp. 483–586, 1899.

[3] N. Westerhof, P. Sipkema, G. V. D. Bos, and G. Elzinga, "Forward and backward waves in the arterial system," *Cardiovascular research*, vol. 6, no. 6, pp. 648–656, 1972.

[4] Y. Hashizume, "Nonlinear pressure waves in a fluid-filled elastic tube," *Journal of the Physical Society of Japan*, vol. 54, no. 9, pp. 3305–3312, 1985.

[5] Y. Hashizume, "Nonlinear pressure wave propagation in arteries," *Journal of the Physical Society of Japan*, vol. 57, no. 12, pp. 4160–4168, 1988.

[6] S. Yomosa, "Solitary waves in large blood vessels," *Journal of the Physical society of Japan*, vol. 56, no. 2, pp. 506–520, 1987.

[7] E. Crépeau and M. Sorine, "Identifiability of a reduced model of pulsatile flow in an arterial compartment," in *Decision and Control, 2005 and 2005 European Control Conference. CDC-ECC'05. 44th IEEE Conference on*, pp. 891–896, IEEE, 2005.

[8] H. Demiray, "Weakly nonlinear waves in a viscous fluid contained in a viscoelastic tube with variable cross-section," *European Journal of Mechanics-A/Solids*, vol. 24, no. 2, pp. 337–347, 2005.

[9] E. Crépeau and M. Sorine, "A reduced model of pulsatile flow in an arterial compartment," *Chaos, Solitons & Fractals*, vol. 34, no. 2, pp. 594–605, 2007.

[10] A. Melis, *Gaussian process emulators for 1D vascular models*. PhD thesis, University of Sheffield, 2017.

[11] T.-M. Laleg, E. Crépeau, and M. Sorine, "Separation of arterial pressure into a nonlinear superposition of solitary waves and a windkessel flow," *Biomedical signal processing and control*, vol. 2, no. 3, pp. 163–170, 2007.

[12] T.-M. Laleg, E. Crépeau, Y. Papelier, and M. Sorine, "Arterial blood pressure analysis based on scattering transform i," in *Engineering in Medicine and Biology Society, 2007. EMBS 2007. 29th Annual International Conference of the IEEE*, pp. 5326–5329, IEEE, 2007.

[13] T.-M. Laleg, C. Médigue, F. Cottin, and M. Sorine, "Arterial blood pressure analysis based on scattering transform ii," in *Engineering in Medicine and Biology Society, 2007. EMBS 2007. 29th Annual International Conference of the IEEE*, pp. 5330–5333, IEEE, 2007.

[14] T.-M. Laleg-Kirati, C. Médigue, Y. Papelier, F. Cottin, and A. Van de Louw, "Validation of a semi-classical signal analysis method for stroke volume variation assessment: A comparison with the PiCCO technique," *Annals of biomedical engineering*, vol. 38, no. 12, pp. 3618–3629, 2010.

[15] T.-M. Laleg-Kirati, E. Crépeau, and M. Sorine, "Semi-classical signal analysis," *Mathematics of Control, Signals, and Systems*, vol. 25, no. 1, pp. 37–61, 2013.

[16] Y. Mehta and D. Arora, "Newer methods of cardiac output monitoring," *World journal of cardiology*, vol. 6, no. 9, p. 1022, 2014.

[17] J. X. Sun, A. T. Reisner, M. Saeed, T. Heldt, and R. G. Mark, "The cardiac output from blood pressure algorithms trial," *Critical care medicine*, vol. 37, no. 1, p. 72, 2009.

[18] A. J. Lee, J. H. Cohn, and J. S. Ranasinghe, "Cardiac output assessed by invasive and minimally invasive techniques," *Anesthesiology research and practice*, vol. 2011, 2011.

[19] K. B. Domino, T. A. Bowdle, K. L. Posner, P. H. Spitellie, L. A. Lee, and F. W. Cheney, "Injuries and liability related to central vascular catheters: A closed claims analysis," *Anesthesiology: The Journal of the American Society of Anesthesiologists*, vol. 100, no. 6, pp. 1411–1418, 2004.

[20] A. Katsikis, G. Karavolias, and V. Voudris, "Transfemoral percutaneous removal of a knotted swan-ganz catheter," *Catheterization and Cardiovascular Interventions*, vol. 74, no. 5, pp. 802–804, 2009.

[21] M. M. Smith, D. W. Barbara, L. C. Torsher, and C. J. Jankowski, "Nonsurgical removal of knotted pulmonary artery catheter," *Journal of Medical Cases*, vol. 4, no. 3, pp. 163–165, 2012.

[22] S. A. Esper and M. R. Pinsky, "Arterial waveform analysis," *Best Practice & Research Clinical Anaesthesiology*, vol. 28, no. 4, pp. 363–380, 2014.

[23] N. Westerhof, F. Bosman, C. J. De Vries, and A. Noordergraaf, "Analog studies of the human systemic arterial tree," *Journal of biomechanics*, vol. 2, no. 2, pp. 121–143, 1969.

[24] L. Zanoli, S. Rastelli, G. Inserra, and P. Castellino, "Arterial structure and function in inflammatory bowel disease," *World Journal of Gastroenterology: WJG*, vol. 21, no. 40, p. 11304, 2015.

[25] R. Burattini and G. Gnudi, "Computer identification of models for the arterial tree input impedance: comparison between two new simple models and first experimental results," *Medical and Biological Engineering and Computing*, vol. 20, no. 2, pp. 134–144, 1982.

[26] L. Formaggia, D. Lamponi, and A. Quarteroni, "One-dimensional models for blood flow in arteries," *Journal of engineering mathematics*, vol. 47, no. 3-4, pp. 251–276, 2003.

[27] H. Demiray, "Nonlinear waves in a viscous fluid contained in a viscoelastic tube," *Zeitschrift für angewandte Mathematik und Physik ZAMP*, vol. 52, no. 6, pp. 899–912, 2001.

[28] J. Misra and M. Patra, "A study of solitary waves in a tapered aorta by using the theory of solitons," *Computers & Mathematics with Applications*, vol. 54, no. 2, pp. 242–254, 2007.

[29] J.-F. Paquerot and M. Remoissenet, "Dynamics of nonlinear blood pressure waves in large arteries," *Physics Letters A*, vol. 194, no. 1-2, pp. 77–82, 1994.

[30] N. Westerhof, *Physics of Heart and Circulation.* CRC Press, 1993.

[31] C. G. Caro, T. Pedley, and R. Schroter, *The mechanics of the circulation.* Cambridge University Press, 2012.

[32] C. G. Caro and R. M. Nerem, "Transport of 14c-4-cholesterol between serum and wall in the perfused dog common carotid artery," *Circulation Research*, vol. 32, no. 2, pp. 187–205, 1973.

[33] N. Smith, A. Pullan, and P. J. Hunter, "An anatomically based model of transient coronary blood flow in the heart," *SIAM Journal on Applied mathematics*, vol. 62, no. 3, pp. 990–1018, 2002.

[34] P. Hunter, *Numerical simulation of arterial blood flow.* PhD thesis, ResearchSpace@ Auckland, 1972.

[35] G. Hagen, "Ueber die bewegung des wassers in engen cylindrischen röhren," *Annalen der Physik*, vol. 122, no. 3, pp. 423–442, 1839.

[36] J. L. Poiseuille, *Recherches expérimentales sur le mouvement des liquides dans les tubes de très-petits diamètres.* Imprimerie Royale, 1844.

[37] N. Xiao, J. Alastruey, and C. Alberto Figueroa, "A systematic comparison between 1-D and 3-D hemodynamics in compliant arterial models," *International journal for numerical methods in biomedical engineering*, vol. 30, no. 2, pp. 204–231, 2014.

[38] A. Osborne and M. Petti, "Numerical inverse-scattering-transform analysis of laboratory-generated surface wave trains," *Physical Review E*, vol. 47, no. 2, p. 1035, 1993.

[39] E. Boileau, P. Nithiarasu, P. J. Blanco, L. O. Müller, F. E. Fossan, L. R. Hellevik, W. P. Donders, W. Huberts, M. Willemet, and J. Alastruey, "A benchmark study of numerical schemes for one-dimensional arterial blood flow modelling," *International journal for numerical methods in biomedical engineering*, vol. 31, no. 10, p. e02732, 2015.

[40] X. Wang, J.-M. Fullana, and P.-Y. Lagrée, "Verification and comparison of four numerical schemes for a 1d viscoelastic blood flow model," *Computer methods in biomechanics and biomedical engineering*, vol. 18, no. 15, pp. 1704–1725, 2015.

[41] S. Sherwin, V. Franke, J. Peiró, and K. Parker, "One-dimensional modelling of a vascular network in space-time variables," *Journal of Engineering Mathematics*, vol. 47, no. 3-4, pp. 217–250, 2003.

[42] H. C. Chen, V. Patel, J. Wiek, S. M. Rassam, and E. M. Kohner, "Vessel diameter changes during the cardiac cycle," *Eye*, vol. 8, no. 1, p. 97, 1994.

[43] A. G. Brown, Y. Shi, A. Marzo, C. Staicu, I. Valverde, P. Beerbaum, P. V. Lawford, and D. R. Hose, "Accuracy vs. computational time: translating aortic simulations to the clinic," *Journal of biomechanics*, vol. 45, no. 3, pp. 516–523, 2012.

[44] T. A. Driscoll, N. Hale, and L. N. Trefethen, "Chebfun guide," 2014.

[45] C. S. Gardner, J. M. Greene, M. D. Kruskal, and R. M. Miura, "Method for solving the Korteweg-de Vries equation," *Physical review letters*, vol. 19, no. 19, p. 1095, 1967.

[46] A. Osborne, "Nonlinear Fourier analysis for the infinite-interval Korteweg-de Vries equation i: An algorithm for the direct scattering transform," *Journal of Computational Physics*, vol. 94, no. 2, pp. 284–313, 1991.

[47] I. Kay and H. Moses, "Reflectionless transmission through dielectrics and scattering potentials," *Journal of Applied Physics*, vol. 27, no. 12, pp. 1503–1508, 1956.

[48] P. D. Lax, "Integrals of nonlinear equations of evolution and solitary waves," *Communications on pure and applied mathematics*, vol. 21, no. 5, pp. 467–490, 1968.

[49] C. Gardner and O. Morikawa, "Similarity in the asymptotic behaviour of collision-free hydromagnetic waves and water waves," *Sc. Rep. NYO*, vol. 9082, 1960.

[50] T. Taniuti and C.-C. Wei, "Reductive perturbation method in nonlinear wave propagation. i," *Journal of the Physical Society of Japan*, vol. 24, no. 4, pp. 941–946, 1968.

[51] H. Leblond, "The reductive perturbation method and some of its applications," *Journal of Physics B: Atomic, Molecular and Optical Physics*, vol. 41, no. 4, p. 043001, 2008.